DEFECT CHARACTERIZATION AND PHASE ANALYSES OF COPPER ZINC TIN SULFIDE/SELENIDE

by

Elizabeth Lund

A dissertation submitted to the faculty of
The University of Utah
in partial fulfillment of the requirements for the degree of

Doctor of Philosophy

Department of Chemical Engineering

The University of Utah

December 2014

The University of Utah Graduate School

STATEMENT OF DISSERTATION APPROVAL

The dissertation of **Elizabeth Lund**

has been approved by the following supervisory committee members:

Michael Scarpulla	, Co-Chair	**10/18/14** Date Approved
Eric Eddings	, Co-Chair	**10/28/14** Date Approved
Jules Magda	, Member	**10/28/14** Date Approved
Geoffrey Silcox	, Member	**10/28/14** Date Approved
Loren Rieth	, Member	**10/28/14** Date Approved

and by **Milind Deo** , Chair/Dean of

the Department/College/School of **Chemical Engineering**

and by David B. Kieda, Dean of The Graduate School.

ABSTRACT

This work characterizes defects and phases within $Cu_2ZnSn(S,Se)_4$ (CZTS(Se)), an earth-abundant material used to make thin film photovoltaic solar cells. Overall research efforts focus on improving the solar cell device efficiency with the hope that it can be produced at the terawatt energy scale and circumvent material supply bottlenecks of current thin film photovoltaic technology. In this work, deep defects, composition-dependent crystalline disorder and secondary phase formation, and polymorph variation are all explored to determine the effects on the CZTS(Se) absorber layer within a solar cell device. Chapter 1 introduces how thin film photovoltaics fit into the global energy perspective and gives background into the ideal CZTSSe material characteristics, solar cell function, and current knowledge about why CZTS(Se) device performance still lags other current thin film photovoltaics. Chapter 2 explains the temperature admittance and deep level transient capacitance spectroscopy methods used in Chapter 3. Chapter 3 reports the observation of a deep defect state 590 meV from the conduction band edge with an attractive capture cross section of 2 x 10-14 cm^{-2} behaving as an electron trap within nanoparticle-ink deposited CZTSSe. This is the first report of minority carrier trapping within CZTS(Se). Chapter 4 reports the coherent (Cu_2SnS_3, CZTS) and incoherent (Cu_xS, Sn_xS_y) phases formed in a compositionally-varied coevaporated CZTS film. Raman spectroscopy experiments show Cu/Sn composition-dependent differences within the Cu_2SnS_3 crystalline structure of films deposited at low temperatures and CZTS crystalline disorder in films deposited at higher temperatures. This work demonstrates the deleterious effect of Sn-rich growth on the

overall crystalline quality and possible defect concentration within CZTS. Chapter 5 reports the results of modeling the effects of varying the polymorph of the absorber layer within a CZTS solar cell. The kesterite and stannite polymorph variation do not significantly negatively impact the absorber layer in the bulk, however, the presence of kesterite at the interface and stannite in the bulk is shown to have the highest solar cell efficiencies. Chapter 6 summarizes each project and outlines future work.

This work is dedicated to Chad Kramer, Jed Lund, and Alexandra Kelly.
I am grateful for the personal support and unique roles of encouragement that each gave
to help me accomplish this work.

TABLE OF CONTENTS

LIST OF FIGURES

ACKNOWLEDGEMENTS

I am extraordinarily grateful to my mentor, Prof. Mike Scarpulla. His patience and continued dedication to developing my ability as a researcher enabled me to accomplish this work. His passion for photovoltaic research, very hard work to secure funds, and continued generation of novel ideas made this research possible. He also engendered exploration of a wide variety of topics within my research that strengthened my overall skill set and is unique to most doctorate experiences.

I am also thankful to my committee members for their support and feedback in my research as well as great classroom instruction with thorough and clear teaching. I am especially grateful to Prof. Eric Eddings for his initial and continued support despite my shift in research interests. He lives by the quote taped to his computer monitor, "People don't always remember…what you do, but they always remember how you made them feel." – Maya Angelou

I am also grateful for the many discussions with undergraduate students, fellow graduate students, and postdocs. I also appreciate the combinatorial CZTS samples and insightful discussions with collaborators, Dr. Glenn Teeter and Dr. Hui Du at the National Renewable Energy Laboratory. I am also grateful to Caleb Miskin and Prof. Rakesh Agrawal at Purdue for the CZTSSe sample.

The research at the University of Utah was fully supported by the U.S. Department of Energy, Office of Basic Energy Sciences, Division of Materials Sciences and Engineering under Award DE-SC0001630.

CHAPTER 1

INTRODUCTION

Photovoltaics on the Global Energy Scale

Global energy consumption is projected to increase from 18 terawatts (TW) in 2010 to 28 TW in 2040 [1]. Although the cumulative global renewable electricity installed capacity has grown by 97% from 2000 to 2012 to now account for 27% of worldwide electricity generation [2], further growth is required to meet increasing energy demands. Increasing energy generation from renewable resources will reduce reliance on finite fossil fuels and mitigate the detrimental effects of CO_2 release, but these renewable technologies must be able to produce on the TW scale in order to make an appreciable difference. With $>10^5$ TW incident sunlight on the earth, solar power is promising for large-scale energy production. Sunlight may be harvested through conversion to thermal, chemical, or electrical energy. Currently photovoltaic (PV) power systems, which transfer energy from photons to electrons via the photoelectric effect, comprise the large majority of solar power installations. Even though solar power is currently a small 1.8% contribution to worldwide electricity generation, solar is the fastest growing sector in renewable electricity generation with a 49-fold increase from 2000 to 2012 [2], and shows promise for electricity generation on the TW scale.

Thin Film Photovoltaics

Either single or polycrystalline silicon (c-Si) is the semiconductor used as the photoactive layer in 90% of all new PV installations. The other 10% comprises thin film technologies using CdTe, $CuIn_xGa_{1-x}Se_2$ (CIGSe), and amorphous or nanocrystalline Si [3]. As the name implies, thin films only use 1-3 μm of semiconductor for sunlight absorption, whereas a thicker c-Si wafer will be >100 μm. Despite the high energy cost to produce ≥99.9999% pure Si wafers [4], global solar electricity generation is still dominated by this well-developed technology because growth is sustained through continued improvements in device design, material quality, and material processing [5]. Even though these advances result in higher overall module efficiencies for c-Si (η=22.9% for record efficiency of c-Si module vs. η=17.5% for record efficiency of CdTe module [6]), thin film deposition is not only less energetically expensive, but also more versatile. Thin films can be deposited by a variety of methods including coevaporation, sputtering, solution deposition, or nanoparticle "ink" to form polycrystalline films with grain sizes on the order of a μm. They can be deposited onto the traditional glass substrate or flexible metal or plastic films which enable roll-to-roll processing. Thin films can also be deposited over large areas so an entire module (~1 m^2) may be "printed" at once, whereas c-Si-based solar cells (~100-400 cm^2) are limited by wafer size, and additional soldering is required to connect multiple cells to form a module.

Thin film PV manufacturing and installation advantages as well as recent advances in record cell efficiencies of CdTe (η=21.0% [7]) and CIGSe (η=20.8% [8]) technologies encourage continued research to overcome the disadvantages of lower module efficiencies and inclusion of toxic, rare-earth elements including Cd, Te, In, and Se. Since the CIGSe

and CdTe absorber layers are sequestered between large pieces of glass or plastic, leaching is of no concern if the module remains intact, and no appreciable amounts of these toxic elements are emitted during PV operation [9]. Even though the toxicity concerns can be alleviated by safe manufacturing processes and proper end-of-life module disposal, the limited raw material supply is an unresolved concern when considering scale-up of CIGSe and CdTe to TW levels of production.

Earth-Abundant CZTS

Using the 2012 production volumes of mineable ores as a metric for scalability [4], it would require 700 years to make 1 TW of CdTe PV modules because of limited Te, and it would require 200 years to make 1 TW of CIGSe modules because of limited In. These time frames are huge compared to 1 TW of c-Si PV, which could be made in 3 years. (These estimates account for typical thicknesses and densities for each of these materials, efficiency η=10%, and typical solar irradiation, but do not account for the additional purification of metallurgical grade silicon to higher purity.)

The alternative earth-abundant material Cu_2ZnSnS_4 (CZTS) has a very similar crystalline structure to CIGSe and may provide the same thin film benefits of this "close cousin" while also circumventing toxicity and supply bottleneck issues. One TW of CZTS modules could be made in just under 1 year! (This is based on similar calculations [4], but using η=5%.) The limiting element in the CZTS case is Sn. The caveat is the η=8.4% [10] CZTS solar cell record device efficiency is significantly lower than η=20.8% [8] for CIGSe, and the CZTS device efficiency is difficult to improve without addition of Se [11] to the absorber layer. One TW of $Cu_2ZnSnSe_4$ (CZTSSe) modules would require 90 years to make at the current limited rate of Se supply (assuming a higher η=10%). Therefore,

understanding and overcoming the hurdles to reach higher $Cu_2ZnSn(S,Se)_4$ (CZTS(Se)) solar cell device efficiencies is paramount to establishing commercial viability to this appealing earth-abundant thin film photovoltaic material.

A Note on Acronyms

This research explores three types of materials that vary only by chalcogen composition: sulfur-only Cu_2ZnSnS_4 (CZTS), selenium-only $Cu_2ZnSnSe_4$ (CZTSe), or the mixed sulfo-selenide $Cu_2ZnSn(S_x,Se_{1-x})_4$ (CZTSSe). When referring to all three of these as a general class, the acronym CZTS(Se) is used.

Photovoltaic Solar Cell Operation

There are three factors necessary for a photovoltaic solar cell to generate electrical work from absorbed light energy. First, the device must absorb light with enough energy so that electrons originally in a ground state bound to atoms in the crystal lattice of the semiconductor are promoted to an excited, unbound state in which they become "free carriers." This promotion of electrons from the highest occupied molecular orbital (HOMO), also called the valence band maximum (VBM) of the semiconductor, to the lowest unoccupied molecular orbital (LUMO), or conduction band minimum (CBM) results in free carriers, which are electrons in the conduction band and holes in the valence band. Second, these light-generated electron-hole pairs must be spatially separated to avoid annihilation by recombining. Once they are separated, they must lastly travel to the front and back contacts where they are collected by the external circuit to accomplish electrical work.

Figure 1.1 shows the layers in a typical CZTS(Se) solar cell. The CZTS(Se) is the

active absorber layer where the electron-hole pairs are generated, separated, and then drift to the external circuit. To separate the electron-hole pairs generated within the CZTS(Se) absorber layer, the solar cell device contains a p-n junction at the CdS/CZTS(Se) interface (Figure 1.1). The junction formed from intrinsic p-type CZTS(Se) and n-type CdS contains both an asymmetric spatial variation in voltage potential as well as an asymmetric energetic variation in conduction and valence band offsets, as shown in Figure 1.2. The potential varies within the space charge region (SCR) and drives electrons towards the CdS where they will be collected by the front contact. The holes are driven to the back interface to be collected by the back contact.

CZTS(Se) Material Properties

CZTS belongs to the class of Group I_2-II-IV-VI_4 quaternary semiconductors. With a mixed sulfide/selenide composition, it is considered pentenary. CZTS(Se) forms several different polymorphs, which are all based on a tetragonal lattice structure. The most energetically favorable crystalline structure is kesterite, with the stannite polymorph differing only in cation arrangement and being only 0.2 eV higher in formation energy [12] (Figure 1.3).

The absorption coefficient ($>10^{-4}$ cm^{-1}) [13] indicates the capability for CZTS(Se) to effectively absorb light, and the bandgap enables charge carrier generation, which satisfies the first of the three requirements for effective solar energy generation. The CZTS(Se) band gap, which is the energy barrier from a bound to an unbound electron, can be tuned from 1.0 eV (CZTSe) to 1.5 eV (CZTS) [14]. This energy range spans the solar spectrum and is therefore ideal for sunlight absorption [15]. CZTSSe also has a direct bandgap, which is desirable for optoelectronic materials since there is a higher probability

an absorbed photon will generate an electron/hole pair because the band to band transition conserves crystalline momentum [16]. An indirect semiconductor such as Si requires an additional interaction with the crystal to gain the necessary momentum for the band to band transition.

The bandgap of CZTS(Se) indicates a homojunction CZTSSe device with a spatially-uniform bandgap could theoretically achieve $\eta \sim 30\%$, the maximum efficiency possible for a single junction solar cell [15]. However, this theoretical prediction, the Shockley-Queisser limit, only accounts for losses from radiative recombination of electron/hole pairs within the absorber layer and neglects losses from crystalline disorder, heterojunction band offsets (i.e., CZTS(Se)/CdS/ZnO), or other device imperfections including the formation of secondary phases within the absorber layer.

CZTS(Se) Solar Cell Performance Disparity

Even though sufficient charge carrier generation and separation may occur within CZTSSe, recombination of electron and hole pairs before sufficient separation and collection to the external circuit limits the device performance. For comparison, the close cousin material CIGSe has a similar tetragonal crystalline structure and band gap, and the device architecture is almost identical to that for CZTS(Se), but the record CZTSSe solar cell device efficiency is only 12.6% [17], whereas the 20.8% CIGSe device record efficiency [18] is almost double. A comparison of two solar cells, a 10.1% efficient CZTSSe device and a 15.1% efficient CIGSSe device, both deposited by the same laboratory with the same techniques, reveals that the CIGSSe device outperforms the CZTSSe on every major device characteristic used to define a solar cell's performance. The largest performance disparity between the close cousins is the 15% lower open-circuit

voltage (V_{OC}) in CZTSSe [19].

The V_{OC}, the voltage at zero current, is the maximum voltage available to the device. Because losses in V_{OC} arise from increased reverse saturation current, it can also be viewed as a metric of the recombination occurring within the device. V_{OC} losses within CZTSSe devices indicate that defects that lie near the middle of the CZTSSe band gap (deep defects) may be acting as recombination centers. These defects may occur in the bulk, interfaces, or grain boundaries of the absorber layer.

Defects may act as recombination centers and lower the minority carrier lifetime and reduce the light-generated current. Using three different methods, Repins et al. measure the minority carrier lifetime of 9.4% efficient CZTSe devices to be 2-3 ns [20]. The lifetime of high-efficiency CIGSe on the other hand is >100 ns [21]. Even commercial CIGSe devices have >30 ns minority carrier lifetimes. Device modeling studies attribute the majority of voltage loss of CZTSe devices to be a result of short minority carrier lifetime, however, the V_{OC} of the device model is still higher than that of the actual device. This indicates other mechanisms of voltage loss also account for lower CZTSe device efficiencies [20].

Experts studying kesterite and chalcopyrite materials and solar cell devices met in January 2013 to identify research goals for kesterite photovoltaics that would expedite achieving >18% efficient devices. To address the primary cause for lagging efficiencies, the V_{OC} deficit, meeting participants identified three high-impact research areas: defect characterization and passivation, phase stability and process control, and interface optimization [22]. The research in this dissertation addresses defect characterization and phase analysis.

Secondary Phase Formation in CZTS(Se)

The compositional range for thermodynamic stability of the pure CZTS phase is only a few mol % wide for Cu, Zn, and Sn variation at temperatures relevant for film synthesis (i.e., the 670 K isotherm in [23]), and there is a high likelihood that secondary phases including Cu_xS, Sn_xS_y, Cu_xSnS_y, and ZnS will form during film synthesis. To further complicate phase stability, the quaternary compound also readily decomposes into binary $Cu_{2-x}S$ and ZnS as a result of SnS evaporation [24]. The secondary phases and defects that result from compositional variation both positively and negatively affect CZTSSe devices.

ZnS(Se) phase presence both lowers the V_{OC} of a device [25] and also blocks charge collection due to band structure misalignment [26]. Even though ZnS(Se) phase precipitation lowers CZTS(Se) device performance [27], a final Zn-rich, Cu-poor film composition yields higher device efficiencies [28]. A postulated benefit to the secondary phases ZnS(Se) and $Cu_2SnS(Se)_3$ (CTS(Se)), which have similar zinc-blend based crystalline structures to CZTS(Se), is grain boundary passivation [29] by reducing strain and lowing recombination velocities at the grain interfaces. Although CTS(Se) may positively alter grain boundaries, its lower bandgap (0.8-0.9 eV for CTS and 0.4 eV for CTSe) [30] may reduce overall solar cell efficiency. The flake-like grain structure of SnS on the surface of the solar cell will also cause problems with adhesion and cause insufficient electrical contact between the morphologically rough CZTS/SnS/CdS layer and the ZnO that is typically sputtered on for the transparent conducting oxide [31] (Figure 1.1). Chapter 4 presents characterization of secondary phases that are either miscible or immiscible within the main CZTS(Se) film and examines their presence relative to film

composition. Composition variation in CZTS(Se) not only affects the secondary phase formation, but also affects defect formation and concentration, which controls the doping, electrical, and optical behaviors of the absorber layer.

Defects in CZTS(Se)

The pentenary nature of CZTSSe lends itself to a wide variety of defects including vacancy, interstitial, and antisite defects. Following Kroger-Vink notation, the defects are written as M_S where M is the species (vacancy, interstitial, or atom), and S is the lattice site. For example, the vacancy on a copper site is written as V_{Cu}, and a Sn atom on a Zn lattice site is written Sn_{Zn}. In most cases herein, the charge of the defect is left off of the notation. The predicted charge transfer levels for defects most likely to form in CZTS and CZTSe [12], [22] are shown in Figure 1.4.

CZTS(Se) is natively p-type due to the high concentration of Cu_{Zn} and V_{Cu} defects that act as electron acceptors and are ionized at room temperature. The concentration of these defects are predicted to depend on the Cu/(Zn+Sn) and Zn/Sn ratios or chemical potentials of the elements depending on the synthesis method [12]. Defects which lie near the band edge have low enough energies to be ionized at room temperature and are called shallow states. This demarcation energy is approximately k_BT=25 meV (k_B is the Boltzmann's constant and temperature T=300K). These shallow defects consist of electron(s) weakly bound by a Coulomb potential which are localized, but to a rather large volume of the crystal (up to thousands of lattice spacings), that can ionize to the extended states of the crystal. Conversely, defects with electrons or holes having ionization energies larger than a few k_BT, are more strongly localized by the impurity potential [32]. These deep states have more deleterious consequences to the solar cell efficiency since they are

more likely to trap free carriers for long times and possibly act as recombination centers if the opposite polarity carrier is trapped before the first is remitted. As a general rule, the closer a trap lies to midgap, the more likely it is to act as a recombination center, however, the capture and emission cross sections also play a role.

Deeper states within CZTS(Se) have been measured by methods including thermal admittance spectroscopy (TAS) [33]–[36], deep level transient spectroscopy (DLTS) [36], transient photocapacitance [37], current mode DLTS [38], time-resolved photoluminescence [36], deep level capacitance profiling [34], and indirectly by measuring the effect on photoluminescence (PL) [31], [39]–[41]. States from 30 meV to >637 meV have been attributed to acceptors that range from shallow to deep [31], [33], [34], [36], [38], [42], [43], and an optically active defect at ~400 meV has been attributed to a quasi-donor/acceptor pair [40]. However, to date, no electron traps or defect-assisted nonradiative recombination centers have been reported in CZTS(Se) literature. Chapter 3 presents the results of DLTS research showing evidence for a deep electron trap near the CZTSSe midgap, which is highly suggestive that carrier recombination may be assisted by deep traps within CZTS(Se).

Defects within CZTS(Se) may also form charge neutral groupings which convert defects that would otherwise trap or assist in recombination into electrically benign clusters. For example, the defect complex predicted to have the lowest formation energy is the antisite pair [Cu_{Zn}^{-} + Zn_{Cu}^{+}]. This antisite defect complex, with a formation energy of 0.2 eV, is a unitary element that can be used to switch between the kesterite and stannite polymorphs polymorphsas discussed previously. The overall impact on the electronic and optical properties in forming this defect complex is weak, however, the difference between

the bandgap of the stannite and kesterite polymorphs does raise questions as to the overall effects on CZTS(Se) device performance. Chapter 5 presents the results of modeling polymorph variation within a CZTS solar cell, and presents the findings that placing kesterite at the interface and stannite within the bulk of the absorber layer increases the overall solar cell efficiency.

Even though some stoichiometric complexes are fairly benign, not all complexes that conserve stoichiometry can be considered harmless. For example, the [Zn_{Sn} + Sn_{Zn}] cluster decreases the band gap by 0.3 eV in Cu_2ZnSnS_4 and 0.1 eV in $Cu_2ZnSnSe_4$ [12], which may indicate a lower V_{OC} and higher tendency for carrier trapping. Although their formation energy is predicted to be fairly high and thus their total concentration should be relatively low, evidence for increased film disorder and lower photoluminescence is presented in Chapter 4. This highlights the problem with the common assumption that excess Sn flux during CZTS(Se) film deposition to prevent SnS(Se) losses from the films does not impact the Sn-related defect population within the absorber layer.

Experimental results from stoichiometric variation of CZTS(Se) within solar cells indicate higher device efficiencies for compositions of Cu/(Zn + Sn) ≈ 0.8 and Zn/Sn ≈ 1.2. Calculated defect formation energies and concentrations indicate several non-stoichiometric defect complexes may contribute to this observation [12]. The three nonstoichiometric defect clusters predicted to have the lowest formation energies are [$2Cu_{Zn}^{-}$ + Sn_{Zn}^{2+}], [V_{Cu}^{-} + Zn_{Cu}^{+}], and [Zn_{Sn}^{2-} + $2Zn_{Cu}^{+}$]. The defect cluster [$2Cu_{Zn}^{-}$ + Sn_{Zn}^{2+}] causes a downshift in the CBM which may encourage electron trapping, whereas the other two complexes have little effect on the VBM or CBM. Therefore a Cu-poor and Zn-rich film may avoid the more deleterious defect complexes in favor of more electrically

benign albeit off-stoichiometry complexes. Both Chapters 3 and 4 explore the implications of Sn-related defects as well as minority carrier trapping, which may provide some further insight into defect formation within CZTS(Se).

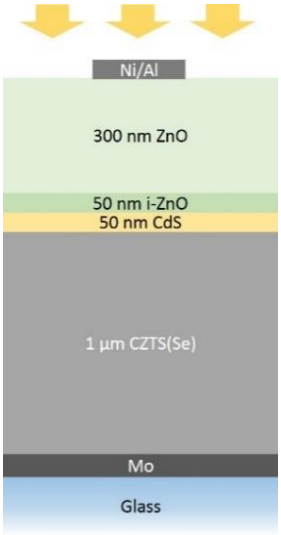

Figure 1.1. Cross-section of a typical CZTS(Se) solar cell device. This substrate configuration is illuminated on the front side of the diode. Charge carriers are generated and separated within the CZTS absorber layer. Holes are collected at the back contact (Mo), and electrons are collected at the front contact (Ni/Al). Cross-section of a typical CZTS(Se) solar cell device showing all layers that comprise a full device.

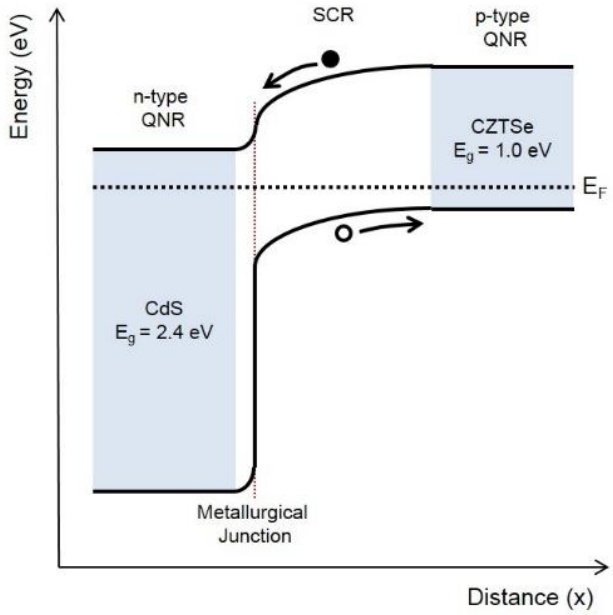

Figure 1.2. Band diagram of CdS/CZTSe p-n junction. The junction is in equilibrium with no applied bias. Quasineutral regions (QNR) are shown in blue for both n-type CdS and p-type CZTSe. The space-charge region (SCR) extends primarily into the lower-doped CZTSe. Electrons (black dot) and holes (black circle) generated in the SCR drift to the front and back contacts respectively due to the energetic difference on the conduction and valence bands of CdS and CZTSe.

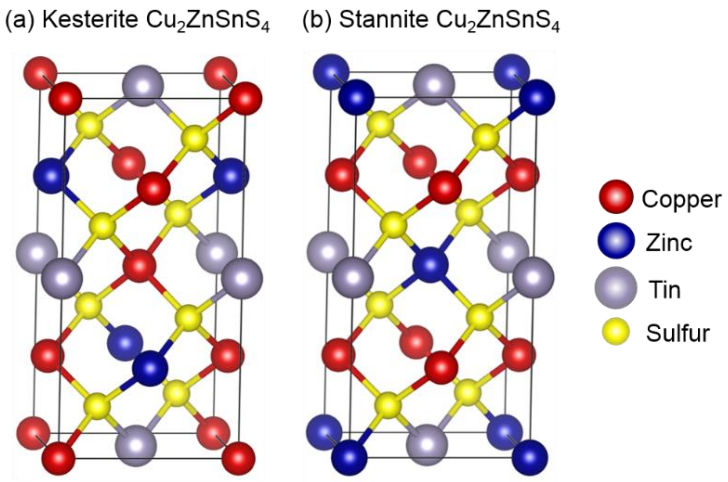

Figure 1.3. Polymorphs of CZTS. (a) Kesterite and (b) stannite differ only in Cu and Zn cation arrangement.

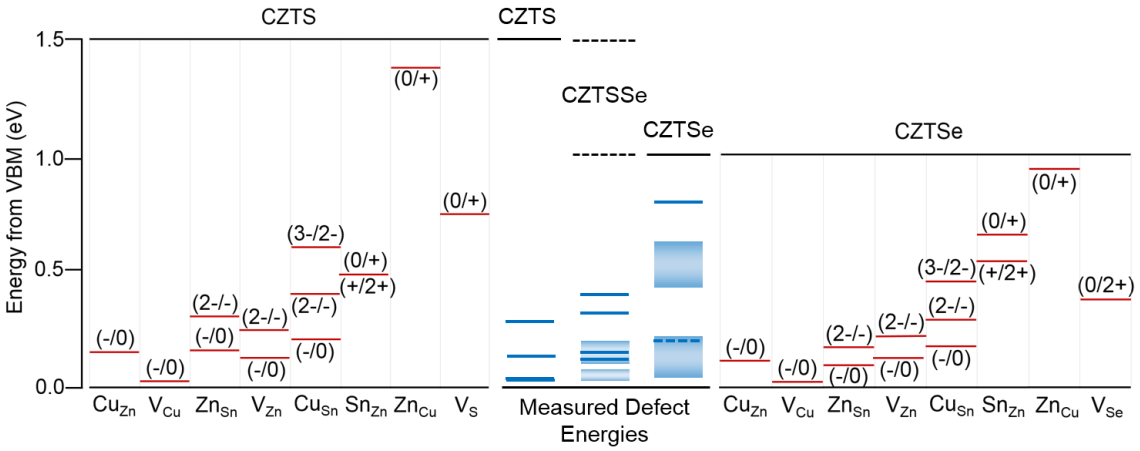

Figure 1.4. Measured and calculated defect ionization energies for CZTS(Se). Calculated ionization energies for CZTS and CZTSe [12] are represented by red lines and labeled with the change in charge states. Experimentally determined values of defect energies in CZTS, CZTSSe with varying S/Se ratios, and CZTSe are represented by blue lines or bands and are reported in [31], [38], [39], [42] (CZTS), [33]–[35], [38], [40], [41] (CZTSSe), and [36], [37] (CZTSe). The energy is given with respect to the valence band maximum (VBM). The conduction band minimum varies from 1.5 for CZTS to 1.0 for CZTSe and changes depending on the S/Se ratio for CZTSSe.

References

[1] J. Conti et al., “International Energy Outlook 2013,” U.S. Energy Inform. Admin., Washington, DC, Rep. DOE/EIA-0484(2013), July 2013.

[2] R. Gelman, “2012 Renewable Energy Data Book,” National Renewable Energy Lab, Golden, CO, Rep. DOE/GO-102013-4291, Oct. 2013.

[3] B. Burger et al., “Fraunhofer ISE: Photovoltaics Report (2014),” Freiburg, Germany, July 28, 2014.

[4] P. C. K. Vesborg and T. F. Jaramillo, “Addressing the terawatt challenge: Scalability in the supply of chemical elements for renewable energy,” *RSC Adv.*, vol. 2, no. 21, p. 7933, 2012.

[5] C. A. Wolden et al., “Photovoltaic manufacturing: Present status, future prospects, and research needs,” *J. Vac. Sci. Technol. A Vacuum, Surfaces, Film*, vol. 29, no. 3, p. 030801, 2011.

[6] M. A. Green et al., “Solar cell efficiency tables (version 44),” *Prog. Photovoltaics Res. Appl.*, vol. 22, no. 7, pp. 701–710, Jul. 2014.

[7] S. Krum et al., (2014 Aug. 5). *First solar builds the highest efficiency thin film PV cell on record*. [Online]. Available: http://investor.firstsolar.com/releasedetail.cfm?ReleaseID=864426.

[8] P. Jackson et al., “Compositional investigation of potassium doped Cu(In,Ga)Se2 solar cells with efficiencies up to 20.8%,” *Phys. Status Solidi - Rapid Res. Lett.*, vol. 8, no. 3, pp. 219–222, Mar. 2014.

[9] V. M. Fthenakis, “Overview of potential hazards,” in *Practical Handbook of Photovoltaics: Fundamentals and Applications*, vol. 32, no. 1, T. Markvart and L. Castañer, Eds. Elsevier B.V., 2003, pp. 857–868.

[10] B. Shin et al., “Thin film solar cell with 8.4% power conversion efficiency using an earth-abundant Cu2 ZnSnS4 absorber,” *Prog. Photovoltaics Res. Appl.*, vol. 21, no. 1, pp. 72–76, Jan. 2013.

[11] A. Redinger et al., “Influence of S/Se ratio on series resistance and on dominant recombination pathway in Cu2ZnSn(SSe)4 thin film solar cells,” *Thin Solid Films*, vol. 535, pp. 291–295, May 2013.

[12] S. Chen et al., “Classification of lattice defects in the kesterite Cu2ZnSnS4 and Cu2ZnSnSe4 earth-abundant solar cell absorbers,” *Adv. Mater.*, vol. 25, no. 11, pp. 1522–39, Mar. 2013.

[13] C. Persson, “Electronic and optical properties of Cu2ZnSnS4 and Cu2ZnSnSe4,” *J. Appl. Phys.*, vol. 107, no. 5, p. 053710, 2010.

[14] S. Chen et al., “Crystal and electronic band structure of Cu2ZnSnX4 (X=S and Se) photovoltaic absorbers: First-principles insights,” *Appl. Phys. Lett.*, vol. 94, no. 4, p. 041903, 2009.

[15] W. Shockley and H. J. Queisser, “Detailed balance limit of efficiency of p-n junction solar cells,” *J. Appl. Phys.*, vol. 32, no. 3, p. 510, 1961.

[16] D. A. Neamen, “Introduction to the quantum theory of solids,” in *Semiconductor Physics and Devices*, 3rd ed., McGraw-Hill Companies, 2002, pp. 34–74.

[17] W. Wang et al., “Device characteristics of CZTSSe thin-film solar cells with 12.6% efficiency,” *Adv. Energy Mater.*, vol. 4, no. 7, May 2014.

[18] A. J. Jackson and A. Walsh, “Abinitio thermodynamic model of Cu2ZnSnS4,” *J. Mater. Chem. A*, vol. 2, no. 21, p. 7829, 2014.

[19] D. B. Mitzi et al., “Prospects and performance limitations for Cu-Zn-Sn-S-Se photovoltaic technology,” *Philos. Trans. A. Math. Phys. Eng. Sci.*, vol. 371, no. 1996, p. 20110432, Aug. 2013.

[20] I. L. Repins et al., “Indications of short minority-carrier lifetime in kesterite solar cells,” *J. Appl. Phys.*, vol. 114, no. 8, p. 084507, 2013.

[21] W. K. Metzger et al., “Recombination kinetics and stability in polycrystalline Cu(In,Ga)Se2 solar cells,” *Thin Solid Films*, vol. 517, no. 7, pp. 2360–2364, Feb. 2009.

[22] A. Polizzotti et al., “The state and future prospects of kesterite photovoltaics,” *Energy Environ. Sci.*, vol. 6, no. Advance Article, 2013.

[23] I. Olekseyuk et al., “Phase equilibria in the Cu2S–ZnS–SnS2 system,” *J. Alloys Compd.*, vol. 368, no. 1–2, pp. 135–143, Apr. 2004.

[24] J. J. Scragg et al., “Chemical insights into the instability of Cu2ZnSnS4 films during annealing,” *Chem. Mater.*, vol. 23, no. 20, pp. 4625–4633, Oct. 2011.

[25] K. Wang et al., “Structural and elemental characterization of high efficiency Cu2ZnSnS4 solar cells,” *Appl. Phys. Lett.*, vol. 98, no. 5, p. 051912, 2011.

[26] J. Timo Wätjen et al., “Direct evidence of current blocking by ZnSe in Cu2ZnSnSe4 solar cells,” *Appl. Phys. Lett.*, vol. 100, no. 17, p. 173510, 2012.

[27] A. Fairbrother et al., “Development of a selective chemical etch to improve the conversion efficiency of Zn-rich Cu2ZnSnS4 solar cells,” *J. Am. Chem. Soc.*, vol. 134, no. 19, pp. 8018–21, May 2012.

[28] A. Walsh et al., “Crystal structure and defect reactions in the kesterite solar cell absorber Cu2ZnSnS4 (CZTS): Theoretical insights,” in *American Institute of Physics Conference Proceedings*, 2011, vol. 4, pp. 63–64.

[29] B. G. Mendis et al., “The role of secondary phase precipitation on grain boundary electrical activity in Cu2ZnSnS4 (CZTS) photovoltaic absorber layer material,” *J. Appl. Phys.*, vol. 112, no. 12, p. 124508, 2012.

[30] Y.-T. Zhai et al., “Structural diversity and electronic properties of Cu2SnX3(X=S, Se): A first-principles investigation,” *Phys. Rev. B*, vol. 84, no. 7, p. 075213, Aug. 2011.

[31] J. P. Leitão et al., “Photoluminescence and electrical study of fluctuating potentials in Cu2ZnSnS4-based thin films,” *Phys. Rev. B*, vol. 84, no. 2, p. 024120, Jul. 2011.

[32] P. Blood and J. W. Orton, *The Electrical Characterization of Semiconductors: Majority Carriers and Electron States*. San Diego, CA: Academic Press, 1992.

[33] D. A. R. Barkhouse et al., “Device characteristics of a 10.1% hydrazine-processed Cu2ZnSn(Se,S)4 solar cell,” *Prog. Photovoltaics Res. Appl.*, vol. 20, no. 1, pp. 6–11, Jan. 2012.

[34] O. Gunawan et al., “Electronic properties of the Cu2ZnSn(Se,S)4 absorber layer in solar cells as revealed by admittance spectroscopy and related methods,” *Appl. Phys. Lett.*, vol. 100, no. 25, p. 253905, 2012.

[35] H.-S. Duan et al., “The role of sulfur in solution-processed Cu2ZnSn(S,Se)4 and its effect on defect properties,” *Adv. Funct. Mater.*, vol. 23, no. 11, pp. 1466–1471, Mar. 2013.

[36] J. V. Li et al., “Effects of sodium incorporation in co-evaporated Cu2ZnSnSe4 thin-film solar cells,” *Appl. Phys. Lett.*, vol. 102, no. 16, p. 163905, 2013.

[37] D. W. Miller et al., “Electronically active defects in the Cu2ZnSn(Se,S)4 alloys as revealed by transient photocapacitance spectroscopy,” *Appl. Phys. Lett.*, vol. 101, no. 14, p. 142106, 2012.

[38] S. Das et al., “Defect levels in Cu2ZnSn(SxSe1−x)4 solar cells probed by current-mode deep level transient spectroscopy,” *Appl. Phys. Lett.*, vol. 104, no. 19, p. 192106, May 2014.

[39] M. Grossberg et al., “The role of structural properties on deep defect states in Cu2ZnSnS4 studied by photoluminescence spectroscopy,” *Appl. Phys. Lett.*, vol. 101, no. 10, p. 102102, 2012.

[40] T. Gershon et al., “Photoluminescence characterization of a high-efficiency Cu2ZnSnS4 device,” *J. Appl. Phys.*, vol. 114, no. 15, p. 154905, 2013.

[41] E. Kask et al., “Deep defects in Cu2ZnSnS4 monograin solar cells,” *Energy Procedia*, vol. 10, pp. 261–265, Jan. 2011.

[42] A. Nagaoka et al., “Growth and characterization of Cu2ZnSnS 4 single crystals,” *Phys. Status Solidi*, vol. 210, no. 7, pp. 1328–1331, Jul. 2013.

[43] E. Kask et al., “Defect studies in Cu2ZnSnSe4 and Cu2ZnSn(Se0.75S0.25)4 by admittance and photoluminescence spectroscopy,” *Mater. Sci. Semicond. Process*, vol. 16, no. 3, pp. 992–996, Jun. 2013.

CHAPTER 2

CAPACITANCE SPECTROSCOPY

Temperature Admittance Spectroscopy

Temperature admittance spectroscopy (TAS) can be used to determine the apparent energy levels and capture cross sections of shallow majority carrier traps, estimate the free carrier concentration, determine the temperature range for DLTS measurements, and may be used to troubleshoot interferences from secondary junctions.

Admittance is a complex quantity, with the conductance and capacitance related to the real and imaginary parts of the admittance. Temperature admittance spectroscopy is a measurement of the capacitance and conductance of a junction as a function of the frequency (ω) of AC voltage oscillation. Majority carrier (hole) traps within the p-type CZTSSe band gap within the depletion region where the Fermi level (E_F) crosses the defect charge transition level (E_T) may be able to change their occupation state depending on the temperature (T) and ω of measurement and the emission rate (e_p) of holes from the trap. The threshold frequency, or the frequency at which the trap ceases to respond and the junction admittance changes, is governed by the emission and capture rates of the trap being stimulated. If the frequency or the temperature changes so the trap can no longer respond, the trap occupation changes and hence causes a measurable change in capacitance. At lower frequencies, the trap will be able to follow the AC voltage frequency and capture and emit the carrier within one cycle. Since the trap emits holes by thermal excitation, as the temperature increases, the emission rate also increases. Therefore, the capacitance step

occurs at higher frequencies for higher temperatures. If $e_p < \omega$, at low temperatures and high frequencies, then the trap cannot respond to the voltage stimulus. If $e_p > \omega$, then the majority trap can emit and capture holes with capture (c_p) and emission rates defined by the equations 2.1 and 2.2 [1].

$$c_p(T) = \sigma_p(T)\langle \nu_p(T)\rangle p(T) \tag{2.1}$$

$$e_p(T) = c_p(T)\exp\left(\frac{-E_T}{kT}\right) \tag{2.2}$$

These rates include both characteristics of the bulk material, carrier average thermal velocity $\langle \nu_p \rangle$ and free hole concentration p, as well as properties unique to the trap itself, capture cross-section σ_p and energy level within the band gap that corresponds to the charge transition E_T. This energy E_T is referenced to the relevant band edge, which is the valence band edge in the case for hole capture in p-type CZTSSe. The resulting signal is a step in capacitance or a peak in conductance at the demarcation energy where $e_p = \omega$. Using this equality in equation 2.2, the demarcation energy ω_{max} is now defined by equation 2.3. The temperature dependence of $\langle \nu_p \rangle$ and p are moved to the left hand side of the equation, and the A term accounts for the remaining factors within the capture rate (equation 2.1).

$$\frac{\omega_{max}}{T^2} = ln\mathrm{A} - \frac{E_T}{kT} \tag{2.3}$$

Measurements are made by observing the capacitance of a junction excited with an oscillating AC voltage with a set amplitude over a varying frequency range. Typical measurement AC voltage is ~k_BT/q or 25-50 mV, and the frequency range of our instrumentation is 20 Hz-1 MHz. Capacitance vs. ω curves are then collected over a temperature range, typically from 100-335 K, yielding a data set like the simplified

example shown in Figure 2.1 (a). The derivative of the capacitance with respect to temperature is then plotted as seen in Figure 2.1 (b), and the corresponding (ω, T_{max}) points are plotted on an Arrhenius plot like the one shown in Figure 2.1 (c). The Arrhenius equation (2.3) is derived from $e_p(T)$, and ω=e_p at T_{max}. The slope is proportional to the apparent trap energy, and the intercept is used to obtain the temperature-independent apparent σ_p. The trap signature, which is the apparent E_T and σ_p, is not the absolute trap energy and capture cross section due to possible unaccounted-for entropy effects and temperature dependencies of σ_p. Other phenomena including band discontinuities or back contact barriers for example, can also produce apparent trap signatures. Therefore, the interpretation of the trap signature must be approached with care.

Deep Level Transient Spectroscopy

Unlike TAS measurements taken with a sinusoidally oscillating test signal, deep level transient spectroscopy (DLTS) is a transient capacitance decay measurement driven by an abrupt change in voltage or light bias. Like DLTS, TAS is also used to calculate the apparent capture cross section and trap energy of defects of a semiconductor in a p-n junction. DLTS is more sensitive to lower concentrations of traps and can characterize deeper traps than those detected by TAS. The capacitance of a p-n junction can be altered by filling or emptying traps of charge carriers. The capacitance (C) of the p-n junction is inversely proportional to the square root of the applied voltage (V) and directly proportional to the square root of the ionized impurity density in the space-charge region (N_{SCR}) [2] as shown by equation 2.4. The space charge density is the sum of all ionized defects including the shallower ionized acceptor N_A^-, ionized majority trap N_T^+, and ionized minority traps N_T^- concentrations as shown by equation 2.5. (These descriptions, charges, and equations

are assuming a p-type material and N_{SCR} is uniform versus distance.)

$$C = A\sqrt{\frac{q\varepsilon_S\varepsilon_0 N_{SCR}}{2(V_{bi}-V)}} \tag{2.4}$$

$$N_{SCR} = N_A^- - N_T^+ + N_T^- \tag{2.5}$$

Both deep and shallow traps contribute to N_{SCR}. The trap occupation can also be altered by light, temperature, and/or applied bias voltage to the junction. The easiest DTLS measurement is the majority carrier emission, which is the emission of holes from a trap in p-type CZTS(Se). This majority carrier emission measurement consists of a "filling pulse" followed by a "measurement" time period. Typically, traps are filled by applying zero or forward bias voltage to the p-n junction, which results in decreasing the width of the space charge region within the CZTS(Se). Then the junction is abruptly switched to reversed bias, and the decay in capacitance is measured as a function of time. This change from forward to reversed bias changes the band bending of the conduction and valence bands, and alters the trap occupation. Figure 2.2 demonstrates these concepts.

From the collective data set, an apparent capture cross section (σ_p) and trap energy (E_T) are calculated in a similar manner to TAS. The rate window (time over which the capacitance difference is measured) is varied instead of the frequency for the Arrhenius plot. The rate window is related to e_p by equation 2.6 [2] in which t_1 and t_2 are the first and second times the capacitance is taken for the rate window and emission rate calculations. Figure 2.3 demonstrates how the raw transients measured at a range of temperatures are analyzed to determine σ_p and E_T [2], [3].

$$e_p = \frac{\ln t_2/t_1}{t_2 - t_1} \tag{2.6}$$

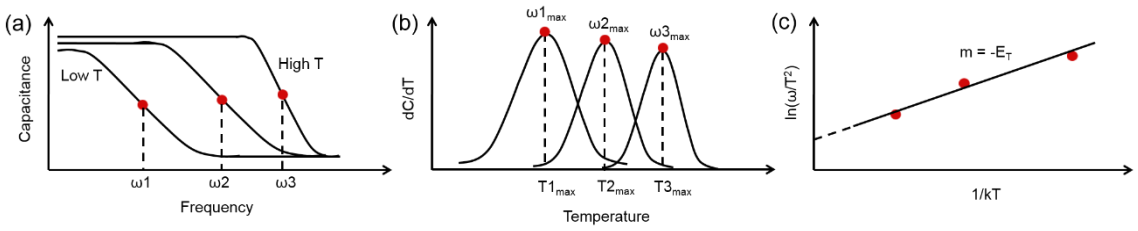

Figure 2.1. TAS analysis steps. Temperature admittance spectroscopy analysis steps start with (a) raw data and show how to (b) identify (ω, T_{max}) points and then (c) calculate the trap energy and capture cross section from the Arrhenius plot.

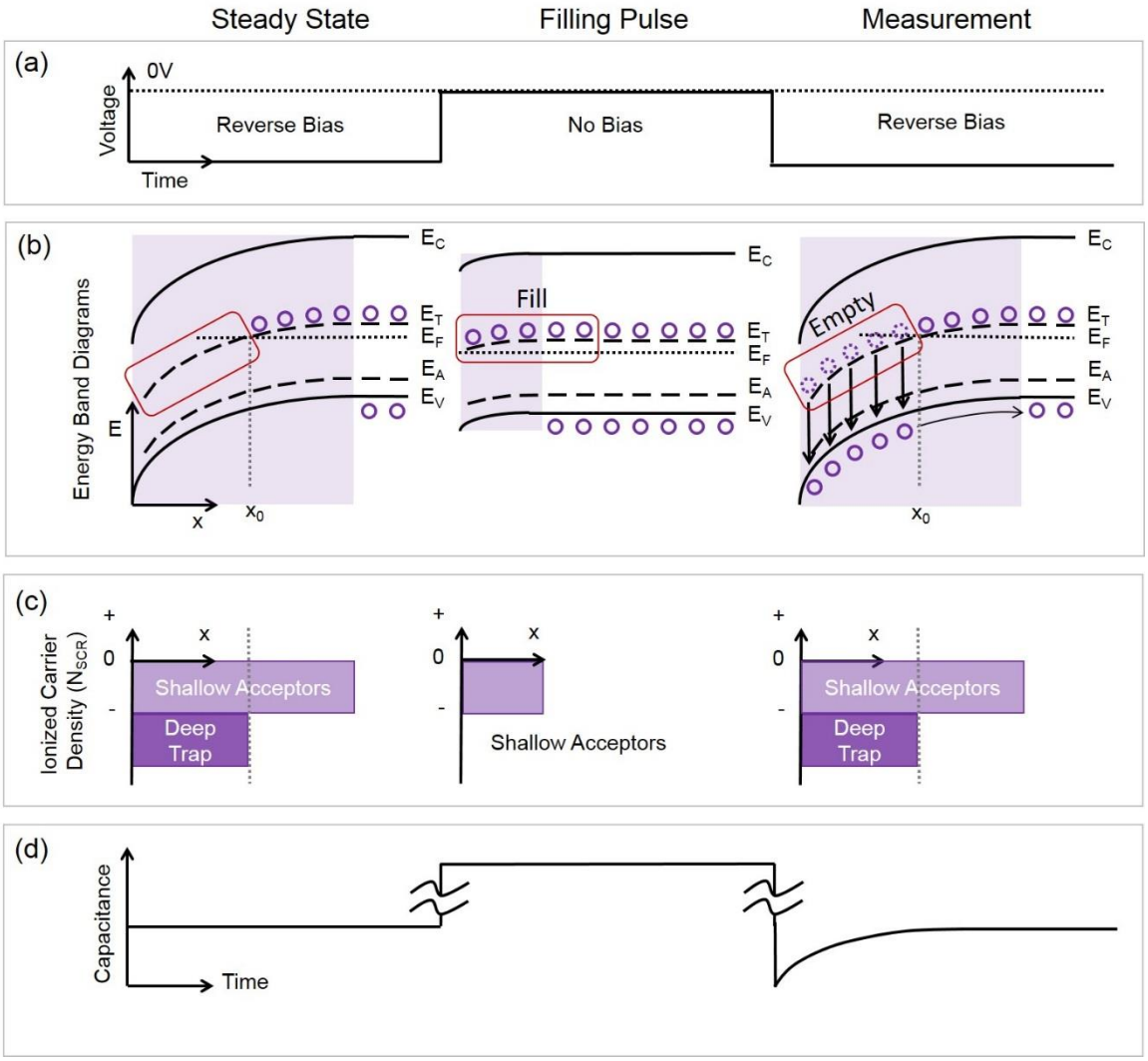

Figure 2.2. Diagram of the steady state, filling pulse, and measurement conditions for majority carrier emission DLTS measurements. This diagram illustrates processes occurring in the p-type material of an n^+-p junction. (a) Displays the voltage conditions. (b) Displays the energy band diagrams with the space-charge region highlighted in purple. Traps below the Fermi level (E_F) are unoccupied by holes and negatively charged. Traps above E_F are occupied and neutral. During the zero bias voltage filling pulse, the space-charge region is shortened due to decreased band bending, and traps are filled. During the reverse bias measurement, the previously filled traps emit holes (majority carrier). (c) Shows the ionized carrier density in the space-charge region (N_{SCR}) that results from the shallow acceptors (at energy E_A in (b)) and the deep traps (at energy E_T in (b)). The negative space-charge density decreases due to deep trap neutralization during the filling pulse, and it increases again during the transient measurement. (d) Shows the capacitance response for all three conditions, with the increased capacitance during the filling pulse resulting from the smaller SCR, and the increasing transient during the measurement results from traps ionizing as they empty of holes.

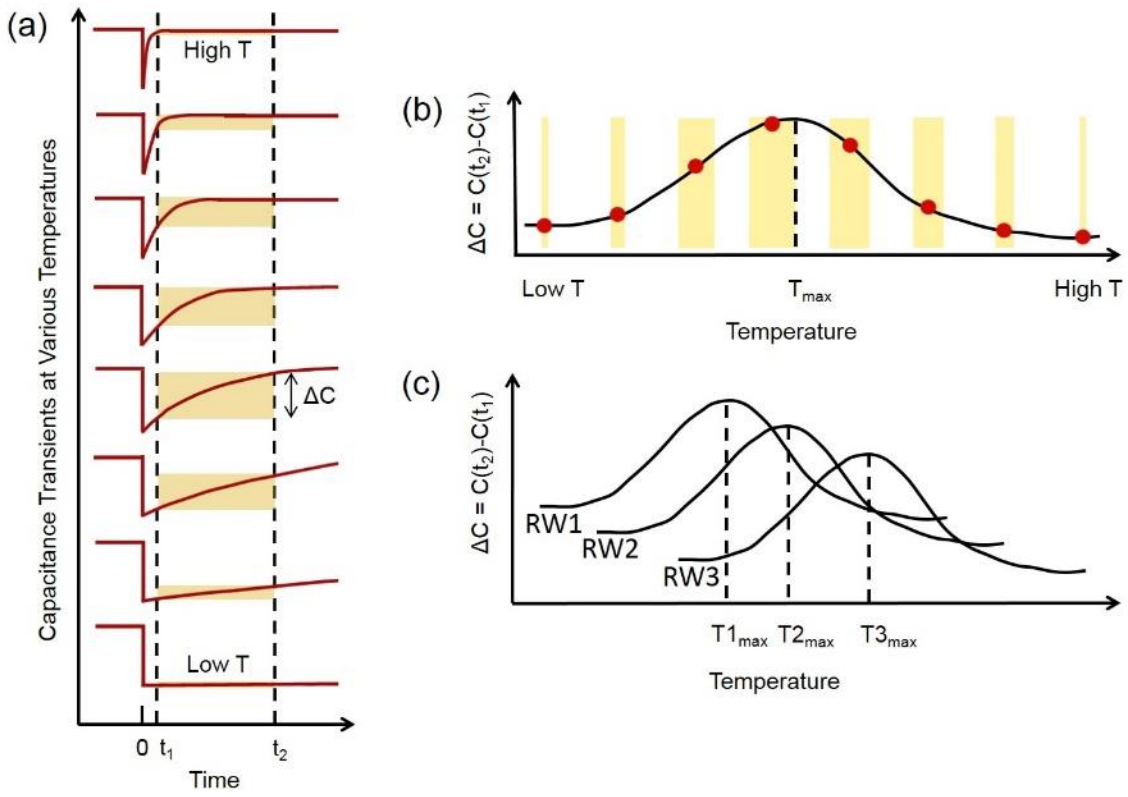

Figure 2.3. Example of DLTS data calculations. The example shown is expected for a DLTS measurement of emission of a majority carrier from a deep trap. (a) Displays the capacitance transients from high to low temperature. The capacitance quickly returns to the steady-state capacitance at high temperature, and returns very slowly at low temperature. At both extremes, the magnitude in the change of capacitance (ΔC) is very small. A midrange temperature shows a much higher ΔC shown by the height in (a) or width of the yellow bar in (b). (b) Plot of the ΔC shown in (a) as a function of temperture. (c) Shows several ΔC(T) curves for various rate windows (t_2-t_1). The maxima of these curves are used to obtain (e_p,T) points for an Arrhenius plot like the one shown in Figure 2.1 (c).

References

[1] P. Blood and J. W. Orton, *The Electrical Characterizatioin of Semiconductors: Majority Carriers and Electron States*. San Diego, CA: Academic Press, 1992.

[2] D. V. Lang, "Deep-level transient spectroscopy: A new method to characterize traps in semiconductors," *J. Appl. Phys.*, vol. 45, no. 7, pp. 3023–32, 1974.

[3] D. V. Lang et al., "Measurement of the density of gap states in hydrogenated amorphous silicon by space charge spectroscopy," *Phys. Rev. B*, vol. 25, no. 8, pp. 5285–5319, 1982.

CHAPTER 3

OBSERVATION OF A MINORITY CARRIER DEEP DEFECT IN CZTSSE

Abstract

Thin film solar cells using $Cu_2ZnSn(S,Se)_4$ (CZTSSe) as the light absorber have promise as a technology scalable to terawatt installed photovoltaic generating capacity without significant raw materials price increases caused by scarcity. However, to date, even near-record efficiency CZTSSe devices exhibit large open circuit voltage (V_{OC}) deficits and short minority carrier lifetimes. To investigate the origins of this V_{OC} loss, we used junction capacitance spectroscopy to explore the underlying causes of nonradiative recombination in CZTSSe devices. Deep level transient spectroscopy (DLTS) in reverse bias was used for the first time to identify a midgap defect capturing and emitting minority electrons in the depletion width of devices based on selenized Cu_2ZnSnS_4 nanoparticle ink absorber layers. This state is 590 meV from the conduction band edge with an energy distribution approximately 170 meV wide and has an apparent electron cross section approximately 2×10^{14} cm^2. These characteristics make it likely that this state can contribute to low minority carrier lifetime and reduced V_{OC} in operating photovoltaic devices and we investigate the extent of such effects.

Introduction

The semiconductor $Cu_2ZnSn(S,Se)_4$ (CZTSSe) is an alternative photovoltaic material used in thin film solar cell devices to circumvent supply and price bottlenecks concerns of indium and tellurium [1]. CZTSSe has a decent absorption coefficient and a bandgap tunable from 1-1.5 eV depending on the selenium to sulfur ratio. Although the earth-abundant components and ideal material properties make CZTSSe a great candidate for possible scale-up to terawatt photovoltaic power systems, the record CZTSSe device efficiency of 12.6% [2] lags those of CdTe 21.0% [3] and CIGSSe 20.8% [4]. The main performance disparity between CZTSSe and CIGSSe, which have similar bandgaps for record devices, is the lower open circuit voltage (V_{OC}) in CZTSSe. The CZTSSe record efficiency device has a 617 mV V_{OC} deficit [2] as compared to a 356 mV V_{OC} deficit for CIGSSe [4].

Three factors are suspected to lower V_{OC} in CZTSSe devices: 1) defect mediated recombination, 2) band tails, and 3) cliffs or spikes in the band alignment of the CdS/CZTSSe heterojunction [1]. The first two factors are related to defects which result from crystalline disorder. These defects and defect aggregates may have localized or partially-localized electrostatic potentials that may be distributed homogeneously or inhomogeneously within grains or may exist only at interfaces and grain boundaries [5]–[7]. The quaternary or pentenary nature of CZTSSe lends itself to a wide variety of native vacancy, interstitial, and antisite defects [8]. If the defect energies lie relatively close to the band edges, they will dope the material but an aperiodic spatial distribution will also contribute to band tails.

Band tails lower the V_{OC} by decreasing the effective band gap for absorption

compared to that for transport [7]. The defect states that give rise to band tails are more electrostatically localized and extend beyond the conduction and valence band mobility edges into the band gap of CZTSSe. The electron hole pairs generated at these more localized sites by light whose energy corresponds to this decreased effective band gap do not contribute to the overall photocurrent produced since these carriers cannot be swept away into the conduction or valence bands. Band tails also induce lateral fluctuations in the bandgap that assist in tunneling-enhanced recombination and further exacerbate defect-assisted recombination [9]. Band edge fluctuations can account for approximately 125 mV of the V_{OC} loss (This estimate is based on the ~80 meV bandgap fluctuation amplitude measured for CZTSSe [6], and equation 10 in Rau et al. [7]) Nonradiative recombination centers most likely also contribute to additional V_{OC} loss, although they have not yet been observed.

Defects whose energies lie near midgap are more likely to trap carriers and act as nonradiative recombination centers. This Shockley-Read-Hall (SRH) recombination lowers the minority carrier lifetimes within the absorber layer [10]. For co-evaporated CZTSe solar cells, short minority carrier lifetimes of a few ns [11] and increasing energies of Urbach band tail states [5], which are correlated with trap densities, have been implicated in decreasing $V_{OC.}$ Equations 3.1 and 3.2 show the relationship between V_{OC} and the minority carrier lifetime τ_n. In addition to decreasing the reverse saturation current J_O, smaller minority carrier lifetime can decrease the light-generated current J as well (Equation 3.3).

$$V_{OC} = \frac{nkT}{q} ln\left(\frac{J_{SC}}{J_0} + 1\right) \tag{3.1}$$

$$J_O = qn_i^2 \left(\sqrt{\frac{D_p}{\tau_p}} \frac{1}{N_D} + \sqrt{\frac{D_n}{\tau_n}} \frac{1}{N_A} \right) \tag{3.2}$$

$$J = J_O \left[\exp\left(\frac{qV}{nkT} - 1 \right) \right] \tag{3.3}$$

The temperature dependence of V_{OC} in solution-deposited CZTSSe devices also indicates significant recombination occurring at the CZTSSe/CdS interface [12], although some of this voltage loss may also be caused by bandgap fluctuations [6]. Many measured activation energies (E_a) ranging from 25 to 280 meV from the valence band edge (VBE) have been attributed to more shallow acceptor states in CZTS(Se) devices. These E_a are affected by Cu, S/Se, and Na content as well as sample aging [13]–[21]. Deeper defects have also been observed and attributed to 800 meV optical defects [5], which assist in radiative recombination, quasi donor/acceptor pairs at 400 meV [22], and deeper acceptors from 428 meV to >637 meV [20] (Figure 1.4).

Previous CZTSSe device studies cover a wide array of absorber layer deposition techniques including coevaporation, sulfur/selenization of metallic precursors, and hydrazine-processed CZTS(Se) (Figure 1.4). The most common measurement techniques used for defect characterization are capacitance spectroscopy methods that include thermal admittance spectroscopy (TAS), deep level transient spectroscopy (DLTS), drive level capacitance profiling (DLCP), and transient photocapacitance and transient photocurrent. Photoluminescence (PL) techniques measure radiative recombination, but nonradiative defect-assisted recombination is the main area of interest in determining the defects participating in SRH recombination which decreases V_{OC}. Although deep defects have been reported, only majority traps have been directly observed. Defect-assisted recombination centers have not yet been identified in CZTS(Se), although their presence

is likely. Capture of both electrons and holes must be observed, or the defect concentration and minority carrier lifetime must be correlated in order to conclude a defect acts as a recombination center.

In this work, we observe a near midgap defect behaving as a minority carrier trap within CZTSSe by measuring a $\eta = 7\%$ solar cell device containing a selenized CZTS nanoparticle ink absorber layer. From DLTS measurements, we determine the trap lies 590 meV from the conduction band edge and has an electron-attractive capture cross section of 2×10^{-14} cm^2. The DLTS signals observed are distinguished from non-Ohmic back contact responses. Admittance spectroscopy measurements show a temperature-dependent series resistance of the junction with an activation energy of 110 meV from the valence band edge and a neutral apparent capture cross section for holes of 6×10^{-17} cm^2. These observations provide direct evidence that midgap traps within CZTSSe are capable of trapping minority carriers and are very likely to act as recombination centers under forward biasing from illumination during device operation.

Experimental

CZTSSe Device Fabrication

The CZTSSe absorber layer in the reported solar cell devices were formed from CZTS nanoparticles annealed in a Se vapor. The CZTS nanocrystals were formed by reacting Cu, Sn, and Zn salts with sulfur in an oleylamine solution. This "nanoparticle ink" was then spread on a Mo/glass substrate, the solvent was evaporated, and the resulting CZTS nanocrystals were then annealed in a Se vapor to yield ~1 μm grains of CZTSSe. The device stack consisted of a Mo back contact on glass, ~1 μm CZTSSe, CdS, ZnO, indium tin oxide, and Ni/750 nm Al front contacts. The film synthesis and device

fabrication is described in [23], [24]. Original solar cell sizes were 0.48 cm^2, and 1.9 mm^2 subcells were scribed with a needle to obtain capacitance values within the measurement limits of the electrical characterization equipment.

Defect Characterization

Electrical spectroscopy measurements were performed using a system built by Semetrol and having an LCR meter (Quadtech 1920) for admittance spectroscopy and a fast capacitance bridge operating at 1 MHz (Boonton 7200) for deep level transient spectroscopy and CV. Samples were mounted on a copper stage within a closed-cycle cryostat with optical access. Temperatures were measured by a small Si diode held by a spring to the film side of the solar cell devices. Thermal and mechanical contact between the copper stage, sample, and temperature sensor was made using GE varnish. The impedances of the electrical connections to the sample were characterized and found to be negligible. A harmonic AC signal of 50 mV was used for temperature dependent admittance spectroscopy measurements from 20 Hz-1 MHz. Data collected at the lower frequencies are not reported due to excessive noise. Each capacitance (C) vs. f curve was collected at constant temperature (T) incremented by either 3 K or 5 K. Deep level transient spectroscopy involves the measurement of capacitance vs. time transients following step changes in electrical or light bias and is used to detect deep level defects. Each transient was measured at constant temperature at 3 K or 5 K increments. The capacitance measurements were made during -0.5 V reversed bias voltage after a 0 bias fill voltage pulse.

Results and Discussion

The physical and device characteristics of devices from the same batch of samples used in this study were previously reported [24]. Dark and illuminated J-V curves for both the full cell and the smaller scribed subcell in this study are shown in Figure 3.1. The subcell performance is similar to that of the full cell, however, the efficiency is 1% lower due to small reductions of both J_{SC} and V_{OC}. These losses may indicate device degradation induced either by temperature cycling during capacitance spectroscopy measurements or by aging of the CZTSSe layer since the subcell power curves were measured after the TAS and DLTS measurements. The lower series resistance of the subcell is most likely due to increased front contact area that reduces current spreading resistance, whereas the lower shunt resistance may arise from either localized CZTSSe inhomogeneity, or from effects due to the ultrasonic wire bonding to the front contact. The ideality factor greater than 1 also points to recombination occurring in traps within the depletion width. Even though the subcell is slightly less efficient than the full cell, we do not expect the effects of the subcell preparation to change the overall conclusions in this work.

Thermal admittance spectroscopy of the subcell (Figure 3.2) indicate a very wide distribution of states with an activation energy that corresponds to junction freezeout. The admittance (Y) vs. frequency (ω) values were corrected based on previously published methods [25], [26] using the equation $Y_{corrected} = Y - R_S - i\omega L_S$ where R_S and inductance (L_S) were chosen fitting parameters. First, L_S and R_S were allowed to float, and L_S was chosen by minimizing the error function [26] as well as accurately fitting the increasing capacitance values at high temperature and frequency, which are indicative of inductive effects. Using the resulting best fit $L_S = 1.65 \times 10^{-6}$ Henrys, the function was then fitted

using values spanning from R_S = 5 Ω to R_S = 40 Ω, and choosing R_S = 12 Ω, which minimized overall error in the corrected admittance function. These admittance corrections are described in more detail in Caruso et al. [27] The inductance and resistance corrections do not change the shape of the long, sloping tail of the capacitance at low frequencies, which indicates the gently sloping capacitance step is from a very wide distribution of time constants. Furthermore, the high frequency, low temperature capacitance values converge to the geometric capacitance C_g = 153 pF, indicating this step corresponds to the activation energy of junction freeze out. The calculated subcell C_g = 138 pF (using the dielectric constant $8.24\varepsilon_0$ for E_G=1.1 eV) is close to the experimental result.

The activation energy (E_a) for junction freezeout as measured by TAS is 110 ± 20 meV (Figure 3.3), with a relatively small apparent hole capture cross section (σ_p) of 6×10^{-17} cm^2. This commonly observed state within CZTS(Se) devices [17], [18], [20] has been previously been analyzed as a trap state, although recent work within our research group [27] demonstrates the temperature dependence of this capacitance step (analyzed for a different CZTSe device) instead arises from effects of acceptor freezeout on a non-Ohmic back contact.

Figure 3.3 also presents E_a and the electron capture cross section (σ_n) for the defect measured by DLTS. Figure 3.4 (a) shows the DC voltage and pulse times used in this measurement and presents the expected transient behavior of either a majority (b) or minority (c) trap. The observed transients are decreasing in capacitance. An isothermal transient at 299 K is shown in Figure 3.5. This decreasing capacitance behavior indicates a minority carrier (electron) emission process (Figure 3.4 (c)) is most likely occurring. Since the full interpretation of DLTS relies on knowledge of the junction parameters as

determined by the ionized acceptor concentration, it is important to note the DLTS measurements occur over an entirely different temperature range that is higher than those for which we observe the junction freezeout. Thus, we can assume the ionized acceptor concentration is relatively constant over the range of temperatures comprising the DLTS peak response for the rate windows used herein. Temperature dependent capacitance-voltage measurements (CVT) of the subcell confirm this observation and show an average hole concentration of 1×10^{16} cm^{-3} from 270-335 K. In addition to a different temperature range, the rate windows in the DLTS measurements correspond to a lower frequency range, 10^{-3}-3 Hz, than those used in TAS, 100-10^{6} Hz. This also indicates the processes characterized by TAS and DLTS arise from different activation mechanisms, temperature-dependent series resistance for TAS and emission of a minority carrier from a defect for DLTS.

The activation energy for the carrier emission from the defect measured by DLTS is 590 ± 50 meV from the conduction band edge (E_c) and $\sigma_n = 2 \times 10^{-14}$ cm^2. Unlike the more shallow acceptor state, the small minority carrier σ_n of this deep state indicates it has more coulombic attraction for electrons [28] and a much higher rate of electron capture [29]. This minority carrier trap is a very likely contributor to recombination, especially due to its presence near midgap. The assignment of this response to a minority carrier (electron) capture from and emission to the conduction band arises from a decreasing capacitance transient within DLTS measurements.

Our observations of a decreasing instead of an increasing DLTS signal are atypical of other reported DLTS results of CZTS(Se) [20]. Although voltage-pulsed DLTS is typically considered to measure defects within the p-type absorber layer of an n^+p device,

the capacitance transients may also be affected by high circuit resistance, non-Ohmic contacts, or interface defects. These possibilities further complicate interpreting decreasing transients, which are usually considered to be a result of minority carrier (electron) emission, but may instead be from high series resistances within the device or a Schottky junction between the CZTSSe and Mo. In the following analyses, we examine the possibilities of the observed DLTS signal arising from either a deep minority trap within CZTSSe or from a back contact and conclude the signal is most likely from a deep minority trap within CZTSe.

Conventional and complementary DLTS measurements with equal fill and measurement pulse times demonstrate a decreasing transient signal ($C_{t2} - C_{t1} = \Delta C < 0$) for conventional measurements and an increasing transient ($\Delta C > 0$) for complementary measurements (Figure 3.6). If the measured circuit contains a high enough series resistance in either the solar cell device or the accompanying electrical measurement system, the transient will change polarity [30]. We tested this possibility by adding a 470 Ω resistor in series with the device, which caused the transient to flip from decreasing to increasing in capacitance value over time. If the transient was already flipped from high series resistance before the additional resistance was added, we would expect only a decrease in signal amplitude, not a polarity change. Therefore, we exclude series resistance within the original circuit as the cause of the decreasing signal.

The transient also decreases if majority carriers (hole) are captured by the trap. Increased energy band bending within the depletion region under reversed bias measurement conditions suggest holes are more likely to be emitted rather than captured during the measurement in reversed bias (conventional DLTS – Figure 3.6 (b)). However,

if we still consider hole capture in reversed bias a possibility, we would expect a larger amplitude of ΔC for the complementary signal (i.e., for hole emission) than the conventional signal (i.e., for hole slow capture) [31]. As can be seen in Figure 3.6, we observe the opposite effect. So we also exclude that the decreasing transient arises from majority carrier capture during conventional DLTS measurements.

Theoretical predictions and experiments with standard circuits show a decreasing capacitance transient may also be from a non-Ohmic back contact that has a time constant for the n^+p junction greater than the time constant of the non-Ohmic back contact ($\tau_J > \tau_{BC}$) [32]. If this were the case, the complementary DLTS signal should have the largest amplitude, however, we observe the opposite. The maximum change in capacitance for the complementary DLTS transients (Figure 3.6 (a)) is 3 orders of magnitude smaller for the conventional measurements (Figure 3.6 (b)).

After excluding the series resistance, hole capture, and a non-Ohmic back contact from causing the decreasing transient, we conclude it is most likely due to electron emission in conventional DLTS, and the complementary signal is from the slow capture of electrons. Capture rates depend on carrier concentration available for capture, and this concentration can vary spatially from the depletion region to the quasineutral region (QNR) of the CZTSSe layer. Therefore, the capture rate can spatially vary from "slow" to "fast" capture. Both of these capture rates are faster than emission, which occurs from filled traps within the depletion region during the reversed bias measurement [29]. The change in capacitance is directly proportional to the number of traps responding to the voltage pulse [33], therefore a higher ΔC indicates more traps are involved. Fast capture occurs on a time scale not measurable by our instrumentation, so only the emission and slow capture

processes are observed. All traps emit at relatively the same rate, therefore, the number of traps corresponding to a time constant is expected to be much larger than the very small amount of traps responding at the slow capture rate. Therefore, in addition to the amplitude of the DLTS signals, the comparative rates deducted from the conventional and complementary measurements also point to a minority trap rather than a non-Ohmic back contact. Figure 3.7 shows the normalized ΔC maximum occurs at a lower temperature for the complementary than for the conventional DLTS measurements. This lower temperature maximum indicates a faster transient during complementary measurements. The observed faster transient during the complementary measurements indicates a slow capture process is most likely occurring. For a back contact response, the complementary DLTS measurement is expected to be slower (i.e., maximum ΔC is at a higher temperature) than that of the conventional DLTS measurement [31].

Figure 3.8 shows the energy band diagrams which demonstrate the trap occupation changes with applied bias due to the trap energy relative to the electron quasi-Fermi energy. These diagrams were generated from a SCAPS model in which the CZTSSe material parameters [34] were calculated assuming a 20% CZTS content based on E_g=1.1 eV and linear dependence on material properties with composition. According to the model, the trap only changes occupation within 46 nm of the depletion region (Figure 3.9). Assuming this deep defect is homogenous throughout the bulk, the capacitance response would only account for a small portion of the total defects. This is discussed further in the density of trap states calculation below. The capture cross section of holes was chosen to be 1×10^{-18} cm^{-2} to demonstrate the defect state acting only as a minority trap since that is most consistent with our observations within DLTS transient. In the SCAPS model, the trap

acting as a minority trap with a low hole capture cross section accounts for an 11% relative drop in cell efficiency. If the trap is included, and the hole capture cross section is increased to $1x10^{-15}$ cm^{-2}, the trap behavior and occupation differ dramatically, and the overall cell efficiency drops 35% relative to the model with no trap. Other DLTS observations of near midgap traps acting as acceptors [20] indicate the high likelihood that deep traps may trap holes as well as electrons. Therefore, these traps may act as recombination centers, although DLTS is an inadequate method for observing recombination.

The trap signature reported in this study does not account for entropy effects as well as possible temperature-dependence of the capture cross section. The emission rate equation and subsequent Arrhenius analysis assume a temperature-independent capture cross section as well as the trap energy being equivalent to the Gibbs free energy. In these temperature-dependent emission rate determinations, only the enthalpy within the Gibbs free energy is actually measured [29], and the entropy term for $\Delta G = \Delta H - T\Delta S$ is neglected. A more accurate analysis would use optical excitation to directly account for the entire Gibbs free energy as well as directly measuring the capture cross section as a function of temperature using techniques such a variable pulsed width DLTS [29]. The density of trap states (N_T) within the bandgap was approximated by equation 3.4 [33] (Figure 3.10). C_0 is the steady state capacitance at the applied bias, x_1 is the position in the depletion region at 0 V applied bias where E_T=E_F, x_2 is the position in the depletion region at -0.5 V applied bias where E_T=E_F, and x_d is the depletion width at -0.5 V (Figure 3.9).

$$N_T = 2\frac{\Delta C}{C_0} N_A \left(\frac{x_d^2}{x_1^2 - x_2^2}\right) \tag{3.4}$$

The number of shallow acceptors $N_A = 1 \times 10^{16}$ cm^{-3} was estimated by measuring the free carrier density using CVT and assuming 90% of the shallow acceptors were ionized

(as per the SCAPS simulation). The shallow acceptor ionization did not change significantly between forward and reversed bias since the 110 meV acceptor state lies well below the quasi-Fermi energy for holes. The entire band of states could not be measured due to temperature limits of the cryostat chamber, so the full width half max (FWHM) of 170 meV and a total trap concentration of 1×10^{15} cm^{-3} were determined by Gaussian fit. The N_T calculation is based on the assumption that trap emission occurs over only 46 nm of the sample.

Figure 3.11 shows the overlay of the observed minority trap within the CZTSSe with defect energy predictions [8] of various defects in CZTS and CZTSe. Several deep traps are predicted to have an energy near the observed minority trap energy of 590 meV from the CBE of CZTSSe, shown as 510 meV from the VBE in Figure 3.11 due to the CZTSSe E_g=1.1 eV. Since it is unlikely that a negatively charged defect (i.e., Cu_{Sn}) would capture an electron, the observed minority trap is more likely due to the neutral/positively charged $V_{S,Se}$ or Sn_{Zn} defects. Further studies directly correlating atomic arrangement and composition with defect concentrations are required to conclusively attribute this midgap minority trap to Sn_{Zn} or $V_{S,Se}$ defects.

Conclusions

We observe a near midgap defect behaving as a minority carrier trap in reverse bias DLTS experiments within CZTSSe by measuring a $\eta = 7\%$ solar cell device containing a selenized CZTS nanoparticle ink absorber layer. Using DLTS and CVT analyses, we determine the trap lies 590 meV from the conduction band edge, has an electron-attractive $\sigma_n = 2 \times 10^{-14}$ cm^2, a FWHM of 170 meV, and a total trap concentration of 1×10^{15} cm^{-3}. The decreasing transient observed in the DLTS spectra is attributed to a near midgap

minority trap as opposed to a signal from a non-Ohmic back contact based on comparisons of the conventional and complementary voltage-pulsed DLTS measurements. Admittance spectroscopy measurements also corroborate previous studies of an acceptor state with a junction freeze out activation energy of 110 meV from the valence band edge and a neutral capture cross section of $\sigma_p = 6 \times 10^{-17}$ cm^2.

Evidence for low V_{OC} of CZTSSe devices that is partially from low minority carrier lifetimes has previously been reported [11], and our observation provides direct evidence that deep states within the bandgap of CZTSSe are capable of trapping minority carriers and therefore are likely to act as recombination centers and lower the V_{OC} during operation when the device is in forward bias. When comparing the observed trap energy with theoretical predictions of defects within CZTS and CZTSe, it is proposed the midgap trap may be attributed to either Sn_{Zn} or $V_{S,Se}$. Our former work [35], [36] implicates high Sn activity with deleterious Sn-related defects despite the self-limiting nature of SnS. If the midgap trap is indeed the Sn_{Zn} defect, this could cause further concern for the commonly used high Sn activity during deposition and/or annealing. Another study shows the V_S^{2+} defect is dominant in a large range of chemical potentials within CZTS [37], which may indicate the likelihood of the existence of this defect as well. Further work to correlate this trap with a defect identity and determine if the trap can also act as a recombination center are needed to understand its overall contribution to lowering CZTSSe solar cell efficiencies.

Acknowledgements

The research discussed herein was supported in whole by the U.S. Department of Energy, Office of Basic Energy Sciences, Division of Materials Sciences and Engineering under Award DE-SC0001630.

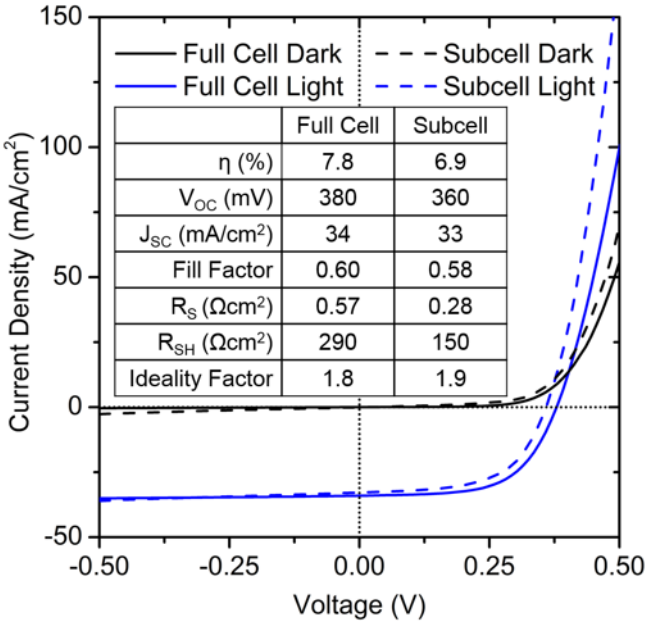

	Full Cell	Subcell
η (%)	7.8	6.9
V_{OC} (mV)	380	360
J_{SC} (mA/cm²)	34	33
Fill Factor	0.60	0.58
R_S (Ωcm²)	0.57	0.28
R_{SH} (Ωcm²)	290	150
Ideality Factor	1.8	1.9

Figure 3.1. Current density-voltage curves. Both the full cell (solid line) and subcell (dashed line) were measured in the dark (black line) and under AM 1.5 illumination (blue line). Front contacts cover 20% of the subcell, therefore, calculations are based on a 1.5 mm^2 area. The efficiency (η), open-circuit voltage (V_{OC}), short-circuit current density (J_{SC}), fill factor, series resistance (R_S), and shunt resistance (R_{SH}) are presented for comparison of both cells.

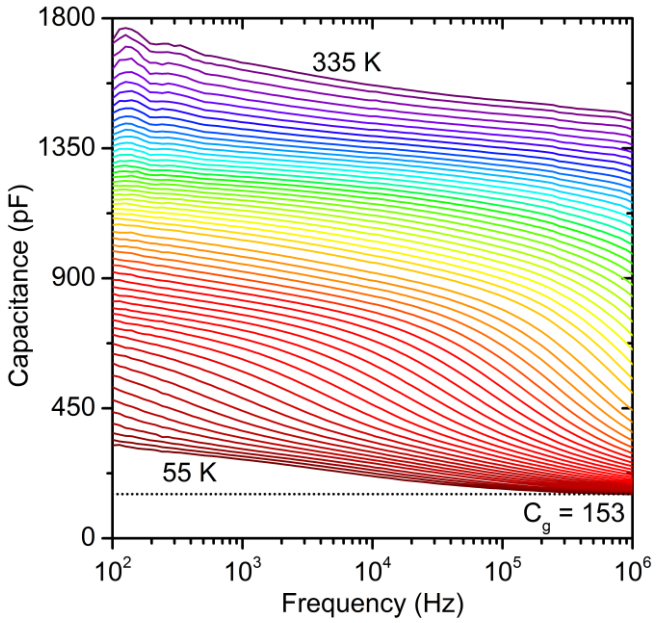

Figure 3.2. Temperature admittance spectroscopy data. Capacitance measurements from 335 K (purple) to 55 K (red) at 5 K increments were corrected for series resistance and inductance effects. The junction capacitance step converges to the geometric capacitance (C_g) at low temperatures.

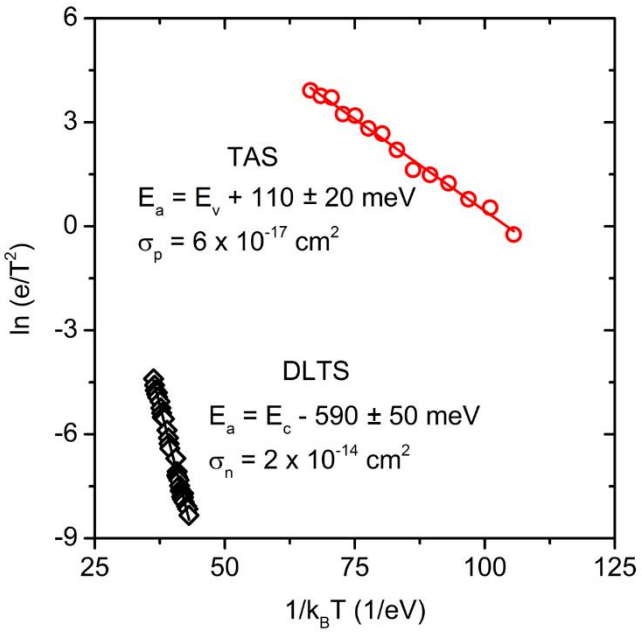

Figure 3.3. Arrhenius plot with TAS and DLTS trap signatures. The Arrhenius plot with the apparent activation energies (E_a) relative to either the valence or conduction band edge (E_V, E_C) and either apparent hole or electron capture cross sections (σ_p, σ_n) calculated from either TAS (red circles) or DLTS (black diamonds) measurements.

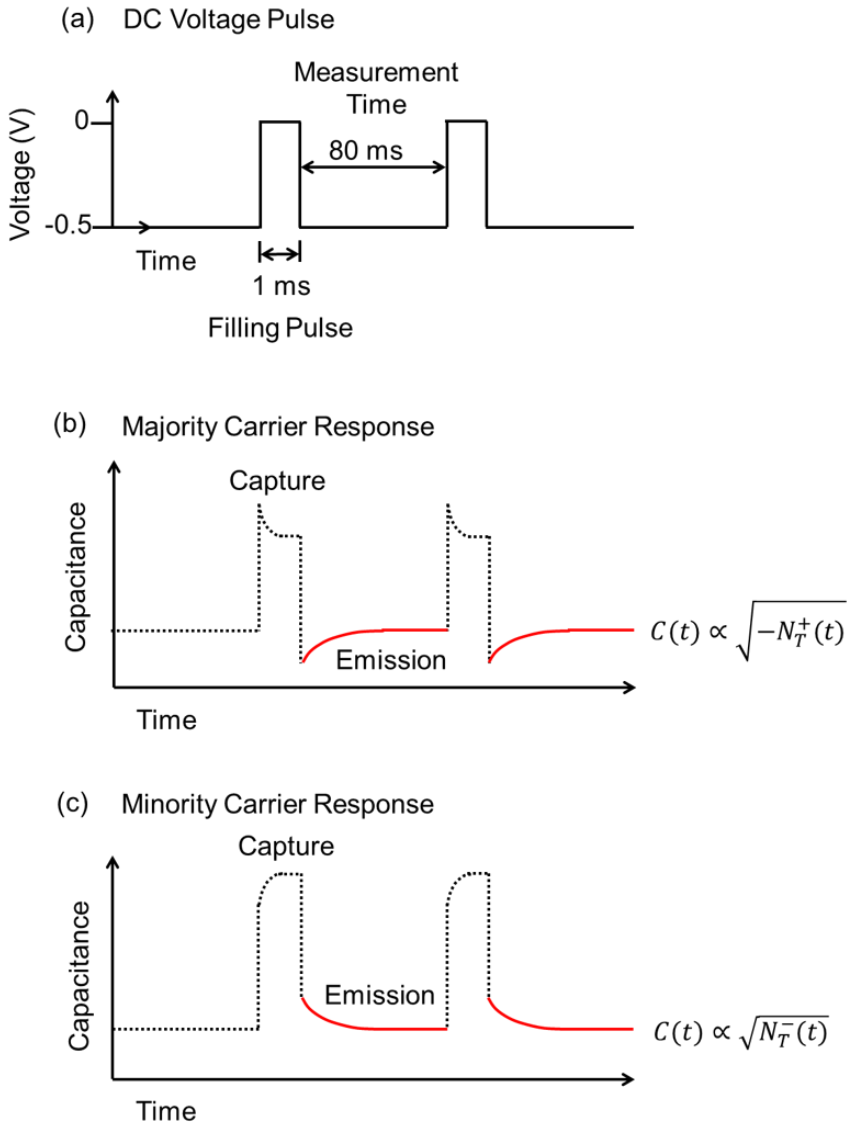

Figure 3.4. Voltage pulses and expected capacitance transients for majority and minority carrier emission. (a) DC voltage pulsing. Expected capacitance transient response due to change in voltage for either (b) majority or (c) minority capture and emission. A large and fast response is expected for the depletion width decrease when changing from -0.5 V to 0 V, and a slower transient is expected due to deep trap occupation response. During the filling pulse, the free carrier is captured from the relevant band edge (Figure 2.2). During the measurement time, that same carrier is emitted back to the relevant band edge. An example of an expected capacitance response based on the change in N_{SCR} (equation 2.5) is shown in solid red for (b) and (c) based on the proportionality to the right of the transient. The dotted portion of the capacitance curves represent the expected, but not measured, response. Figure is not to scale.

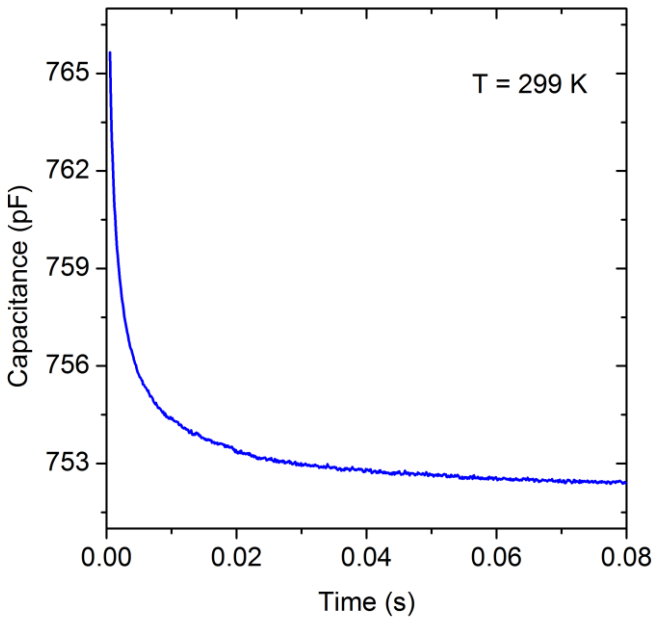

Figure 3.5. Decreasing capacitance transient observed at 299 K. Measurement conditions are shown in Figure 3.4 (a).

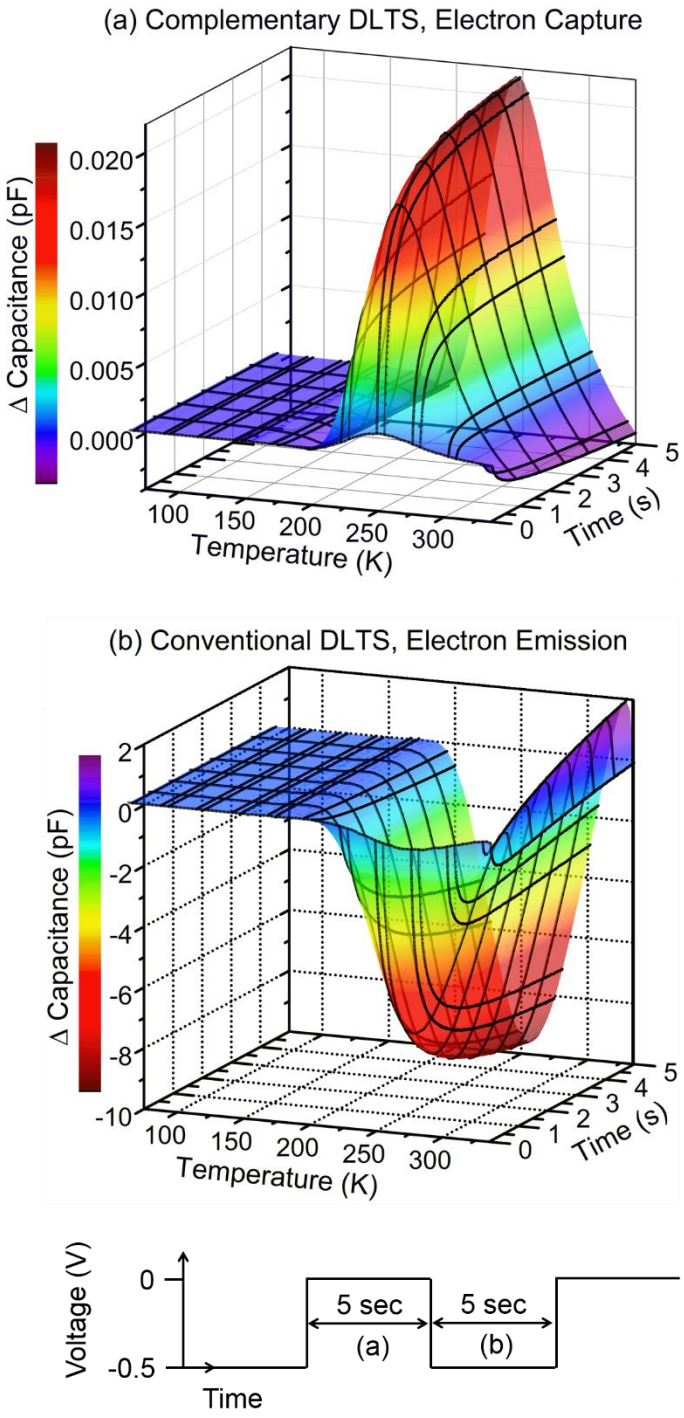

Figure 3.6. Conventional and complementary DLTS measurements. The capacitance transients measured from two separate sets of DLTS measurements from 85 K to 335 K during either (a) no bias for complementary DLTS or (b) -0.5V reversed bias for conventional DLTS. Both sets of experiments had equal duration excitation pulse and measurement times of 5 seconds.

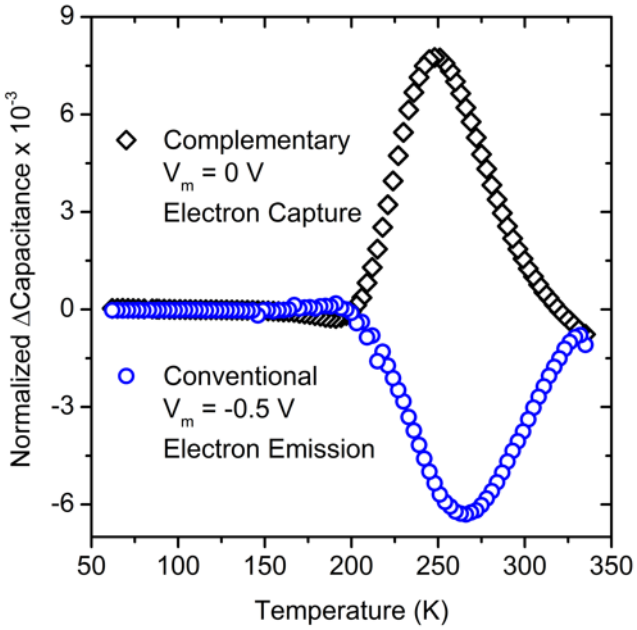

Figure 3.7. Conventional and complementary DLTS measurements for 100 ms rate window. The change in capacitance (C) versus the temperature for a 100 ms rate window from the conventional (blue circles) and complementary (black diamond) DLTS signals. Normalized ΔCapacitance = [C(150 ms)–C(50 ms)]/C(5s). The maximum amplitude of the normalized ΔCapacitance occurs at a higher temperature for the conventional DLTS measurement, therefore, the emission rate is assumed to be slower for this process than for the electron capture.

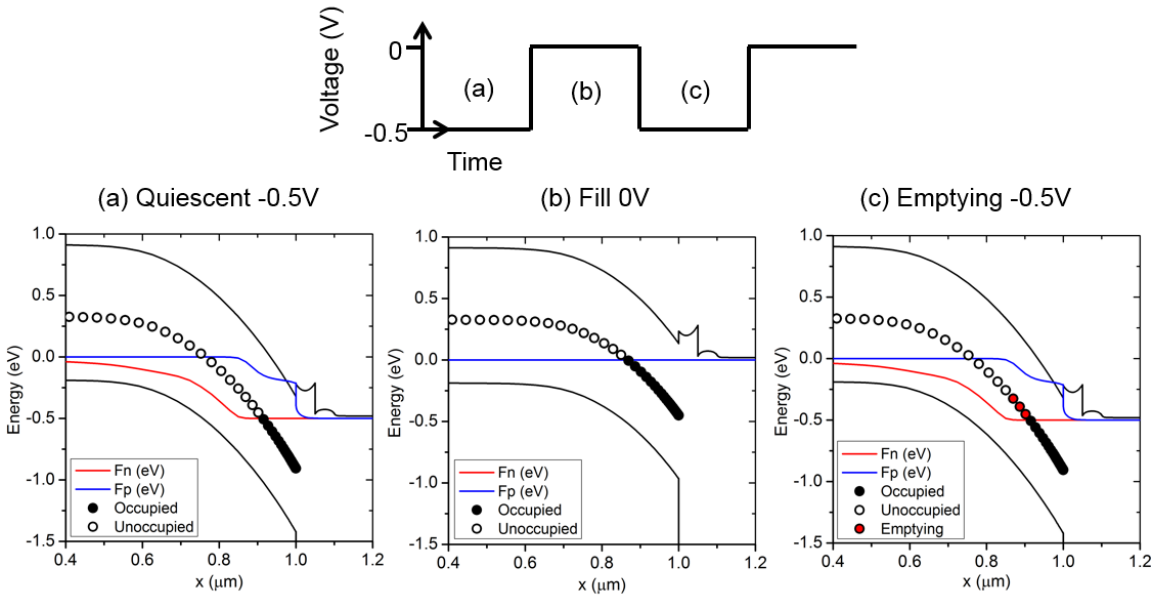

Figure 3.8. SCAPS band diagrams. These diagrams show the minority trap filling and emptying as a result for forward and reversed bias. If electrons occupy the trap, the trap lies below the quasi-Fermi level for electrons (E_{Fn}).

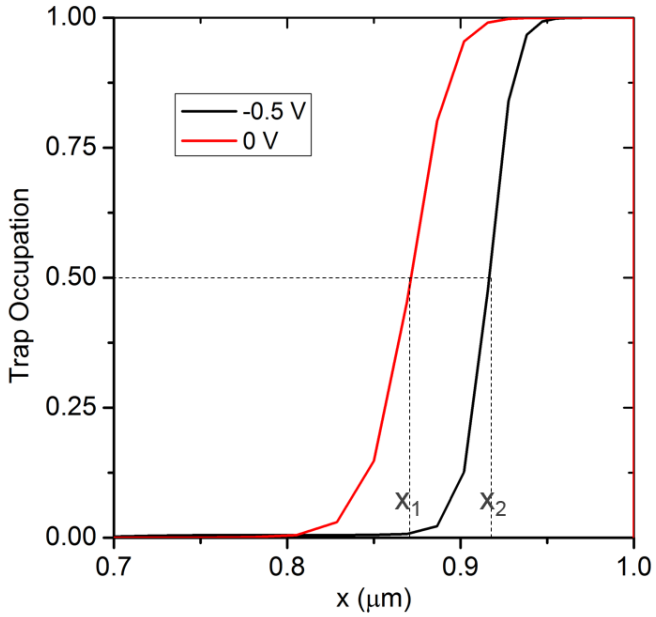

Figure 3.9. Minority trap occupation within CZTSSe. The positions x_1 and x_2 depict where the trap energy level crosses the quasi-Fermi level for electrons either in reversed bias (black) or no applied bias (red) in the dark.

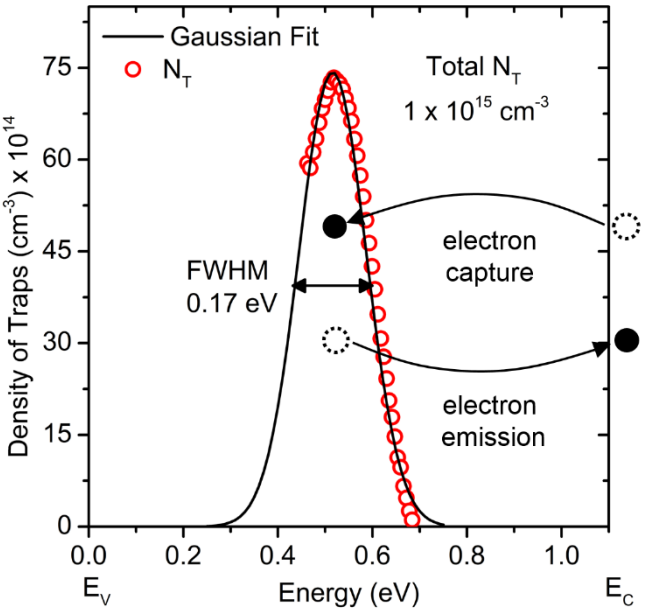

Figure 3.10. Density of states of deep minority carrier trap. The density of the deep defect state (N_T) measured by DLTS is calculated from the change in capacitance vs. temperature from DLTS and CVT measurements. Electron capture and emission are illustrated as processes that interact with the deep state and the conduction band edge E_C = 1.1 eV. The reported full width half max (FWHM) and total N_T are determined from the Gaussian fit.

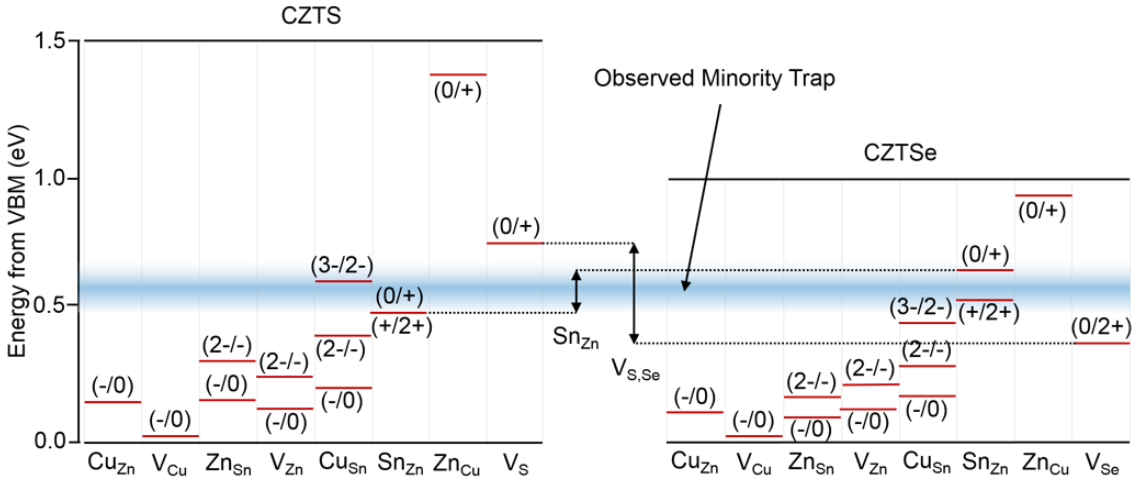

Figure 3.11. Observed minority trap overlaid on calculated defect energies. The blue band represents the observed apparent trap energy and DOS width and is compared to various vacancy and antisite defects in CZTS and CZTSe [8]. This trap falls within the theoretical limits of both the positively charged Sn_{Zn} and $V_{S,Se}$ defect energies as defined by the predictions for CZTS and CZTSe.

References

[1] D. B. Mitzi et al., “Prospects and performance limitations for Cu-Zn-Sn-S-Se photovoltaic technology,” *Philos. Trans. A. Math. Phys. Eng. Sci.*, vol. 371, no. 1996, p. 20110432, Aug. 2013.

[2] W. Wang et al., “Device characteristics of CZTSSe thin-film solar cells with 12.6% efficiency,” *Adv. Energy Mater.*, vol. 4, no. 7, May 2014.

[3] S. Krum et al., “First solar builds the highest efficiency thin film PV cell on record,” 2014. [Online]. Available: http://investor.firstsolar.com/releasedetail.cfm?ReleaseID=864426.

[4] P. Jackson et al., “Compositional investigation of potassium doped Cu(In,Ga)Se2 solar cells with efficiencies up to 20.8%,” *Phys. Status Solidi - Rapid Res. Lett.*, vol. 8, no. 3, pp. 219–222, Mar. 2014.

[5] D. W. Miller et al., “Electronically active defects in the Cu2ZnSn(Se,S)4 alloys as revealed by transient photocapacitance spectroscopy,” *Appl. Phys. Lett.*, vol. 101, no. 14, p. 142106, 2012.

[6] T. Gokmen et al., “Minority carrier diffusion length extraction in Cu2ZnSn(Se,S)4 solar cells,” *J. Appl. Phys.*, vol. 114, no. 11, p. 114511, 2013.

[7] U. Rau and J. H. Werner, “Radiative efficiency limits of solar cells with lateral band-gap fluctuations,” *Appl. Phys. Lett.*, vol. 84, no. 19, p. 3735, 2004.

[8] S. Chen et al., “Classification of lattice defects in the kesterite Cu2ZnSnS4 and Cu2ZnSnSe4 earth-abundant solar cell absorbers,” *Adv. Mater.*, vol. 25, no. 11, pp. 1522–39, Mar. 2013.

[9] U. Rau et al., “Electronic loss mechanisms in chalcopyrite based heterojunction solar cells,” *Thin Solid Films*, vol. 361–362, pp. 298–302, Feb. 2000.

[10] U. Rau et al., “Electrical characterization of Cu(In,Ga)Se2 thin-film solar cells and the role of defects for the device performance,” vol. 67, pp. 137–143, 2001.

[11] I. L. Repins et al., “Indications of short minority-carrier lifetime in kesterite solar cells,” *J. Appl. Phys.*, vol. 114, no. 8, p. 084507, 2013.

[12] O. Gunawan et al., “Loss mechanisms in hydrazine-processed Cu[sub 2]ZnSn(Se,S)[sub 4] solar cells,” *Appl. Phys. Lett.*, vol. 97, no. 23, p. 233506, 2010.

[13] S. Das et al., “Defect levels in Cu2ZnSn(SxSe1−x)4 solar cells probed by current-mode deep level transient spectroscopy,” *Appl. Phys. Lett.*, vol. 104, no. 19, p. 192106, May 2014.

[14] J. P. Leitão et al., “Photoluminescence and electrical study of fluctuating potentials in Cu2ZnSnS4-based thin films,” *Phys. Rev. B*, vol. 84, no. 2, p. 024120, Jul. 2011.

[15] A. Nagaoka et al., “Growth and characterization of Cu2ZnSnS4 single crystals,” *Phys. Status Solidi*, vol. 210, no. 7, pp. 1328–1331, Jul. 2013.

[16] M. Grossberg et al., “The role of structural properties on deep defect states in Cu2ZnSnS4 studied by photoluminescence spectroscopy,” *Appl. Phys. Lett.*, vol. 101, no. 10, p. 102102, 2012.

[17] D. A. R. Barkhouse et al., “Device characteristics of a 10.1% hydrazine-processed Cu2ZnSn(Se,S)4 solar cell,” *Prog. Photovoltaics Res. Appl.*, vol. 20, no. 1, pp. 6–11, Jan. 2012.

[18] O. Gunawan et al., “Electronic properties of the Cu2ZnSn(Se,S)4 absorber layer in solar cells as revealed by admittance spectroscopy and related methods,” *Appl. Phys. Lett.*, vol. 100, no. 25, p. 253905, 2012.

[19] H.-S. Duan et al., “The role of sulfur in solution-processed Cu2ZnSn(S,Se)4 and its effect on defect properties,” *Adv. Funct. Mater.*, vol. 23, no. 11, pp. 1466–1471, Mar. 2013.

[20] J. V. Li et al., “Effects of sodium incorporation in Co-evaporated Cu2ZnSnSe4 thin-film solar cells,” *Appl. Phys. Lett.*, vol. 102, no. 16, p. 163905, 2013.

[21] E. Kask et al., “Defect studies in Cu2ZnSnSe4 and Cu2ZnSn(Se0.75S0.25)4 by admittance and photoluminescence spectroscopy,” *Mater. Sci. Semicond. Process.*, vol. 16, no. 3, pp. 992–996, Jun. 2013.

[22] T. Gershon et al., “Photoluminescence characterization of a high-efficiency Cu2ZnSnS4 device,” *J. Appl. Phys.*, vol. 114, no. 15, p. 154905, 2013.

[23] Q. Guo et al., “Enhancing the performance of CZTSSe solar cells with Ge alloying,” *Sol. Energy Mater. Sol. Cells*, vol. 105, pp. 132–136, Oct. 2012.

[24] C. K. Miskin et al., “9.0% efficient Cu2ZnSn(S,Se)4 solar cells from selenized nanoparticle inks,” *Prog. Photovoltaics Res. Appl.*, vol. 57, Apr. 2014.

[25] J. H. Scofield, “Effects of series resistance and inductance on solar cell admittance measurements,” *Sol. Energy Mater. Sol. Cells*, vol. 37, no. 2, pp. 217–233, May 1995.

[26] J. Lauwaert et al., “A simple correction method for series resistance and inductance on solar cell admittance spectroscopy,” *Sol. Energy Mater. Sol. Cells*, vol. 94, no. 6, pp. 966–970, Jun. 2010.

[27] A. E. Caruso et al., “Temperature dependence of equivalent circuit parameters used to analyze admittance spectroscopy and application to CZTSe devices,” in *Photovoltaic Specialist Conference (PVSC), 2014 IEEE 40th*, 2014, pp. 733–736.

[28] M. Gloeckler et al., “Numerical modeling of CIGS and CdTe solar cells: Setting the baseline,” in *World Conference on Photovoltaic Energy Conversion*, 2003, p. Vol. 1 491–494.

[29] P. Blood and J. W. Orton, *The Electrical Characterizatioin of Semiconductors: Majority Carriers and Electron States*. San Diego, CA: Academic Press, 1992.

[30] D. K. Schroder, “Parallel or Series Connection?” in *Semiconductor Material and Device Characterization*, 3rd ed., Wiley-IEEE Press, 2006.

[31] J. Lauwaert et al., “About RC-like contacts in deep level transient spectroscopy and Cu(In,Ga)Se2 solar cells,” *Prog. Photovoltaics Res. Appl.*, vol. 20, no. 5, pp. 588–594, Aug. 2012.

[32] J. Lauwaert et al., “Assignment of capacitance spectroscopy signals of CIGS solar cells to effects of non-ohmic contacts,” *Sol. Energy Mater. Sol. Cells*, vol. 112, pp. 78–83, May 2013.

[33] J. Cohen and D. Lang, “Calculation of the dynamic response of Schottky barriers with a continuous distribution of gap states,” *Phys. Rev. B*, vol. 25, no. 8, pp. 5321–5350, Apr. 1982.

[34] C. Persson, “Electronic and optical properties of Cu2ZnSnS4 and Cu2ZnSnSe4,” *J. Appl. Phys.*, vol. 107, no. 5, p. 053710, 2010.

[35] E. A. Lund et al., “Investigation of combinatorial coevaporated thin film Cu2ZnSnS4 (II): Beneficial cation arrangement in Cu-rich growth,” *J. Appl. Phys.*, vol. 115, no. 17, p. 173503, May 2014.

[36] H. Du et al., “Investigation of combinatorial coevaporated thin film Cu2ZnSnS4. I. Temperature effect, crystalline phases, morphology, and photoluminescence,” *J. Appl. Phys.*, vol. 115, no. 17, p. 173502, May 2014.

[37] V. Kosyak et al., “Model of native point defect equilibrium in Cu2ZnSnS4 and application to one-zone annealing,” *J. Appl. Phys.*, vol. 114, no. 12, p. 124501, 2013.

CHAPTER 4

INVESTIGATION OF COMBINATORIAL COEVAPORATED THIN FILM CU_2ZNSNS_4 (II): BENEFICIAL CATION ARRANGEMENT IN CU-RICH GROWTH

Reprinted with permission from Lund, E. A. and Du, H. and Hlaing OO, W. M. and Teeter, G. and Scarpulla, M. A.; Investigation of combinatorial coevaporated thin film Cu_2ZnSnS_4 (II): Beneficial cation arrangement in Cu-rich growth, Journal of Applied Physics, 115, 173503 (2014), DOI:http://dx.doi.org/10.1063/1.4871665.

JOURNAL OF APPLIED PHYSICS **115**, 173503 (2014)

Investigation of combinatorial coevaporated thin film Cu_2ZnSnS_4 (II): Beneficial cation arrangement in Cu-rich growth

E. A. Lund,[1] H. Du,[2,a)] W. M. Hlaing OO,[3] G. Teeter,[4] and M. A. Scarpulla[1,3,5,b)]
[1]*Department of Chemical Engineering, University of Utah, 50 S. Central Campus Dr. Rm 3290, Salt Lake City, Utah 84112, USA*
[2]*Sion Power Corporation, 2900 E Elvira Rd., Tucson, Arizona 86756, USA*
[3]*Department of Materials Science and Engineering, University of Utah, 122 S. Central Campus Dr. Rm 304, Salt Lake City, Utah 84112, USA*
[4]*National Renewable Energy Laboratory, 15013 Denver West Parkway, MS3218, Golden, Colorado 80401, USA*
[5]*Department of Electrical and Computer Engineering, University of Utah, 50 S. Central Campus Dr. Rm 3280, Salt Lake City, Utah 84112, USA*

(Received 7 November 2013; accepted 6 April 2014; published online 2 May 2014)

$Cu_2ZnSn(S,Se)_4$ (CZTSSe) is an earth-abundant semiconductor with potential for economical photovoltaic power generation at terawatt scales. In this work, we use Raman scattering to investigate phase coexistence in combinatorial CZTS thin films grown at 325 or 470 °C. The surface of the samples grown at 325 °C is rough except for a prominent specularly reflective band near and along the ZnS-Cu_2SnS_3 (CTS) tie line in the Cu-Zn-Sn-S quaternary phase diagram. All structurally incoherent secondary phases (SnS_2, CuS) exist only as surface phases or are embedded as separate grains, whereas the structurally coherent secondary phase CTS coexists with CZTS in the dense underlying film. In films grown at 325 °C, which are kinetically trapped by the low growth temperature, a change is observed in Cu and Sn site occupancy, evidenced by the shift from cubic-CTS in the Cu-rich region (Cu/Sn > 2) to more tetragonal-CTS in the Sn-rich region (Cu/Sn < 2). For CZTS samples grown at 470 °C, CTS is not observed and regions grown under excess Sn flux are more disordered than Cu-rich regions evidenced by broader CZTS A mode peaks. Therefore, increasing Sn chemical potential results in more CZTS lattice disorder, suggesting, with other evidence, the formation of Sn antisite defects. In contrast, the CZTS A mode breadth is insensitive to Zn richness suggesting that excess Zn does not induce significant disorder within the CZTS lattice. We postulate that initially growing CZTS films Cu-rich (Cu/Sn > 2) results in higher cation ordering meaning fewer antisite defects. © *2014 AIP Publishing LLC*.
[http://dx.doi.org/10.1063/1.4871665]

I. INTRODUCTION

$Cu_2ZnSn(S,Se)_4$ (CZTSSe), a semiconductor used as an absorber layer in thin film solar cells, poses an alternative to $Cu(In,Ga)Se_2$ (CIGSe) due to the constituent elements' relatively low costs and large industrial availability. Recent thin film solar cell device efficiencies of 12.6% (Ref. 1) for mixed sulfoselenide (CZTSSe) absorbers and 8.4% (Refs. 2 and 3) for the pure sulfide (CZTS) demonstrate the viability of this material for use in practical thin film technologies. However, the compositional region of thermodynamic stability for the pure CZTS phase is quite small on the bulk pseudo-ternary phase diagram at temperatures relevant for thin film synthesis,[4,5] which indicates the formation of secondary phases such as ZnS, Cu_xSnS_{x+1}, Sn_xS_y, and Cu_xS is probable with variations in stoichiometry.

The defects and secondary phases that result from compositional variation both positively and negatively affect CZTSSe devices. $Cu_{2-x}S(Se)$ phases in the final film may cause shunting due to both the high conductivity and contact with front and back CZTS(Se) interfaces. Nevertheless, it is also used as a fluxing agent to promote lateral grain growth during the initial stage of CZTSe (Ref. 6) coevaporation. ZnS phase separation from CZTS at the back interface lowers the open circuit voltage (V_{OC}) of a CZTS device[7] and ZnSe within the space-charge region of a CZTSe film blocks charge collection due to band structure misalignment with CZTSe.[8] Even though ZnS(Se) phase precipitation lowers CZTS(Se) device performance,[9,10] a final Zn-rich, Cu-poor film composition yields higher device V_{OC} and agrees with the prediction[11] that the defect complex $[V_{Cu}^{-} + Zn_{Cu}^{+}]^0$ formed in this compositional regime may maximize CZTS(Se) device performance. Secondary phases including ZnS and Cu_2SnS_3 (CTS) that have similar crystalline structures to CZTS may also passivate grain boundaries[12] by reducing strain and lowering recombination velocities at the grain interfaces. Although CTS may play a positive role in grain boundary passivation, its lower bandgap (0.8–0.9 eV for CTS and 0.4 eV for CTSe)[13] may decrease V_{OC} for CZTS devices and, therefore, reduce overall solar cell efficiency.

The current record efficiency kesterite device was made by a non-vacuum hydrazine processing method, whereas all record-efficiency CIGSe devices over the last 20 years[6] have

[a)]This work was performed while H. Du was at National Renewable Energy Laboratory, 15013 Denver West Parkway, MS3218, Golden, Colorado 80401, USA.
[b)]Author to whom correspondence should be addressed. Electronic mail: scarpulla@eng.utah.edu.

been deposited by coevaporation. An advantage of coevaporative growth is the tunability of composition through the film thickness, which can control the bandgap and phases present as well as maintain high overpressure of volatile species during long growth runs at high temperature. Nevertheless, coevaporative growth of CZTSSe is encumbered by the high substrate temperatures necessary for quality grain growth, which causes SnS loss and CZTS decomposition into binary $Cu_{2-x}S$ and ZnS.[14–16] Despite these challenges, a 9.15% efficient CZTSe device has been made using a 2-stage coevaporation process, which incorporates a transition from Cu- to Zn-rich growth.[6] Kaune *et al.*[17] demonstrate the conversion of $Cu_{2-x}Se$, SnSe, and ZnSe directly into CZTSe during the 2-stage coevaporation of CZTSe; however, CZTS(Se) grown at low temperature (<400 °C) develops an intermediate CTS(Se) phase, which requires higher temperature processing to convert to CZTS(Se).[18,19] These observations emphasize that both temperature and composition affect the phases which coexist with CZTS during growth.

For low-quality or small-grained films, the CTS and ZnS secondary phases are difficult to distinguish from CZTS by x-ray diffraction (XRD), which further complicates the development and evaluation of phase-pure CZTS films. Raman spectroscopy has been shown to resolve some secondary phases from CZTS, and both lateral and depth resolution at the scale of grains have been achieved.[20] Raman studies on CZTS published to date examined samples intended to be compositionally homogeneous across the films.

In this work, we examine compositionally graded, or "combinatorial," CZTS thin films to isolate the effects of composition on phase formation during growth. The samples are similar to those studied and characterized by Du *et al.*[21] in part 1 of this 2-part study. These unique films deposited by coevaporation of elemental Cu, Zn, Sn, and S sources in a molecular beam epitaxy system cover a wide stoichiometric range with all other variables constant.

For films deposited at 325 °C, there is a clearly visible specular band corresponding to the ZnS-CZTS-Cu_2SnS_3 tie line, which follows the ratio Cu/Sn ∼ 2 in CZTS pseudo-ternary phase diagrams. The surface roughness on either side of the specular band is due to Cu_xS and Sn_xS_y surface phases. Both tetragonal- and cubic-Cu_2SnS_3 ($I\bar{4}2m$ tet- and $F\bar{4}3m$ cub-CTS) coexist with CZTS, even in Zn-rich regions where only ZnS and CZTS are expected. The CTS shifts from more cub- to more tet-CTS as the composition shifts from Cu-rich (Cu/Sn > 2) to Sn-rich (Cu/Sn < 2) and from Zn-poor (Cu/Zn > 2) to Zn-rich (Cu/Zn < 2). The change in CTS phase indicates that composition influences the Cu and Sn cation ordering in CTS.

As expected, films grown at 470 °C do not contain CTS and final CZTS crystalline quality is improved with increased growth temperature. The change in Cu and Sn cation ordering within the similarly zinc-blende based CTS phases observed at low growth temperature and the marked increase in CZTS crystalline quality when the high temperature growth sample shifts from Sn-rich to Cu-rich indicates Cu-rich growth may lead to less disorder within CZTS. Our findings are consistent with part 1 of this study, which found dramatically higher photoluminescence (PL) yields in Cu-rich versus Sn-rich regions of the films. The deleterious effects of excess Sn are attributed to native Sn-related defects, which we postulate can be minimized by initial Cu-rich growth. A larger Zn fraction in the sample has relatively little effect on the overall crystalline quality as analyzed by Raman spectroscopy.

II. MATERIALS AND METHODS

A. Deposition of combinatorial thin films

The CZTS films were deposited in a high vacuum physical vapor deposition system with either 325 or 476 °C substrate heating. Cu, Zn, and Sn were evaporated from effusion cells, and S was supplied through a valved cracker. The deposition chamber was equipped with translatable apertures that partially block the metal flux from each source to introduce a graded distribution of the specific element. No aperture was used for the sulfur source. The metal sources with combinatorial apertures were oriented 120° with respect to each other, resulting in films with metal spatial composition gradients. The *ex situ* calibration of the growth rate for this experiment was about 2.1 Å/s, and the films were approximately 0.75–1.5 μm thick. Substrates were molybdenum-coated soda lime glass (SLG/Mo) with dimensions 15 mm × 20 mm. This study encompasses 3 "low temperature" films grown at 325 °C and one "high temperature" film grown at 470 °C with excess fluxes of S and Sn to prevent CZTS decomposition. The three low temperature films have composition ranges containing a point corresponding to stoichiometric CZTS, a film with significant Zn excess, and another film with no Zn. The high temperature film had a small excess of Sn flux during cooling to prevent decomposition and formation of Cu_xS. A detailed description of the deposition is provided in part 1.[21]

B. Raman spectroscopy, scanning electron microscopy (SEM), and X-ray fluorescence (XRF)

Raman spectroscopy was done using an excitation wavelength of 488 nm in a WiTec AlfaSNOM confocal microscope system in the backscattering configuration. The instrument was equipped with a 10× magnification and 0.25 numerical aperture lens. The laser-illuminated spot on the samples was 20 μm in diameter, and the data were collected from a 2 μm area within that spot using the pinhole of the confocal system after carefully focusing each point at the surface of the film. A long-pass filter was employed, which has a cut-on wavelength of 492.8 nm. The absolute wavenumber calibration of the system was measured with a crystalline Si wafer before collection of each data set, and the laser power was adjusted sufficiently low to ensure that the CZTS peaks were not shifted by thermal effects. The metal and sulfur atomic percentages reported for each Raman analysis spot were determined using energy dispersive x-ray spectroscopy (EDS) in an FEI Quanta SEM at an accelerating voltage of 15 keV. The sampling area was 20 μm × 20 μm for the EDS analysis to avoid complications from local fluctuations as the Raman and EDS were measured in different instruments. The Raman signals changed

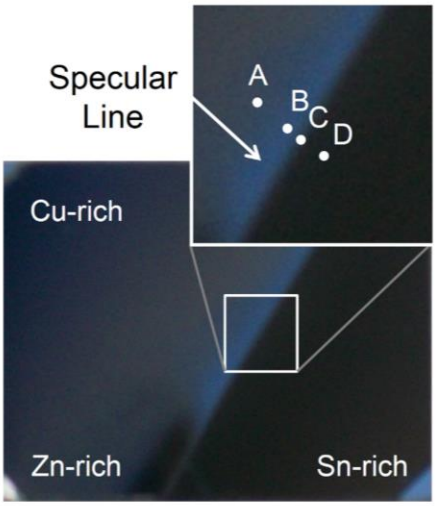

FIG. 1. Diffuse light image of a typical combi-CZTS sample grown at 325 °C showing the specular band. The corners of the sample closest to the respective metal effusion cell sources are labeled Cu-, Sn-, and Zn-rich. Analysis spot C lies just at the transition between specular and rough morphologies. Spots A-D all lie along a line perpendicular to the specular band (spacing not to scale). Spot B lies in the shiniest part of the specular band, 200 μm towards the Cu-rich region from the specular/rough edge. Spot A is 700 μm from spot C into the Cu-rich region. Spot D is 250 μm from point C but in the Sn-rich region.

sufficiently slowly with distance across the sample that the data presented for each analysis spot are representative of the area sampled by EDS. XRF measurements were also made of Cu, Zn, and Sn on a regular grid over the entire sample area with a mm-sized probe and were used to create the compositional contour plots.

III. RESULTS AND DISCUSSION

A. Low temperature films deposited at 325 °C

1. Surface morphology

The compositionally graded CZTS thin films deposited at 325 °C vary in surface morphology due to composition-dependent variation of secondary phases. The diffuse light image of a typical sample (Fig. 1) shows the most notable feature of these low temperature samples: a distinct specularly reflective band running diagonally across the film. Compositional contour maps (Fig. 2) of another combi-CZTS sample deposited under similar conditions demonstrate that the [Cu]/[Sn] ratio correlates with surface roughness on both sides of the specular band. As discussed in part 1,[21] the specular band appears in the region of the sample containing only CZTS and structurally coherent secondary phases including ZnS and cub- and tet-CTS.

The morphological transition from a rough surface to the smooth specular band is gradual on the Cu-rich side, whereas it is abrupt on the Sn-rich side. On the Cu-rich side, Cu_xS is present predominantly as ~1 μm crystals of CuS on top of the CZTS film with the areal density gradually decreasing towards and into the specular region. Part 1[21] shows that the Cu-rich region of a similar sample contains both surface and embedded CuS and Cu_2S crystals in a densely packed film. On the Sn-rich side of the film, the morphology abruptly changes from a very smooth, dense film with no surface phases on the specular band to a thin, porous film of densely packed CZTS with flake-like SnS_2 on top.[21] Part 1 presents XRD and SEM data with the discussion of the correlation of rough or smooth surface morphology to the secondary phases that are structurally incoherent (SnS_2 and Cu_xS) or structurally coherent (CTS and ZnS).

2. Composition

EDS compositional mapping of two low temperature samples, a "regular" and a "Zn-rich" sample, shows a wide variation in Zn composition (Fig. 3) along the specular band. The "Zn-rich" sample was deposited under the same conditions as the "regular" sample, except with a higher Zn flux. In the specular band, the Zn/(Cu + Sn + Zn) fraction spans Zn-poor (0.18) to Zn-rich (0.68) along the ZnS-Cu_2ZnSnS_4-Cu_2SnS_3 tie line of the CZTS quaternary phase diagram, indicating that compositions along this tie line result in lower densities of surface phases. Similar XRF compositional studies also agree with this finding.[21]

The phases detected by Raman spectroscopy in thin films grown at 325 °C include CZTS, SnS_2, Cu_2S, CuS, tet- and cub-CTS, and orthorhombic-Cu_3SnS_4. However, these phases are not all contained exclusively on either the CuS-ZnS-SnS pseudo-ternary phase diagram shown in Fig. 3

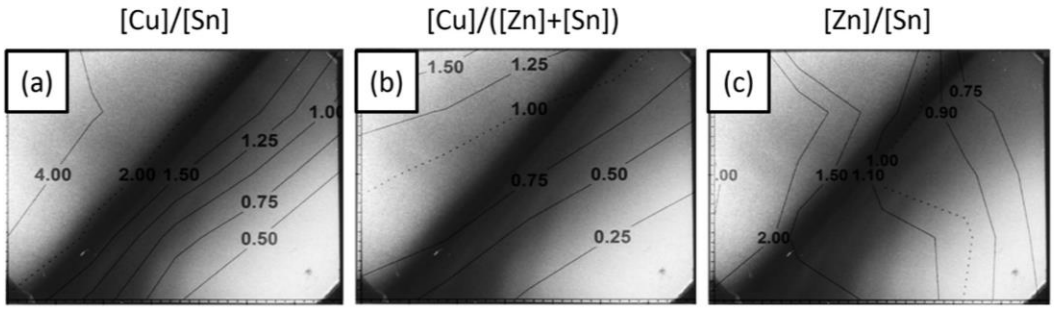

FIG. 2. Diffuse light reflection images overlaid with a compositional contour map determined by XRF. Image (a) shows that there is a clear correlation between the specular region and compositions defined by [Cu]/[Sn] ≅ 2.

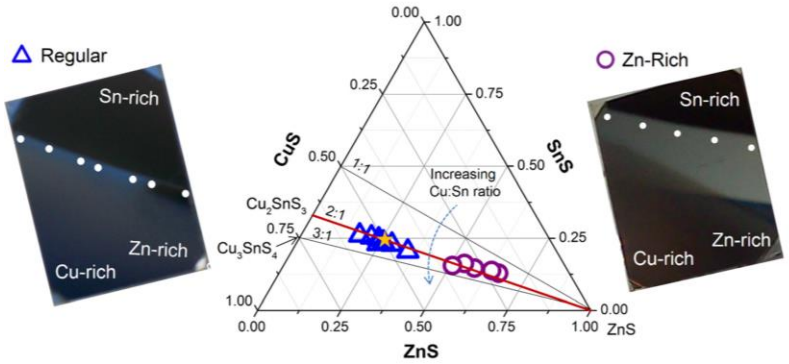

FIG. 3. Optical images of typical and Zn-rich combinatorial films are shown to the left and right of the pseudo-ternary diagram (respectively). The white spots on the sample correspond to the compositional points plotted on the diagram as blue triangles (regular) and purple circles (Zn-rich). The yellow star marks the metals composition of stoichiometric CZTS. Lines depicting [Cu]/[Sn] = 1:1, 2:1, and 3:1 are labeled as well to show that an increasing ratio moves in an arc on the diagram. The [Cu]/[Sn] = 2:1 isopleth is the CTS-CZTS-ZnS tie line and is shown in red.

or the Cu_2S-ZnS-SnS_2 pseudo-ternary diagram investigated by Olekseyuk *et al.*[4] The latter pseudo-ternary phase diagram is the one typically referenced when discussing CZTS phase equilibria, and it is from samples reacted at 1170–1420 K in a sealed glass ampoule followed by annealing at 670 K. Figure 4 displays these two possible pseudo-ternary diagrams as striped yellow and solid purple planes within the quaternary Cu-Zn-Sn-S phase diagram. They intersect along the ZnS-Cu_2ZnSnS_4-Cu_2SnS_3 tie line. The CuS-ZnS-SnS plane maintains a constant metal:S ratio, while the Cu_2S-ZnS-SnS_2 plane maintains the formal oxidation states of the metals in the kesterite structure.

For deposition conditions such as the non-equilibrium thin film route discussed herein, the phase compositions that occur do not fall on exclusively one of these planes due to combined effects of temperature, growth rate, and sulfur activity during deposition. From the phases we observe, for sufficiently high S chemical activity (recall a cracked sulfur flux is used), the ZnS-SnS_2-Cu_2SnS_3 and ZnS-CuS-Cu_2SnS_3 half planes predict the dominant observed phases for Sn- and Cu-rich compositions, respectively. The Cu_2S-ZnS-SnS_2 pseudo-ternary phase diagram, typically referenced when discussing CZTS phase equilibria, is appropriate for synthesis routes based on fixed compositions (e.g., reactants in quartz ampoules). We chose to use the CuS-ZnS-SnS phase diagram in Fig. 3 because we have observed phases such as CuS and Cu_3SnS_4 at co-deposition substrate temperature of 325 °C. However, Cu_2S and SnS_2 secondary phases lying on the Cu_2S-ZnS-SnS_2 plane were also observed in this work, and therefore only a quaternary phase diagram or a non-coplanar pseudo ternary diagram can truly reflect the phase possibilities that can occur during CZTS processing governed by unconstrained reactant amounts.

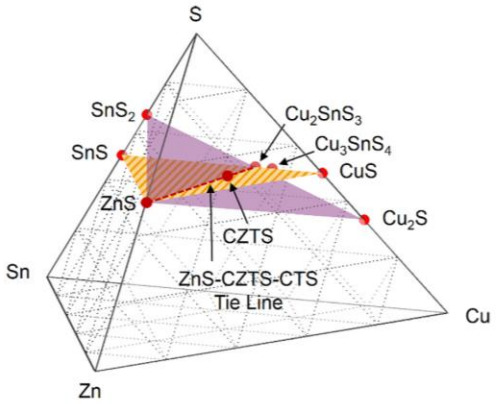

FIG. 4. CZTS quaternary phase diagram including the known phases. Two pseudo-ternary planes each containing CZTS are plotted as intersecting striped yellow and solid purple planes. The planes intersect along the ZnS-Cu_2ZnSnS_4-Cu_2SnS_3 tie line, which is shown in dashed red.

3. Coexistence of phases

Raman spectroscopy x-y mapping in part 1 (Ref. 21) showed Cu_xS phases in the Cu-rich region, SnS_2 phases in the Sn-rich region, and CZTS more concentrated closer to the specular band. Here in part 2, we extend the Raman analysis to investigate the effect of composition on the structurally coherent CZTS and CTS phases in the films deposited at 325 °C. Raman spectra were collected only from the underlying dense film even in the rough Cu- and Sn-rich regions where spectra were collected from areas between surface crystallites. ZnS also co-exists in the dense underlying film, but the excitation wavelength used in this study cannot differentiate ZnS from the structurally similar CTS and CZTS. Therefore, we do not directly analyze the ZnS content or distribution. The film shifts from Cu-rich (Cu/Sn > 2) to Sn-rich (Cu/Sn < 2) transverse to the specular band, while relative Zn-poorness to Zn-richness varies along the specular band. We analyze how these two compositional shifts alter the distribution of structurally coherent phases that comprise the dense CZTS film.

To examine the Cu-rich to Sn-rich regime, Raman spectra (Fig. 5) were collected in four spots A-D (Fig. 1), which lie on a line perpendicular to and near the middle of the specular band of the "regular" combi-CZTS sample, where Zn/(Cu + Zn + Sn) = 0.25, the stoichiometric ratio for CZTS. Both CTS and CZTS are present in all four spectra as indicated by the shoulders at 300 cm^{-1} (CTS) and 370 cm^{-1} (CZTS). The peak at 336.5 cm^{-1} appears most intense in the Sn-rich area, spot D. Tet-CTS and CZTS have nearly identical Raman-active modes (336 cm^{-1} and 337–339 cm^{-1}), so the high peak intensity could arise from higher crystalline quality CZTS within the Sn-rich region. However, we attribute this instead to a high fraction of tet-CTS coexisting with

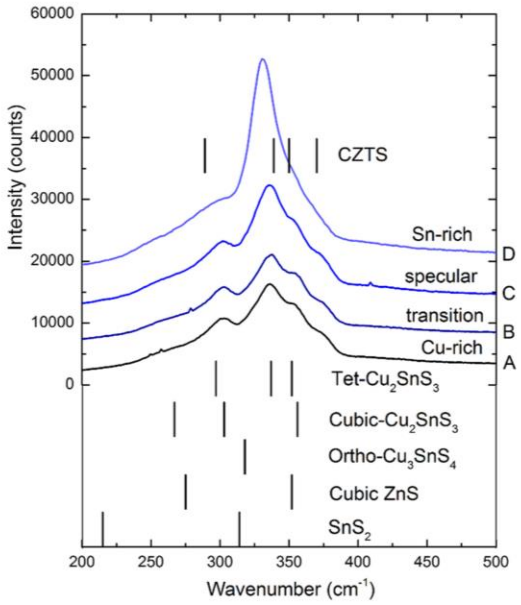

FIG. 5. Raman spectra of sample spots perpendicular to the specular band on the combi-CZTS sample. All expected peak positions are referenced from Fernandes *et al.*[20] Spot locations A-D on the sample are shown in Fig. 2.

CZTS since another tet-CTS Raman mode at 297 cm^{-1} (Ref. 20) is evident and especially broad in the spectrum of the Sn-rich area. Furthermore, the CZTS crystalline quality is expected to be poorer with increased Sn excess,[22] which is confirmed by SEM of the Sn-rich region of a similar sample in part 1 (Ref. 21) showing a porous grain structure within the main absorber layer.

The spectrum of the Sn-rich spot D does not show a resolvable local maximum for the Raman mode of SnS_2 at 318 cm^{-1}, which confirms earlier SEM observations that the structurally dissimilar SnS_2 exists only as a surface phase. Therefore, we conclude that in the Sn-rich region of this sample, tet-CTS co-exists with CZTS and SnS_2 exists only as a surface phase.

In the Cu-rich region (Fig. 5, spot A), more cub-CTS rather than tet-CTS is evident. The cub-CTS peaks at 355 and 303 cm^{-1} are more resolved and higher in intensity relative to the CZTS peaks at 336.5 and 370 cm^{-1}. Raman peaks from Cu_2S and CuS surface phases (expected at 472–475 cm^{-1} (Refs. 20 and 23)) do not appear in the spectrum from the Cu-rich region (Fig. 5, spot A), again confirming phase separation between Cu_xS and CZTS. In addition to the differences in surface phases, the major difference in the Cu- and Sn-rich regions of the sample is the cation ordering of the CTS in the dense absorber layer. Although both cubic and tetragonal phases are structurally coherent with CZTS, Sn-rich compositions favor formation of tet-CTS, while Cu-rich compositions favor more cub-CTS.

A compositionally graded Cu-Sn-S thin film was also grown at 325 °C but without Zn flux to obtain the sample shown in Fig. 6. Peaks from Raman modes of monoclinic-, cub-, and tet-CTS (Cu_2SnS_3) and orthorhombic-Cu_3SnS_4 (ortho-Cu_3SnS_4) are all observed in the spectra of the sample (Fig. 6). Spots 1–3 of the Cu-Sn-S sample follow the general trend of the Zn-containing films, where cub-CTS is favored in the Cu-rich region (Fig. 6, spot 1), and more tet-CTS is formed in the Sn-rich region (Fig. 6, spot 3), but cub-CTS is still dominant in both composition extremes. Spectra of spots 1 and 3 show evidence of both cubic and tetragonal CTS, indicating they coexist under these growth conditions.

Increasing the Cu concentration even more (Fig. 6, spot 4) results in a menagerie of phases including monoclinic-, cub-, and tet-CTS as well as orthorhombic-Cu_3SnS_4. Although cub- and tet-CTS are structurally coherent, monoclinic-CTS and orthorhombic-Cu_3SnS_4 are not.[24–26] This indicates in the initial Cu-rich growth regime at low growth temperatures, compositions of $2 < Cu/Sn < 3$ are more likely to lead to cub- and tet-CTS, which are structurally coherent with CZTS. Gaussian peak fitting of the spectrum from spot 4 (which had the most well-defined peak structures) was attempted, but the resolution of the peak structure is insufficient to warrant fitting with peaks from three separate phases. Thus, the data sets from other analysis spots were also not fitted.

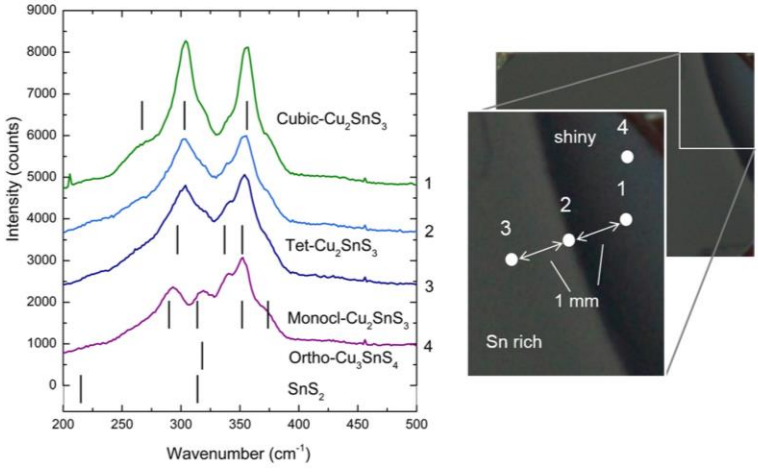

FIG. 6. Raman spectra and optical images of a Cu-Sn-S sample grown under similar conditions as the combi-CZTS samples except without Zn flux. Four distinct phases cubic- and tetragonal-Cu_2SnS_3, monoclinic-Cu_2SnS_3,[24] and orthorhombic-Cu_3SnS_4 are all observed in the Raman spectra. No peak for Cu_2S at 475 cm^{-1} or SnS peaks (below 200 cm^{-1}) are evident in the spectra.

To investigate the effect of Zn on the structurally coherent phases that co-exist with CZTS, Raman spectra of spots 1–9 (Fig. 7) were collected along the specular band, 20 μm from the abrupt transition edge to the Sn-rich region. This series of points thus maintains the constraint Cu/Sn $\sim$ 2, while only the Zn concentration varies. The shoulder at 370 cm^{-1} present in all the spectra of spots 1–9 indicates CZTS presence across the entire specular band. The "CTS shoulder" at $\sim$300 cm^{-1} also exists in all the spectra from the specular band, even in the Zn-rich region.

As the film becomes more Zn-poor, the tet-CTS phase is favored over cub-CTS. The CTS shoulder progressively broadens from the Zn-poor spot 1 spectrum to the Zn-rich spot 9 spectrum. This indicates the increasing fraction of tet-CTS within the coherent CTS/CZTS film. Additionally, the peak intensities of the 303 and 356 cm^{-1} Raman modes of cub-CTS relative to the dominant peak at 336.5 cm^{-1}, common to both CZTS and tet-CTS, are higher in the spectrum of the Zn-poor region (Fig. 7, spot 1). Both the broadening of the CTS shoulder with increased Zn content and the increase in cub-CTS modes in the Zn-poor region indicate a higher cub-CTS fraction in the Zn-poor region of the specular band. Although these data show trends for cub- or tet-CTS preference in either Zn-poor or Zn-rich conditions (respectively), both crystalline structures still co-exist even at the extremes analyzed. Figure 8 displays the clear co-existence of tet-CTS, cub-CTS, and CZTS in the Zn-poor region of the film near spot 1.

Since the CTS shoulder persists in the "regular" sample, a Zn-rich sample grown under similar conditions but with a higher Zn flux was also examined by Raman spectroscopy to determine if raising the Zn fraction in the film would decrease the fraction of CTS. The composition along this "Zn-rich" sample's specular band (Fig. 3) also lies on the ZnS-CZTS-CTS tie line on the CZTS pseudo-ternary phase diagram but with higher Zn fractions than the "regular" sample. Figure 9 compares the Raman spectra of the two samples and demonstrates that despite the Zn-rich composition lying clearly in the region of the pseudo-ternary diagram where CTS is not stoichiometrically favored, the CTS shoulder still persists.

Raman analyses of metal stacks sulfurized at 400 °C also showed CTS presence in samples with stoichiometric CZTS composition.[18] These and our findings differ from Olekseyuk's phase diagram,[4] which indicates CZTS is the thermodynamically stable phase at the stoichiometric CZTS composition on the 670 K ($\sim$400 °C) isotherm. The persistence of CTS despite adequate Zn indicates these thin films have not reached thermodynamic equilibrium at growth temperatures of 325 °C. Because the CTS phase changes with Sn, Cu, and Zn chemical potential across the film, we can observe the changes in composition-dependent cation arrangement by examining the changes in cub- and tet-CTS across these compositionally graded thin films grown at low temperature.

Figure 10 depicts the trend of more cub-CTS bonding characteristics in Cu-rich and Zn-poor regions of the sample

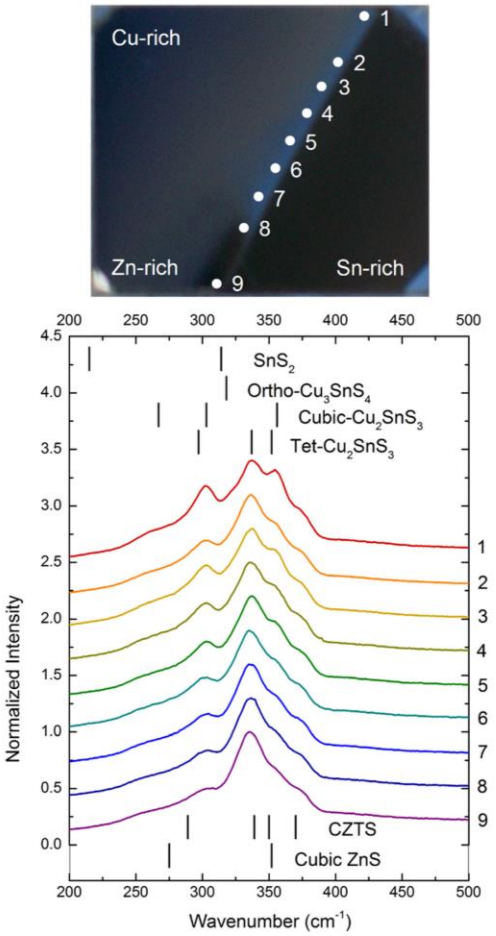

FIG. 7. Raman spectra for spots along the specular band of the regular combinatorial CZTS sample. Reference peak positions expected for CZTS and commonly expected secondary phases are shown below the spectra.[20]

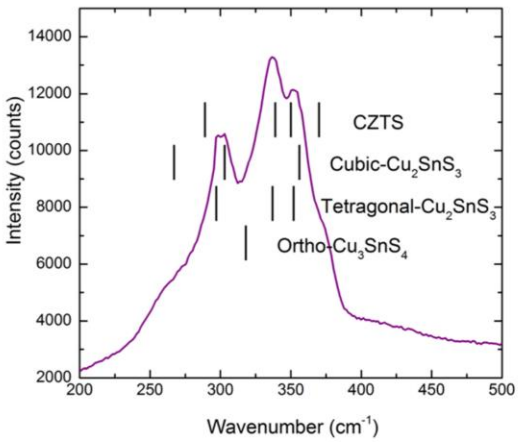

FIG. 8. Co-existence of tet- and cub-CTS phases is clearly discernible in the Raman spectrum collected on the rough side of the specular/rough edge near spot 1 (identified in Fig. 7).

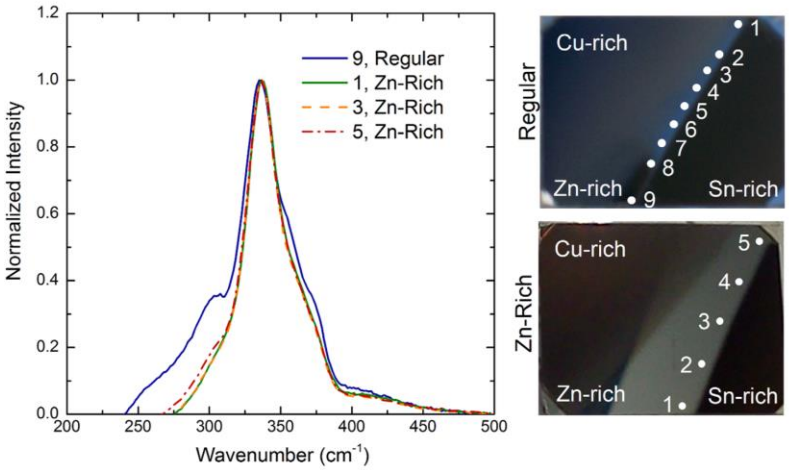

FIG. 9. Raman spectra from the Zn-rich area on the "regular" combi-CZTS sample and from the "Zn-rich" combi-CZTS sample. The spectra are normalized after a linear background subtraction.

grown at 325 °C and more tet-CTS bonding characteristics in Sn- and Zn-rich regions. Note that no region contains exclusively cub- or tet-CTS. Two unit cells of cub-CTS have the same lattice parameters as one unit cell of tet-CTS ($a = 5.434$ Å for cub-CTS and $a = b = 5.412$, $c = 10.810$ Å for tet-CTS (Ref. 25)), so the difference between these phases is not the lattice structure but rather the Cu and Sn cation site occupations. The metals are randomly distributed in cub-CTS, whereas the Cu and Sn site occupation within tet-CTS is more ordered (Figs. 11(a) and 11(b)).

For tet-CTS, the 2a Wyckoff cation sites with coordinates (0,0,0) are occupied only by Cu, leaving the remaining 4d and 2b cation sites with coordinates of $(0,1/2,1/4)$ and $(0,0,1/2)$ having observed 44% or 46% probability of Sn occupation[28] (Fig. 11(b)). In cub-CTS, random distribution results in only 33% probability that Sn will occupy *any* cation site in the lattice (Fig. 11(a)). When comparing these site occupation probabilities with kesterite and stannite CZTS (Figs. 11(c) and 11(d)) and considering that Zn can more easily displace Cu than Sn,[29] it is evident that tet-CTS has a higher probability for 2a and 2b sites having the same metal occupation as kesterite or stannite CZTS. However, cub-CTS has a higher probability that 4d sites will have the same metal occupation as kesterite or stannite CZTS assuming facile Cu/Zn exchange. Since a clear conclusion such as "the probability of Cu and Sn arrangement in tet-CTS is more like kesterite (or stannite) CZTS than for cub-CTS" cannot be drawn, thinking of cation arrangement in a different way may be more helpful.

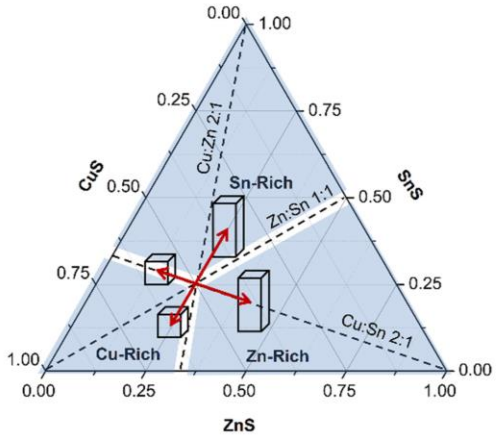

FIG. 10. The Cu/Sn = 2, Cu/Zn = 2, and Zn/Sn = 1 tie lines, which determine the boundaries for Cu-, Sn-, and Zn-rich regions on the pseudo-ternary diagram are all drawn, and each zone is labeled. Cu-rich conditions are Cu/Sn > 2 and Cu/Zn > 2. Sn-rich conditions are Cu/Sn < 2 and Zn/Sn < 1. Zn-rich conditions are Cu/Sn < 2 and Zn/Sn > 1. The trends in crystalline structures of the Cu_2SnS_3, which co-exists with CZTS and ZnS within these different compositional regions on films grown at 325 °C, are depicted by either a cube (cubic-Cu_2SnS_3) or a cuboid (tetragonal-Cu_2SnS_3).

Zhai *et al.*[13] emphasize differences in cation arrangement can also be viewed as differences in tetrahedral coordination of the metallic cations to the sulfur atom within the CTS lattice. The most stable CTS structures are predicted to be a combination of Cu_3Sn and Cu_2Sn_2 coordination to the S atoms.[13] For the Cu-Sn-S system, a Cu_3Sn tetrahedral coordination (Fig. 11(e)) is most analogous to kesterite and stannite CZTS, which both have Cu_2ZnSn tetrahedral coordination for S atoms. Although differences between tet- or cub-CTS can be discussed as differences of Cu or Sn occupation on specific sites or differences in the tetrahedral coordination to the S atom, the main point is the cation arrangement within CTS phase changes with composition. At typical growth temperatures for CZTSe coevaporation, CTSe is not observed, and CZTSe forms from Cu_xSe, ZnSe, and SnSe,[17] so we also examined a film grown at 470 °C to determine how composition variation affected CZTS.

B. High temperature film deposited at 470 °C

1. Surface morphology and composition

Part 1 (Ref. 21) of this study showed that the major morphological difference between the samples grown at 325 °C and 450 °C was the conversion of the entire Sn-rich (Cu/Sn < 2) rough region into a specularly reflective film. The higher growth temperature allowed for self-limiting

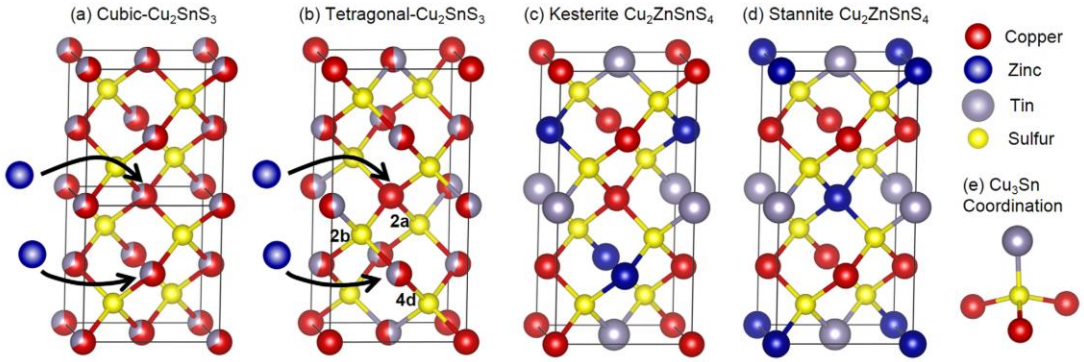

FIG. 11. (a) Two unit cells of cubic-Cu_2SnS_3, (b) tetragonal-Cu_2SnS_3,[27] (c) kesterite, and (d) stannite Cu_2ZnSnS_4.[28] Both cub- and tet-CTS have the same cation sites, but the probability of Cu (red) or Sn (gray) occupation differs and is represented by partial coloring of each atom. Zn (blue) substitution on the 2a and 4d sites of tet-CTS and the analogous sites in the cub-CTS are represented and emphasizes the difference in Zn displacing Cu vs. Sn to form kesterite or stannite CZTS. (e) Cu_3Sn tetrahedral coordination to S (yellow).

incorporation of SnS;[14,15,17] therefore, the compositions of the regions under excess Sn flux collapsed to the CZTS-CTS-ZnS tie line and thus were specularly reflective because they lacked Sn_xS_y surface phases. The sample examined in this second part of the study was grown at 470 °C. It would otherwise be specularly reflective like the samples grown at 450 °C in part 1, except excess Sn and S fluxes were used during cooling in an attempt to prevent CZTS decomposition. As a result, Sn_xS_y phases, which appear as faceted and flake-like grains in SEM, are present on the surface of the entire sample. There is no obvious specular band on this sample but specular reflectivity is observed when viewed at glancing angles. Figure 12(a) displays the composition range of this sample on the pseudo-ternary phase diagram. As is expected for Sn-rich samples at high growth temperatures, the composition lies nearly on the CTS-CZTS-ZnS tie line. Figure 12(b) displays the corresponding Raman spectra of the sample's four corners and the center.

2. Coexistence of phases

Although the surface morphology and film porosity improves for Sn-rich regions at higher growth temperatures in part 1, the PL studies showed a dramatic drop in intensity from the regions with Cu-rich to Sn-rich fluxes. This likely resulted from deleterious Sn-related native point defects. In the Cu-rich regions (Cu/Sn > 2) of these same films, however, the PL intensity increased as the Zn concentration of

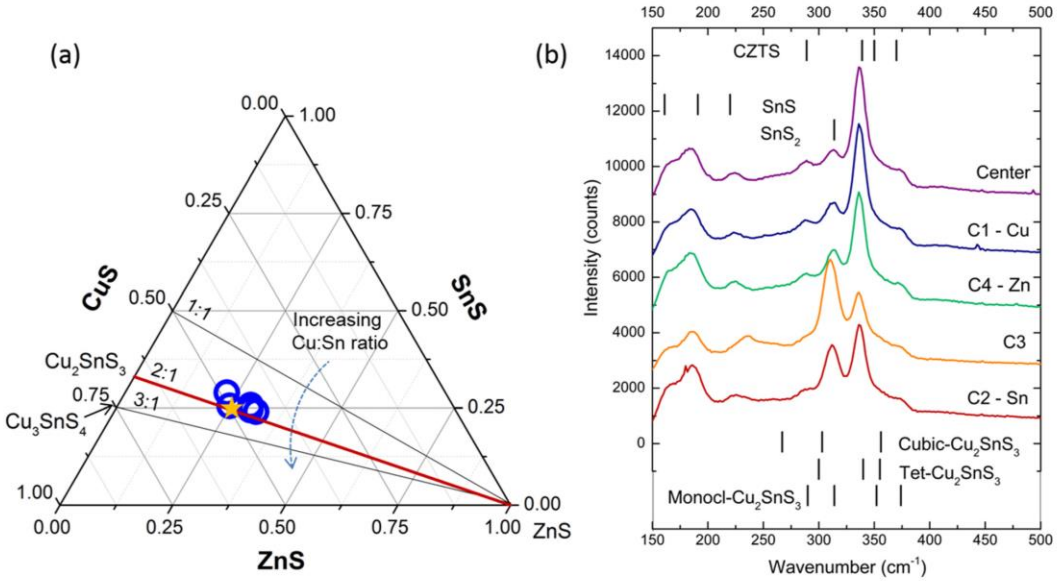

FIG. 12. The compositions of the middle and four corners of a thin film of CZTS deposited at 470 °C are plotted on the pseudo-ternary diagram (a). The Raman spectra of five spots, the center and C1-C4 (corners 1–4), are plotted on the graph in (b). Reference peak positions[20] expected for CZTS and commonly expected secondary phases are shown on the Raman plots.

the film increased. This second portion of the study uses Raman spectroscopy to further investigate the effect of composition variation during higher growth temperatures. Only CZTS (no CTS) was present, and the overall CZTS crystalline quality increased compared to the 325 °C samples. We also found that excess Sn flux during growth induced more crystalline disorder (variation in metal-sulfur vibrational mode energy) in CZTS; however, the crystalline quality is relatively insensitive to excess Zn.

The Raman spectra of the 4 corners and the center of the sample deposited at 470 °C (Fig. 12(b)) indicate that CZTS is present across the entire film. The characteristic CTS shoulder at 300 cm^{-1} prevalent in the samples deposited at 325 °C does not appear in these spectra and indicates the lack of CTS at this higher growth temperature. Note again that ZnS may be present in these composition extremes; however, it is difficult to differentiate from CZTS via Raman using a visible laser. Unlike the samples deposited at 450 °C in part 1 of this study, Sn_xS_y phases are observed over the entire sample surface due to the Sn flux exceeding the Sn/SnS vapor pressure during cooling from the growth temperature to prevent CZTS decomposition. The Sn_xS_y peaks in the spectra are not a direct result of increased growth temperature, and are not expected to change the overall trends for CZTS crystalline quality discussed later since they occur post-deposition as surface phases. However, we discuss them to show the possible phases that may occur under such post-deposition conditions and emphasize there is no major overlap between CZTS and Sn_xS_y Raman active modes.

Peaks at 166, 184, and 223 cm^{-1} (Fig. 12(b)) indicate SnS presence on the surface of the film. The observed peaks differ from previously reported results[20] for SnS at 160, 190, and 219 cm^{-1}. However, the 2_{Ag} mode was observed[20,30,31] in the range of 219–223 cm^{-1}, and the B_{2g} mode, which is the most intense peak observed by us and Fernandes *et al.*,[20] is observed as low as 182 cm^{-1} in SnS nanoparticles.[32] A peak shift may occur with variation in the Sn-S coordination in the Sn_xS_y phases, where x and y are not integers. The peak at 314 cm^{-1}, in the spectra of three of the four corners and the center of the sample (Fig. 12(b), center, Zn, Cu, and Sn) corresponds to SnS_2.[20] The spectrum from the corner with more sulfur relative to the metals' compositional fraction has Raman modes at 310 and 235 cm^{-1}, which correspond more closely to previously reported[33] Sn_2S_3 Raman active modes (307 and 234 cm^{-1}) rather than those of SnS or SnS_2.

The main differences between the combi-CZTS films deposited at 325 °C and 470 °C as seen in the Raman spectra (Fig. 13) are the disappearance of the CTS phase and the increased crystalline quality of the CZTS. Figure 13 directly compares Raman spectra from combinatorial CZTS grown at 325 and 470 °C. The low temperature spectrum (dashed line) was collected from spot 9 on the "regular CZTS" sample grown at 325 °C (Fig. 7), and the spectrum for the high temperature sample (solid line) was collected from the center of the high temperature film (Fig. 12(b), center). The FWHM (full width at half maximum) of the main CZTS peak at 336.5 cm^{-1} decreased from 25 cm^{-1} to 15 cm^{-1} as the growth temperature was increased from 325 to 470 °C. This

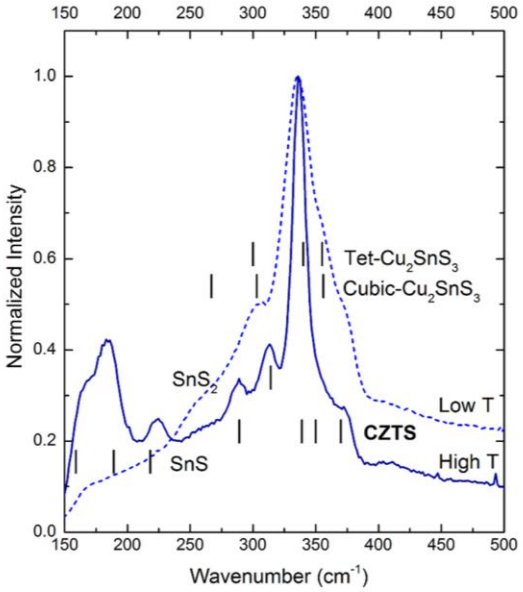

FIG. 13. Raman spectra of films deposited at 325 °C (low T, dotted line) and at 470 °C (high T, solid line) are compared with background subtraction and normalization. The narrower CZTS peak at 336.5 cm^{-1} for the high temperature sample indicates higher crystalline perfection.

decrease in CZTS peak width indicates longer phonon mean free path and thus a higher degree of crystalline order.

In addition to increased deposition temperature, a Cu-rich (Cu/Sn > 2) composition also results in more ordered CZTS. Raman spectra from corner 3 (Cu/Sn = 1.7) and the center (Cu/Sn = 1.9) are selected to compare, since these points both maintain constant Cu/Zn = 1.5, and lie within the desired final Cu-poor, Zn-rich regime. The FWHM of the main CZTS peak at 336.5 cm^{-1} increases almost 50% from 15 to 22 cm^{-1} with only 4% increase in the Cu/(Cu + Sn) ratio. The peak at 336.5 cm^{-1} arises from the A mode in CZTS and is attributed only to anion motion.[34] Since sulfur is coordinated to all metals in CZTS, this FWHM analysis is sensitive to crystalline disorder that may result from cation substitution or vacancies of any of the three metals. The trend of decreasing crystalline quality with increased Sn flux during film growth is also evident when comparing corners 1 (Cu) and 2 (Sn), where the FWHM increases from 15 to 18 cm^{-1} for regions under high Cu vs. high Sn fluxes. The observation of lower crystalline order with higher Sn flux despite the self-limiting nature of SnS and improved morphology at a higher growth temperature agrees with the attribution of low PL response observed in part 1 to higher concentrations of Sn-related native defects.

Conversely, a Zn-rich (Cu/Zn < 2) flux during growth at 470 °C does not significantly impact the crystalline quality of the CZTS within the Cu-rich region. The Raman spectra from corners 4 (Cu/Zn = 1.9) and 1 (Cu/Zn = 1.4) (Fig. 12(b), 4-Cu and 1-Zn) are selected to compare, since these points both maintain a constant Cu/Sn = 1.8. An 18% mole fraction increase in Zn/(Cu + Zn) from corner 4 to corner 1 does not change the 15 cm^{-1} FWHM of the main CZTS peak at 336.5 cm^{-1}. Both

spectra show the same FWHM as well as relatively similar peak intensities. This insensitivity of the FWHM of the CZTS peak to the Zn content in the final film indicates that excess Zn does not induce significant variation in the metal-sulfur bonds from native antisite defects within the CZTS grains to the same extent as the disruptive effects of excess Sn.

Two stage coevaporation of CZTSe[6,17] harnesses the benefits of both initial Cu-rich growth ($Cu/(Zn + Sn) > 1$) for larger grains, and final Zn-rich growth that results in the Cu-poor, Zn-rich composition near the buffer layer interface common to all high efficiency CZTSSe devices. Sn incorporation into CZTS(Se) has been assumed to be self-limiting during growth with sufficiently high Sn and S(Se) vapor pressures. Part 1 shows a dramatic drop in PL intensity related to excess Sn flux on samples grown at 450 °C even though the final CZTS composition remains stoichiometric. In films grown at 325 °C which are kinetically trapped, we observed a change in Cu and Sn arrangement, evident by the shift in the CTS secondary phase from more cub-CTS in the Cu-rich region ($Cu/Sn > 2$) to more tet-CTS in Sn-rich region ($Cu/Sn < 2$). For CZTS samples grown at 470 °C (similar to those in part 1), the volatile CTS is not present, and regions grown under excess Sn flux are more disordered than Cu-rich regions, evident by an increased FWHM in the peak for the Raman active A mode of CZTS. Therefore, increasing Sn chemical potential changes cation arrangement in CTS and results in more CZTS lattice disorder. These findings suggest that high Sn chemical potential adversely changes the cation arrangement within CZTS. However, experiments that directly measure the change in cation ordering in CZTS with variance in Sn chemical potential are necessary to validate this theory.

During the initial Cu-rich growth of CZTSe during 2-stage coevaporation, Cu_xS phases may induce larger grain growth[6] by precipitating dendritic structures of the precursor CTS (or CZTS) within the Cu_xS matrix, similar to the effects[35] of growing $CuInSe_2$ in the presence of Cu_xSe which promotes fluxing and increased lateral grain growth. Mousel *et al.*[19] also showed that precursors grown in Cu-rich conditions led to higher device efficiencies after the Cu_xSe phases were etched out of Cu-Zn-Sn-Se precursors before selenization, leaving the final CZTS film composition Cu-poor. This highlights that the benefits of initial Cu-rich growth extend beyond the fluxing assistance from $Cu_xS(Se)$. We postulate initial Cu-rich ($Cu/Sn > 2$) CZTS growth results in a more ordered CZTS lattice due to favorable tetrahedral Cu_3Sn or Cu_2ZnSn coordination to the S atom, whereas Sn-rich growth may favor multiple Sn atoms coordinated to one S atom. The antisite defect formation energies predicted by Chen *et al.*[29] indicate relatively low energies for Cu/Zn exchanges, higher energies for Sn/Zn exchange, and the highest energies for Sn/Cu exchange. Therefore, growth with $Cu/Sn > 2$ may secure Sn site occupancy with low Sn antisite defects. When more Zn is introduced later during coevaporation, the Zn atoms are more likely to displace a Cu atom as opposed to a Sn atom. We finally propose that finely controlling the Sn chemical potential within Cu-rich growth environment may establish preferred Cu_3Sn or Cu_2ZnSn coordination to the S atom and lead to fewer Sn antisite defects in CZTS. This is to say that simply supplying a large SnS(Se) overpressure may be sufficient to prevent CZTS decomposition; however, this strategy will guarantee the presence of minority carrier lifetime-killing deep states and thus the degree of SnS excess must be carefully tuned. Furthermore, the Zn_{Sn} antisite defect may be relatively benign, whereas the Cu_{Sn} or V_{Sn} defects are deeper within the bangap.[29] Thus, excess Zn may benefit a slight Sn deficiency without deleterious effects to overall CZTS lattice disorder. This is in agreement with part 1 (Ref. 21) that shows increased PL intensity with increased Zn fraction within the $Cu/Sn > 2$ region of the films grown at 450 °C.

IV. CONCLUSIONS

Morphological studies of compositionally graded CZTS thin films grown at 325 °C reveal a specular band with composition lying on the ZnS-CZTS-CTS tie line on the pseudo-ternary phase diagram containing CZTS.[21] In the low temperature combi-CZTS films, observed surface phases of CuS and SnS_2 did not appear in the Raman spectra of the underlying dense CZTS layer, indicating that only structurally coherent phases (cub- and tet-CTS and ZnS) are incorporated in the CZTS film, and all structurally incoherent secondary phases (CuS, SnS_2) are embedded as separate grains or exist only as surface phases. Determination of secondary phases using Raman spectroscopy shows a CTS phase across the entire sample, even in Zn-rich regions. The more disordered cub-CTS intermediate forms preferentially to the more ordered tet-CTS in Cu-rich and Zn-poor compositions, which are the initial growth conditions in 2 stage coevaporation, which lead to better grain growth and ultimately higher device efficiencies. The shift from tetragonal to cubic-CTS phase indicates a change in Cu and Sn cation order with a shift in composition. A higher growth temperature of 470 °C results in CZTS with no CTS, and better crystalline quality is obtained in the Cu-rich regions of the films. The Zn fraction has no measurable effect on crystalline quality at these higher growth temperatures. Considering both the low and high temperature growth results, we propose the observed higher crystalline quality in initial Cu-rich, Zn-poor growth of CZTS is related to the cation site occupations within the zinc-blende lattice, common to ZnS, CTS, and CZTS, which can be manipulated with composition. Initial Cu-rich growth during 2-stage coevaporation of CZTS may form more favorable Cu_3Sn or Cu_2ZnSn tetrahedral coordination on the S atoms, which may lead to fewer Sn antisite defects in CZTS. A Zn-rich final film composition with $Cu/Sn < 2$, which is obtained during the second stage, does not deleteriously affect overall CZTS crystalline quality.

ACKNOWLEDGMENTS

The research at the University of Utah was supported in whole by the U.S. Department of Energy, Office of Basic Energy Sciences, Division of Materials Sciences and Engineering under Award No. DE-SC0001630. The work at NREL was supported by the U.S. Department of Energy under Contract No. DE-AC36-08GO28308 with the National Renewable Energy Laboratory.

[1]W. Wang, M. T. Winkler, O. Gunawan, T. Gokmen, T. K. Todorov, Y. Zhu, and D. B. Mitzi, Adv. Energy Mater. (published online).
[2]T. K. Todorov, J. Tang, S. Bag, O. Gunawan, T. Gokmen, Y. Zhu, and D. B. Mitzi, Adv. Energy Mater. **3**, 34 (2013).
[3]B. Shin, O. Gunawan, Y. Zhu, N. A. Bojarczuk, S. J. Chey, and S. Guha, Prog. Photovoltaics **21**, 72 (2013).
[4]I. Olekseyuk, I. V. Dudchak, and L. V. Piskach, J. Alloys Compd. **368**, 135 (2004).
[5]S. Chen, X. G. Gong, A. Walsh, and S. Wei, Appl. Phys. Lett. **96**, 021902 (2010).
[6]I. Repins, C. Beall, N. Vora, C. DeHart, D. Kuciauskas, P. Dippo, B. To, J. Mann, W.-C. Hsu, A. Goodrich, and R. Noufi, Sol. Energy Mater. Sol. Cells **101**, 154 (2012).
[7]K. Wang, B. Shin, K. B. Reuter, T. Todorov, D. B. Mitzi, and S. Guha, Appl. Phys. Lett. **98**, 051912 (2011).
[8]J. Timo Waütjen, J. Engman, M. Edoff, and C. Platzer-Bjoürkman, Appl. Phys. Lett. **100**, 173510 (2012).
[9]J. Just, D. Luützenkirchen-Hecht, R. Frahm, S. Schorr, and T. Unold, Appl. Phys. Lett. **99**, 262105 (2011).
[10]A. Fairbrother, E. García-Hemme, V. Izquierdo-Roca, X. Fontané, F. A. Pulgarín-Agudelo, O. Vigil-Galán, A. Pérez-Rodríguez, and E. Saucedo, J. Am. Chem. Soc. **134**, 8018 (2012).
[11]A. Walsh, S. Chen, X. G. Gong, S.-H. Wei, J. Ihm, and H. Cheong, AIP Conf. Proc. 63–64 (2011).
[12]B. G. Mendis, M. C. J. Goodman, J. D. Major, A. A. Taylor, K. Durose, and D. P. Halliday, J. Appl. Phys. **112**, 124508 (2012).
[13]Y.-T. Zhai, S. Chen, J.-H. Yang, H.-J. Xiang, X.-G. Gong, A. Walsh, J. Kang, and S.-H. Wei, Phys. Rev. B **84**, 075213 (2011).
[14]A. Weber, R. Mainz, and H. W. Schock, J. Appl. Phys. **107**, 013516 (2010).
[15]J. J. Scragg, T. Ericson, T. Kubart, M. Edoff, C. Platzer-Björkman, and C. Platzer-bj, Chem. Mater. **23**, 4625 (2011).
[16]A. Redinger, D. M. Berg, P. J. Dale, and S. Siebentritt, J. Am. Chem. Soc. **133**, 3320 (2011).
[17]G. Kaune, S. Hartnauer, F. Syrowatka, and R. Scheer, Sol. Energy Mater. Sol. Cells **120**, 596 (2014).
[18]A.-J. Cheng, M. Manno, A. Khare, C. Leighton, S. A. Campbell, and E. S. Aydil, J. Vac. Sci. Technol., A **29**, 051203 (2011).
[19]M. Mousel, T. Schwarz, R. Djemour, T. P. Weiss, J. Sendler, J. C. Malaquias, A. Redinger, O. Cojocaru-Mirédin, P.-P. Choi, and S. Siebentritt, Adv. Energy Mater. **4**(2) (2013).
[20]P. A. Fernandes, P. M. P. Salomé, and A. F. da Cunha, J. Alloys Compd. **509**, 7600 (2011).
[21]H. Du, F. Yan, M. Young, B. To, C.-S. Jiang, P. Dippo, D. Kuciauskas, Z. Chi, E. A. Lund, C. Hancock, W. M. Hlaing OO, M. A. Scarpulla, and G. Teeter, J. Appl. Phys. **115**, 173502 (2014).
[22]J. J. Scragg, *Copper Zinc Tin Sulfide Thin Films for Photovoltaics* (Springer Berlin Heidelberg, Berlin, 2011).
[23]B. Minceva-Sukarova, M. Najdoski, I. Grozdanov, and C. J. Chunnilall, J. Mol. Struct. **410–411**, 267 (1997).
[24]D. M. Berg, R. Djemour, L. Gütay, S. Siebentritt, P. J. Dale, X. Fontane, V. Izquierdo-Roca, and A. Pérez-Rodriguez, Appl. Phys. Lett. **100**, 192103 (2012).
[25]P. A. Fernandes, P. M. P. Salomé, and A. F. da Cunha, J. Phys. D: Appl. Phys. **43**, 215403 (2010).
[26]F. Hergert and R. Hock, Thin Solid Films **515**, 5953 (2007).
[27]X. Chen, H. Wada, A. Sato, and M. Mieno, J. Solid State Chem. **139**, 144 (1998).
[28]S. Chen, X. G. Gong, A. Walsh, and S.-H. Wei, Appl. Phys. Lett. **94**, 041903 (2009).
[29]S. Chen, A. Walsh, X.-G. Gong, and S.-H. Wei, Adv. Mater. **25**, 1522 (2013).
[30]X.-L. Gou, J. Chen, and P.-W. Shen, Mater. Chem. Phys. **93**, 557 (2005).
[31]Y. Liu, D. Hou, and G. Wang, Chem. Phys. Lett. **379**, 67 (2003).
[32]S. Sohila, M. Rajalakshmi, C. Ghosh, A. K. Arora, and C. Muthamizhchelvan, J. Alloys Compd. **509**, 5843 (2011).
[33]L. S. Price, I. P. Parkin, A. M. E. Hardy, R. J. H. Clark, T. G. Hibbert, and K. C. Molloy, Chem. Mater. **11**, 1792 (1999).
[34]T. Gürel, C. Sevik, and T. Çağın, Phys. Rev. B **84**, 205201 (2011).
[35]J. S. Park, Z. Dong, S. Kim, and J. H. Perepezko, J. Appl. Phys. **87**, 3683 (2000).

CHAPTER 5

MODELING CU_2ZNSNS_4 (CZTS) SOLAR CELLS WITH KESTERITE AND STANNITE PHASE VARIATION

Modeling Cu_2ZnSnS_4 (CZTS) solar cells with kesterite and stannite phase variation

Elizabeth A. Lund[a] and Michael A. Scarpulla*[b,c]
[a]Dept. of Chemical Engineering, 50 S. Central Campus Dr. Rm. 3290, Salt Lake City, UT, USA 84112-9203; [b]Dept. of Materials Science and Engineering, 122 S. Central Campus Dr. Rm. 304, Salt Lake City, UT, USA 84112-9203; [c]Dept. of Electrical Engineering, 50 S. Central Campus Dr. Rm. 3280, Salt Lake City, UT, USA 84112-9203

ABSTRACT

Cu_2ZnSnS_4 (CZTS) may exhibit both kesterite and stannite polymorphs and shows promise as an absorber layer in thin film photovoltaic solar cells to be produced at terawatt scales. This study examines the effects of CZTS polymorphism and inhomogeneous distributions of CZTS polymorphs on device characteristics under scenarios of single phase films, a sinusoidal variation between kesterite and stannite with depth, and single phase films with thin layers of the other polymorph at both interfaces. In general, stannite-only devices are predicted to have higher efficiency than kesterite-only devices and sinusoidal grading results in efficiency between those of the pure phases. However, the device performance is relatively insensitive to the wavelength of the sinusoidal grading and rather is very sensitive to the phase present at the CdS interface. Predicted AM1.5 current-voltage (J-V) curves and descriptive metrics as well as wavelength-resolved quantum efficiencies are reported for all models. Based on these results, we propose control of cation ordering in CZTSSe as a mechanism for device design using bandgap grading and interface engineering without variation of stoichiometry.

Keywords: CZTS, Cu_2ZnSnS_4, kesterite, stannite, photovoltaic

*scarpulla@eng.utah.edu

1. INTRODUCTION

Cu_2ZnSnS_4 (CZTS) and the closely-related $Cu_2ZnSnSe_4$ (CZTSe) are natively p-type I_2-II-IV-VI_4 semiconductors that show promise as absorber layers in thin film photovoltaic solar cells. The geological and industrial availability of their constituent elements, high absorption coefficients allowing thin film devices, and the ability to use group IV and VI alloying[1,2] to vary the bandgap across the maximum of the Shockley-Quiesser maximum efficiency curve all point to the possibility for CZTSSe devices to be utilized at terawatt scales. Research interest in this novel earth-abundant material is high, but the record cell efficiency of 11.1%[1] is just over half that of CZTSe's parent compound, $Cu_2(In,Ga)Se_2$ (CIGSe) record efficiency of 20.3%[3]. Increasing device efficiency requires understanding CZTSSe's material properties, but the quaternary nature of CZTS complicates this endeavor. Since phase-pure CZTSSe only exists within a small compositional range[4], small fluctuations in composition can lead to a wide variety of defects and secondary phases. These localized differences lead to spatially inhomogeneous electrostatic potentials that may reduce overall device efficiency by lowering carrier separation and lifetimes.

Another complication with CZTSSe is the mixed cation site occupancy on Cu and Zn sites. This phenomenon may also be thought of as a continuous series of polymorph random alloys. The most enthapically-stable ordered phase (at least as 0 K) is predicted to be the tetragonal kesterite phase, which is closely followed by the stannite. These two phases' formation energies are predicted to differ by only 1.3 meV/atom[5], so it is very plausible that they may coexist in a CZTS film or device, even within a single polycrystalline grain. Since the difference between kesterite and stannite is merely

Physics, Simulation, and Photonic Engineering of Photovoltaic Devices II, edited by Alexandre Freundlich, Jean-Francois Guillemoles, Proc. of SPIE Vol. 8620, 862015 · © 2013 SPIE
CCC code: 0277-786X/13/$18 · doi: 10.1117/12.2012401

cation rearrangement along the [001] axis[6] (c.f. Fig. 1) which can be achieved via the formation of Cu_{Zn} and Zn_{Cu} antisite pairs, it is plausible that real CZTS should vary continuously between stannite and kesterite locally and in general on different length scales. Mendis et al. used aberration corrected scanning transmission electron microscopy to observe compositional inhomogeneity along the [001] axis on the scale of 1.5-5 nm[7]. Similar cation disordering of Cu and Zn along the same axis has also been observed via neutron and x-ray diffraction by Schorr and colleagues[8,9] and by anomalous x-ray diffraction. Recently, evidence for electronic implications of significant disordering in CZTSSe alloys (of unidentified origin) has been shown in studies of photocapacitance by the groups at IBM and University of Oregon[10].

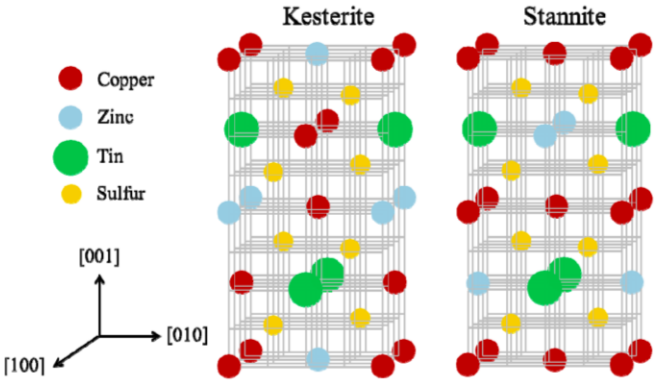

Figure 1. The crystal structure of kesterite and stannite CZTS. The axes in the lower left of the figure display the crystal orientation.

Persson et al. predict a band gap energy of 1.56 eV for kesterite and 1.42 eV for stannite CZTS[5], which are also in line with other calculations and experiments. These values are thus adopted for this work. While the difference of 140 meV between the polymorphs' bandgaps are within the statistical scatter of reported experimental energy gaps from the literature, there is no compelling evidence that any macroscopic CZTSSe sample produced to date is actually 100% kesterite or 100% stannite in light of the above findings of cation disordering[11-13]. We note that many other effects such as sample thickness, strain, Burstein-Moss shift, 2nd phases, grain boundary electronic structure, and band tailing can modify the bandgap apparent via different experimental techniques. Thus we focus on the prediction that stannite CZTS has approximately a 10% lower bandgap than kesterite and examine this implication. This study investigates the changes to device physics resulting from spatial distributions of kesterite and stannite in the CZTS layer. Device performance is evaluated for different length scales of the phase variation and for different phases present at the interfaces of the CZTS.

2. METHODOLOGY

Solar cell devices consisting of a standard Al/ZnO:Al/i-ZnO/CdS/CZTS/Mo multilayer stack were simulated using SCAPS, a program developed specifically for modeling thin film polycrystalline devices[14].

2.1 Full Device Stack

The only variations in the reported scenarios below occur in the CZTS layer's polytype distribution and thickness. The rest of the solar cell device and illumination conditions remain unchanged in all scenarios herein. Only radiative recombination in the CZTS layer (i.e. space charge region recombination) was assumed with a radiative coefficient of 7.2E-10 cm^3/s for CZTS. No interface defects or interface-specific properties were added. The CdS and i-ZnO layers contain "neutral" defects which provide carriers but do not contribute to the space charge region. All simulations were run under AM 1.5, one-sun front-side illumination and all quantum efficiency (IQE) curves were baseline subtracted such that QE=0 for $\lambda > 900$ nm. The model was adapted from the NUMOS CIGS example distributed with SCAPS [14], with the addition of an i-ZnO layer and flat bands at the back contact.

2.2 CZTS Absorber Layer

CZTS was modeled as a semiconductor with background hole concentration of $2x10^{16}$ /cm^3 having neither ionizable shallow dopants nor recombination centers. The band gap, dielectric permittivity, conduction and valence band effective density of states, electron and hole thermal velocities, and absorption constant were used directly or calculated from data reported in Ref. [5]. The hole mobility was estimated to be 10 cm^2/Vs, which may be reasonable for intra-granular transport [15]. The energy band alignment at the CZTS/CdS interface is based on previous theoretical and experimental findings. Chen et al postulate that cation cross-substitution in the closely related quaternary chalcogenide Cu_2GeZnS_4 results in mainly a conduction band minimum downshift from the polytype kesterite to stannite[16]. Nagoya et al. predict ΔE_V=0.3-0.57 eV for the CdS/kesterite CZTS band offset[17], and the record efficiency CZTS solar cell is reported to have a CZTS/CdS Type 1 (straddling) band alignment with ΔE_V=0.54 eV[18]. Therefore, the energy band offsets at the CdS/CZTS interface in the models of this work were chosen to be ΔE_V=0.54 eV for both polytypes, with the 140 meV difference between kesterite and stannite reflected only as a change in the conduction band minimum. The CZTS absorber layer in the device models includes one or both kesterite and stannite phases. Models with CZTS layers containing mixed polytypes are shown in Fig. 2. The sinusoidally-graded models may contain either kesterite or stannite at the absorber interfaces, whereas the sandwich structure contains only stannite on the inside and kesterite at the interfaces.

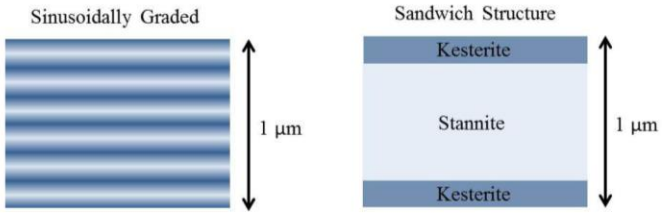

Figure 2. A mixed-polytype CZTS solar cell model is either either sinusoidally graded between kesterite and stannite, or it is a sandwich structure.

For the sinusoidally varied polytype simulations, the percentage of kesterite and stannite is modulated through the full thickness of the CZTS layer with all polytype parameters linearly dependent on phase fraction. The sinusoidal periods were chosen such that integer numbers of full periods equals the layer thickness. Thus the interfaces are either phase-pure kesterite or stannite and the absorber layer is always 50% of each polymorph. Sinusoidal phase grading between the two phases have been tested for length scales in the range of 50-5 nm. We acknowledge that quantum confinement may affect real material and device properties under such scenarios, however confinement is not accounted for in these calculations. The typical absorber layer thickness in current CZTS devices is approximately 1 μm, and this thickness was used when computationally possible. Due to current total mesh point number constraints in SCAPS, an overall CZTS layer that is thinner than 1 μm is required to accurately represent the phase grading for smaller length scales. Thus results for devices with CZTS thicknesses of 1 μm and 400 nm are reported. Again, we focus on extracting relative trends with other variables held constant.

3. RESULTS AND DISCUSSION

3.1 Sinusoidal Grading

The illuminated current density – voltage (JV) parameters for 1 μm and 400 nm thick CZTS absorber layers in a full device stack are reported in Table 1, and the QE curves for these same models are displayed in Figure 3.

Table 1. Light JV parameters from solar cell device models containing a 1 μm or 400 nm thick CZTS absorber layer, which is a single phase of kesterite or stannite, or the layer sinusoidally graded kesterite/stannite with either kesterite (KS) or stannite (ST) at both the front and back interfaces. All energy band offsets are Type 1. The underlined values are the higher value in the comparison between the interfaces being kesterite or stannite.

CZTS Thickness	CZTS Layer Structure	Phase at Interfaces	η (%)	V_{OC} (Volt)	J_{SC} (mA/cm^2)	FF (%)
1 μm	50 nm Sinusoidal	KS	17.8	1.025	20.6	84.2
		ST	13.2	0.996	16.8	79.2
	Single Phase	KS	16.8	1.070	18.3	85.5
		ST	17.9	0.949	22.4	84.1
400 nm	5 nm Sinusoidal	KS	13.8	1.034	15.3	87.2
		ST	10.6	0.962	14.5	75.9
	10 nm Sinusoidal	KS	13.8	1.034	15.3	87.0
		ST	10.4	0.966	14.4	75.2
	50 nm Sinusoidal	KS	13.6	1.033	15.2	86.9
		ST	10.4	0.968	14.3	74.8
	Single Phase	KS	12.4	1.060	13.6	86.1
		ST	13.4	0.939	16.8	85.0

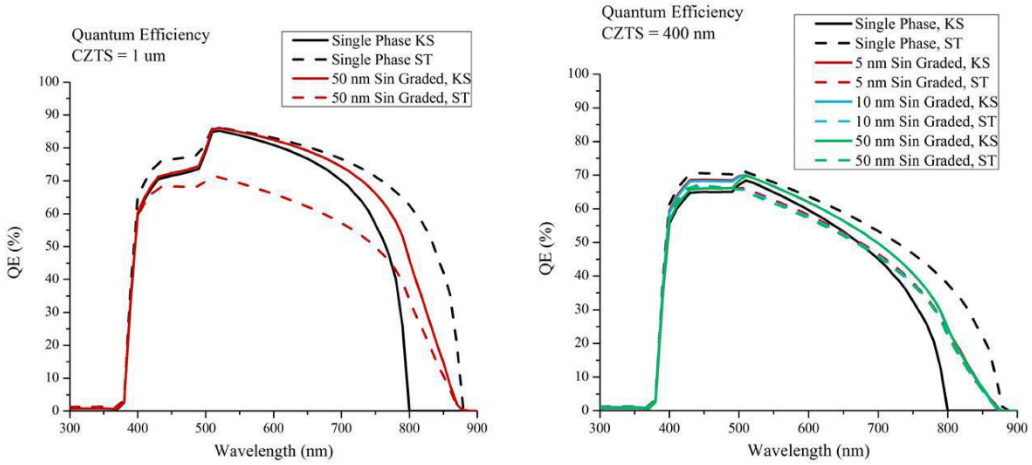

Figure 3. Quantum efficiency versus light wavelength for solar cell device models containing a 1 μm or 400 nm thick CZTS absorber layer, which is single phase kesterite or stannite, or sinusoidally graded kesterite/stannite with either kesterite (KS) or stannite (ST) at both the front and back interfaces. The graph legends indicate the sinusoidal grading scales of 5, 10, or 50 nm.

The data summarized in Table 1 indicates that cell efficiency decreases with CZTS layer thickness and that the sinusoidally-graded models' device parameters usually fall between those of the single phase models. When the CZTS phase is sinusoidally graded, the presence of kesterite as opposed to stannite at the interface actually incurs a higher open

circuit voltage (V_{OC}), short circuit current density (J_{SC}), fill factor (FF), and efficiency (η). This trend is different than the single phase models in which the devices containing only kesterite CZTS have higher V_{OC} and FF but lower J_{SC} and η than those with only stannite. There is a 7% relative increase in efficiency for a device containing 1 μm stannite CZTS as opposed to 1 μm kesterite CZTS. The other parameters besides the bandgap that differ between stannite and kesterite such as electron and hole effective masses, mobilities, and conduction and valence band density of states only contribute to a 3% relative increase in overall efficiency for stannite-only devices as opposed to kesterite-only. This was determined by using a single phase model that kept all of the parameters for stannite but changed the bandgap to that of kesterite.

As can be seen in the quantum efficiency (QE) curves in Fig. 3, the stannite-only devices have a higher QE for $\lambda > \sim 400$ nm, and absorb out to 873 nm as opposed to kesterite devices that only absorb to 795 nm. The quantum efficiency gains for kesterite instead of stannite presence at the interface are light wavelength dependent and Fig. 3 demonstrates that the gains in J_{SC} for kesterite as opposed to stannite at the interfaces originate in the 400-800 nm range. It is also interesting to note that the spatial period of the sinusoid (at least in this 1D case) has little effect on the overall performance and QE response. For the 400 nm-thick CZTS models, the change from 50 to 5 nm sinusoid only changes the efficiency by η+0.2%. However, changing the interface polytype from stannite to kesterite raises the efficiency from η=10.5±0.1% to η=13.7±0.1% for all spatial periods examined.

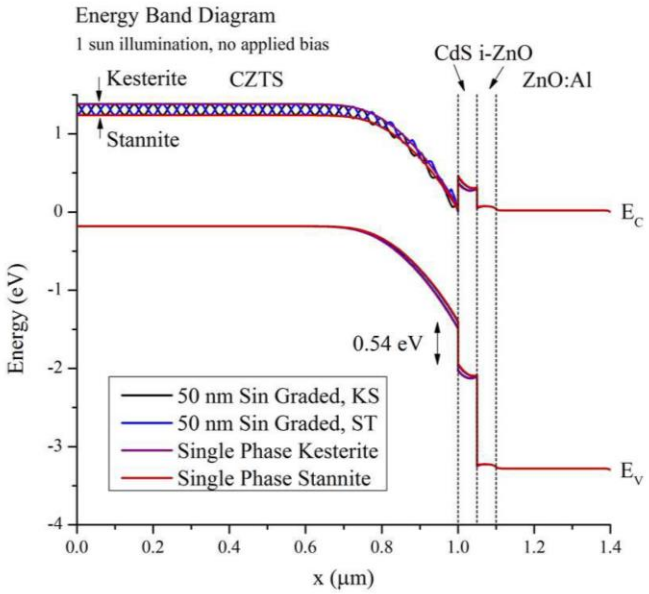

Figure 4. Energy band diagram showing band bending at the CZTS/CdS/i-ZnO/ZnO:Al interfaces for four solar cell device models. The solar cell is under 1-sun AM 1.5 illumination with no other applied bias.

The cell efficiency decreases with CZTS thickness since less light is absorbed and fewer carriers per area are generated. When comparing single-phase CZTS models, the smaller band gap of stannite, 1.42 eV, as compared to kesterite, 1.56 eV, contributes to the majority of the efficiency gains because the increased light absorption at longer wavelengths contributes to higher photocurrent and therefore higher J_{SC}. However, the gains in efficiency and J_{SC} for kesterite as opposed to stannite at the interface mainly arise from increasing the "diode activation energy"[20]. In the case of a Type 1 or straddling band alignment between CdS and CZTS, the diode activation energy is merely the CZTS band gap. If it were a Type 2 alignment, the diode activation energy would be the difference between the energy of the conduction band minimum of CdS and the valence band maximum of CZTS. An increased diode activation energy results in decreased

radiative recombination. Therefore, kesterite at the interfaces decreases the recombination in this model, thereby increasing the efficiency and J_{SC}. Since this is predominantly a band alignment effect, the thickness of the sinusoid has little bearing on the cell performance. This points out the sensitivity of the device parameters to interface band alignment with CdS and/or Mo, and also suggests a route for engineering that band alignment using polytype control. Controlling the polytype (or polytype alloy) at the buffer interface could be used to engineer the cliff /spike alignment and at the Mo interface to adjust the Schottky barrier height and/or create a minority carrier reflector.The band diagram for single phase stannite, kesterite, and 10 nm sinusoidally graded CZTS is shown in Fig. 4. The band alignment of the CdS/CZTS is Type 1 (straddling), as is evidenced by the conduction band spike, which lowers the minority carrier (electron) separation across the junction, thus lowering the photocurrent. However, the CZTS/CdS Type 1 band offset reduces interface recombination as opposed to a Type 2 alignment which has a lower interface bandgap.

3.2 Sandwich Structure

The previous observations that higher efficiency occurs with stannite in the bulk and kesterite at the interface of the absorber layer led us to test the combination of these advantages to see if both can be exploited simultaneously to gain even higher cell performance than that of the single phase stannite CZTS cells. Models of sandwich structure devices, illustrated in Fig. 2, that incorporate stannite in the bulk CZTS and various thicknesses of kesterite at the interfaces, were tested. Table 2 displays the light JV parameters for kesterite thicknesses from 5-50 nm, and Fig. 5 displays the quantum efficiency curves.

Table 2. Light JV parameters from solar cell device models containing a 1 μm thick CZTS layer that is a sandwich structure containing stannite on the inner layer and kesterite at both interfaces. The thickness of the kesterite varies from 5-50 nm.

Absorber Layer	η (%)	Voc (Volt)	Jsc (mA/cm2)	FF (%)
Single Phase Kesterite	16.8	1.070	18.3	85.5
Single Phase Stannite	17.9	0.949	22.5	84.1
5 nm KS / 990 nm ST / 5 nm KS	20.5	0.996	23.6	87.4
10 nm KS / 980 nm ST / 10 nm KS	20.4	0.996	23.5	87.5
50 nm KS / 900 nm ST / 50 nm KS	20.2	0.998	23.2	87.4

These sandwich structures do have higher efficiencies (20%) than the stannite-only CZTS absorber layers (18%), and the gains in QE (Fig. 5) and JV parameters (Tab. 2) are once again relatively insensitive to kesterite thickness, which is similar to the observation of the insensitivity to the sinusoidal length scale in the graded-CZTS cases. This efficiency gain arises from the positive benefits of more light collection with the smaller band gap of stannite in the bulk combined with the higher diode activation energy leading to lower interface recombination with the higher bandgap of kesterite at the interface. This is analogous to the bandgap grading produced by varying Ga or S utilized in high efficiency CIGSSe devices – clearly the same principle could be affected by polytype grading.

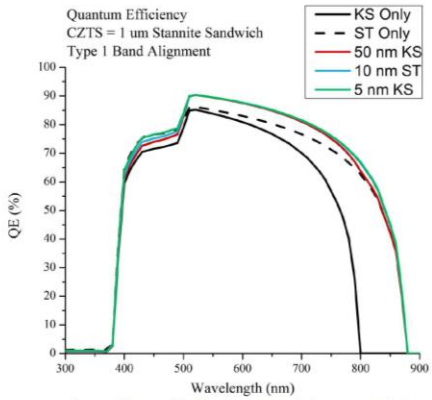

Figure 5. Quantum efficiency curves for solar cell device models containing a 1 μm thick CZTS absorber layer that is a sandwich structure with kesterite (KS) at the interfaces and stannite (ST) in the middle as shown in Fig. 2.

4. CONCLUSIONS

CZTSSe has been observed and predicted by theory to exhibit Cu and Zn site occupancy variations which can be understood as a continuous transformation between kesterite and stannite polymorphs. The kesterite/stannite transformation is believed to be accompanied by changes in bandgap and band alignments. Thus in this work we have begun to explore the engineering of interface bandgap and band alignment of CZTS devices by spatially varying polymorph fluctuation. Stannite-only devices have a higher efficiency than kesterite-only devices, and sinusoidal grading between the polymorphs generally results in efficiencies between those extremes. However, the device performances are relatively insensitive to the length scale of modulation, and instead, the phase present at the interfaces produces dramatic effects. Device models with stannite sandwiched between kesterite interface layers result in efficiencies rising from 17.9% (stannite only) to 20.5%. In this structure, the advantage of the smaller band gap of 1.42 eV for the stannite is used in the bulk of the material, and the advantage of the higher kesterite band gap, 1.56 eV, is utilized at the interface. This preliminary study demonstrates that the polytype degree of freedom can be used as a mechanism for optimizing CZTSSe device designs.

5. REFERENCES

[1] Todorov, T.K., Tang, J., Bag, S., Gunawan, O., Gokmen, T., Zhu, Y., and Mitzi, D.B., "Beyond 11% Efficiency: Characteristics of State-of-the-Art $Cu_2ZnSn(S,Se)_4$ Solar Cells," Advanced Energy Materials 3(1), 34–38 (2013).

[2] Guo, Q., Ford, G.M., Yang, W.-C., Hages, C.J., Hillhouse, H.W., and Agrawal, R., "Enhancing the performance of CZTSSe solar cells with Ge alloying," Solar Energy Materials and Solar Cells 105, 132–136 (2012).

[3] Jackson, P., Hariskos, D., Lotter, E., Paetel, S., Wuerz, R., Menner, R., Wischmann, W., and Powalla, M., "New world record efficiency for Cu (In,Ga)Se_2 thin-film solar cells beyond 20%"(January), 894–897 (2011).

[4] Olekseyuk, I., Dudchak, I.V., and Piskach, L.V., "Phase equilibria in the Cu_2S–ZnS–SnS_2 system," Journal of Alloys and Compounds 368(1-2), 135–143 (2004).

[5] Persson, C., "Electronic and optical properties of Cu_2ZnSnS_4 and $Cu_2ZnSnSe_4$," Journal of Applied Physics 107(5), 053710 (2010).

CHAPTER 6

PROJECT SUMMARIES AND SUGGESTIONS FOR FUTURE WORK

Observation of a Minority Carrier Deep Defect in CZTSSe

Summary

Junction capacitance spectroscopy was used to explore the underlying causes of non-radiative recombination in CZTSSe devices. Deep level transient spectroscopy (DLTS) was used to identify for the first time a midgap defect capturing and emitting minority carriers (electrons) in the depletion width of devices based on$Cu_2ZnSn(S,Se)_4$ absorber layers synthesized from nanoparticle ink. In the sample analyzed, this deep state is 590 meV from the conduction band edge, has a Gaussian energy distribution with FWHM approximately 170 meV, has an electron capture cross section approximately 2×10^{-14} cm^2, and exists at a concentration near 1×10^{15} cm^{-3}. These characteristics make it likely this state can contribute to low minority carrier lifetime and reduced V_{OC} in operating photovoltaic devices, and we investigate the extent of such effects. When comparing the observed trap energy with theoretical predictions of defects within CZTS and CZTSe, it is proposed the midgap trap may be attributed to either Sn_{Zn} or $V_{S,Se}$, although further work correlating chemical potential during processing with defect presence and concentration is required for more conclusive results. The SCAPS modeling software is used to determine that the presence of the defect causes a relative device efficiency loss of 35% if it is

considered a recombination center, but even as a minority trap only, the cell loses 11% relative efficiency due to the presence of this deep defect.

Future Work

The deep minority trap signature derived from calculations based on the DLTS measurements may not accurately reflect the actual trap energy and capture cross section. Temperature dependence of the capture cross section as well as entropy considerations are not accounted for [1]. Attempts to measure the capture rate using variable pulsed width DLTS were not successful in part due to very fast capture rates that exceed the speed of the instrumental response time and also due to transient behavior that was a mix of both increasing and decreasing capacitance response within a single transient. Due to this complicated behavior, determining the actual capture cross section is still of high interest in determining the accuracy of SCAPS (and other software) models to determine the overall effect on the CZTSSe device. A different measurement method needs to be used to determine the capture cross section, or obtaining a clearly decreasing transient at the DLTS peak temperature may enable clear determination of the capture cross section via the method of varying the pulse filling width. With an accurate capture cross section, an accurate trap energy may be calculated.

Investigation of Combinatorial Coevaporated Thin Film Cu_2ZnSnS_4 (II): Beneficial Cation Arrangement in Cu-Rich Growth

Summary

Raman spectroscopy was used to investigate phase coexistence in CZTS thin films coevaporated at 325 or 470 °C. At the lower growth temperature, there is a specularly

reflective band near and along the ZnS-Cu_2SnS_3 (CTS) tie line in the Cu-Zn-Sn-S quaternary phase diagram that corresponds to the coexistence of structurally coherent ZnS, CTS, and CZTS phases. The structurally incoherent secondary phases, SnS_2 and CuS, exist only as surface phases or are embedded as separate grains in the underlying film and in regions that are either Cu- or Sn-rich. Films grown at the lower temperature show a compositionally-dependent change in Cu and Sn site occupancy, evidenced by a change in the volume fractions of the CTS polymorphs: cubic-CTS dominates in the Cu-rich (Cu/Sn>2) region while tetragonal-CTS dominates in the Sn-rich (Cu/Sn<2) region. For CZTS films grown at 470 °C, CTS is not observed, although regions grown with excess Sn flux show more crystalline disorder despite stoichiometric incorporation of Sn. In contrast, areas with high Zn flux show no significant change in crystalline quality. Based on our results, we suggest growing CZTS films Cu-rich results in higher cation ordering and fewer Sn-related antisite defects.

Future Work

This work emphasizes the unknown effects of excess Sn flux on the overall defect equilibria within CZTS films. Films are typically grown at >500 °C with excess Sn flux to avoid Sn loss from SnS evaporation. This excess Sn flux has been assumed until now to have no deleterious effect since the Sn incorporated into the film is stoichiometrically self-limiting [2] within the resolution of standard compositional analysis methods. However, observed quenched PL and increased crystalline disorder in the regions of the film that were stoichiometric but grown under excess Sn flux indicate more needs to be understood about the relationship between growth conditions and native defect

concentrations. Some defects at the parts-per-billion level (10^{13}-10^{15} /cm^3) can control the minority carrier lifetime by acting as recombination centers.

It is obvious increasing Cu overpressure should promote higher concentrations of Cu_{Zn} and Cu_{Sn} antisites, and Sn loss from the film will result in more V_{Sn} defects. It is also expected that when films are annealed under conditions that allow Sn to escape, even in very small amounts, due to insufficient overpressure of Sn or SnS, V_{Sn} defects may form in the 2b Wycoff sites [3]–[7] (Figure 4.11). What is not as easily understood, however, is the effect of excess Sn flux on the overall defect equilibria. In a steady-state situation with excess Sn flux, the V_{Sn} formation energy is high [8], and high concentrations of this defect are not expected. However, the Cu (and possibly Zn) atoms in the planes ¼- or ¾-way along the c-axis containing 2c and 2d sites are highly mobile and may occupy a Sn site. This creates a Cu_{Sn} or Zn_{Sn} antisite plus a V_{Cu} or V_{Zn}, which is lower in energy for the CZTS crystal. Therefore, in the regions of excess Sn flux in the combinatorial samples, the excess Sn flux discourages V_{Sn} formation, rather, it may promote a different balance of Sn_{Cu} and Cu_{Sn} antisite occupancy. Consequently, the Cu/Sn consideration is different for the combinatorial samples than the case in which Sn is allowed to escape.

We propose a synchrotron-based resonant x-ray diffraction analysis of different regions of combinatorially grown films to determine the site occupancy dependence on composition. In addition, defect spectroscopy measurements could link variations in site occupancies with defect energy levels and possibly concentrations.

Modeling Cu_2ZnSnS_4 (CZTS) Solar Cells with Kesterite and Stannite Phase Variation

Summary

CZTSSe has been observed and predicted by theory to exhibit Cu and Zn site occupancy variations which can be understood as a continuous transformation between kesterite and stannite polymorphs. This is also suspected to be a major cause of the larger band tailing observed for CZTSSe compared to CIGSe [9]–[12]. The kesterite/stannite transformation is believed to be accompanied by changes in bandgap and band alignments. This study examines the effects of CZTS polymorphism and inhomogeneous distributions of CZTS polymorphs on device characteristics under scenarios of single phase films, a sinusoidal variation between kesterite and stannite with depth, and single phase films with thin layers of the other polymorph at both interfaces. One-dimensional solar cell devices consisting of a standard Al/ZnO:Al/i-ZnO/CdS/CZTS/Mo multilayer stack were simulated using the solar cell capacitance simulator (SCAPS) software, a program developed specifically for modeling thin film polycrystalline devices [13]–[18].

In general, stannite-only devices were calculated to have higher efficiency than kesterite-only devices due to a lower bandgap and thus more light absorption leading to higher J_{sc}. The sinusoidally-graded models' device efficiencies fall between those of the single phase models. However, the device performance is relatively insensitive to the wavelength of the sinusoidal grading, but is extremely sensitive to the phase present at the CdS interface. The presence of kesterite at the interface and stannite in the bulk induces a higher open circuit voltage (V_{OC}), short circuit current density, fill factor, and efficiency. The gains in efficiency and J_{SC} for kesterite as opposed to stannite at the interface mainly

arise from increasing the diode activation energy or interface bandgap, which is merely the CZTS band gap in the models with a Type 1 straddling alignment with CdS. These results suggest a route for engineering device band profiles using the band alignment using polytype control. In addition to effects at the CdS interface, controlling the polytype (or polytype alloy – meaning a disordered mixture of Cu and Zn site occupancy) at the buffer interface could be used to engineer the cliff /spike alignment and at the Mo interface to adjust the Schottky barrier height and/or create a minority carrier reflector.

Future Work

The SCAPS models used to investigate the polymorphism within CZTS only explore one type of recombination: band to band recombination. A more sophisticated and realistic model containing $CZTS_xSe_{1-x}$ ($0<x<1$), interface and bulk defects, band bending at the back interface, intraband tunneling, and tunneling from bands to interface defects are all of interest in the complicated effects of Cu-Zn cation disorder. Since this work was published, an updated computation of the change in VBM and CBM of CZTS and CZTSe with the self-compensating defect pair [Cu_{Zn} + Zn_{Cu}] show not only a change in the CBM, as presented in the present research, but a change in the VBM also [8]. Incorporating this new knowledge in the SCAPS model would also more accurately reflect the effect of polymorphism on overall device performance.

A method to employ bandgap engineering by selecting for a particular polymorph in the bulk vs. the interface of the absorber layer is presented by another computational project completed within the Scarpulla research group. Junyi Zhu et al. [19] predicted that defect population tuning can be achieved through induced compressive or tensile strain to the CZTS lattice. For example, Cu_{Zn} antisites form preferentially to V_{Cu} under tensile

stress, while the shallower V_{Cu} acceptor is preferred for 2-3% compressive strain. If it is possible to form the compensating Zn_{Cu} antisite as well in tensile strain, it may be possible to engineer the bandgap to achieve the gained efficiencies by selecting for the higher E_g=1.56 eV kesterite at the CZTS/CdS interface to lower the radiative recombination activation energy at the interface, and also exploit the higher absorption advantage of the lower E_g=1.42 eV for stannite within the bulk of the material. The associated effects on doping would also be important to examine. An experiment which uses surface-active agents that can modify the chemomechanical stress [20] of the CZTS would be interesting to determine if CZTS can be bandgap engineered using polymorph manipulation.

References

[1] P. Blood and J. W. Orton, *The Electrical Characterizatioin of Semiconductors: Majority Carriers and Electron States*. San Diego, CA: Academic Press, 1992.

[2] J. J. Scragg et al., "Chemical insights into the instability of Cu2ZnSnS4 films during annealing," *Chem. Mater.*, vol. 23, no. 20, pp. 4625–4633, Oct. 2011.

[3] T. Washio et al., "Analysis of lattice site occupancy in kesterite structure of Cu2ZnSnS4 films using synchrotron radiation x-ray diffraction," *J. Appl. Phys.*, vol. 110, no. 7, p. 074511, 2011.

[4] E. Zillner et al., "Lattice positions of Sn in Cu2ZnSnS4 nanoparticles and thin films studied by synchrotron X-ray absorption near edge structure analysis," *Appl. Phys. Lett.*, vol. 102, no. 22, p. 221908, 2013.

[5] S. Schorr et al., "A neutron diffraction study of the stannite-kesterite solid solution series," *Eur. J. Mineral.*, vol. 19, no. 1, pp. 65–73, Feb. 2007.

[6] S. Schorr, "The crystal structure of kesterite type compounds: A neutron and X-ray diffraction study," *Sol. Energy Mater. Sol. Cells*, vol. 95, no. 6, pp. 1482–1488, Jun. 2011.

[7] R. Schurr et al., "Real-time investigations on the formation reactions during annealing of sulfurized Cu–Sn precursors," *Thin Solid Films*, vol. 519, no. 21, pp. 7412–7415, Aug. 2011.

[8] S. Chen et al., “Classification of lattice defects in the kesterite Cu2ZnSnS4 and Cu2ZnSnSe4 earth-abundant solar cell absorbers,” *Adv. Mater.*, vol. 25, no. 11, pp. 1522–39, Mar. 2013.

[9] T. Gokmen et al., “Semi-empirical device model for Cu2ZnSn(S,Se)4 solar cells,” *Appl. Phys. Lett.*, vol. 105, no. 3, p. 033903, Jul. 2014.

[10] J. W. Boucher et al., “Optical response of deep defects as revealed by transient photocapacitance and photocurrent spectroscopy in CdTe/CdS solar cells,” *Sol. Energy Mater. Sol. Cells*, pp. 1–7, Mar. 2014.

[11] T. Gokmen et al., “Band tailing and efficiency limitation in kesterite solar cells,” *Appl. Phys. Lett.*, vol. 103, no. 10, p. 103506, 2013.

[12] J. J. Scragg et al., “Rapid annealing of reactively sputtered precursors for Cu 2 ZnSnS 4 solar cells,” vol. 4, no. July 2012, pp. 10–17, 2014.

[13] M. Burgelman et al., “Modelling polycrystalline semiconductor solar cells,” *Thin Solid Films*, vol. 361–362, pp. 527–532, 2000.

[14] K. Decock et al., “Modelling multivalent defects in thin film solar cells,” *Thin Solid Films*, vol. 519, no. 21, pp. 7481–7484, Aug. 2011.

[15] J. Verschraegen and M. Burgelman, “Numerical modeling of intra-band tunneling for heterojunction solar cells in scaps,” *Thin Solid Films*, vol. 515, no. 15, pp. 6276–6279, May 2007.

[16] A. Niemegeers and M. Burgelman, “Numerical modelling of AC-characteristics of CdTe and CIS solar cells,” in *Twenty Fifth IEEE Photovoltaic Specialists Conference*, Washington, D.C., 1996, pp. 901–904.

[17] S. Degrave et al., “Polycrystalline thin film solar cells: New features in scaps version 2.3,” in *3rd World Conference on Photovoltaic Energy Conversion*, Osaka, Japan, 2003, pp. 487–490.

[18] M. Burgelman and J. Marlein, “Analysis of Graded Band Gap Solar Cells with SCAPS,” in *23rd European Photovoltaic Solar Energy Conference*, Valencia, Spain, 2008, pp. 2151–2155.

[19] J. Zhu et al., “Strain tuning of native defect populations: The case of Cu2ZnSn(S,Se)4,” *APL Mater.*, vol. 2, no. 1, p. 012110, Jan. 2014.

[20] D. B. Holt and B. G. Yacobi, “An Introduction to Extended Defects,” in *Extended Defects in Semiconductors: Electronic Properties, Device Effects, and Structures*, Cambridge University Press, 2007, pp. 73–121.